Pyrolysis and Flamelet Model for Polymethyl Methacrylate in Solid Fuel Sc(ramjet) Combustors

Henry R. Pace

Dissertation submitted to the Faculty of the

Virginia Polytechnic Institute and State University

in partial fulfillment of the requirements for the degree of

Doctor of Philosophy

in

Aerospace Engineering

Luca Massa, Chair

Gregory Young

Joseph A. Schetz

Joseph W. Meadows

September 9, 2024 Blacksburg, Virginia

Keywords: Solid fuel scramjets, Solid fuel propulsion, Combustion modeling, Flamelet Generated Manifolds

Copyright 2024, Henry R. Pace

Pyrolysis and Flamelet Model for Polymethyl Methacrylate in Solid Fuel Sc(ramjet) Combustors

Henry R. Pace

Abstract

Scramjets have been identified as a potential long-term replacement for rocket and ramjet propulsion systems due to their enhanced performance at high Mach numbers. The introduction of solid fuels in these scramjet systems allows for shaping of the solid fuel cavity by additive manufacturing and introduces the possibility of enhancing combustion rates and stability. The present investigation aims to develop a coupled, high-order computational model to study the combustion of solid fuel scramjets. The primary objectives are to identify the effects of changing geometry on combustion and to better characterize the combustion process and flow patterns within a solid fuel scramjet engine.

The high-Mach number of the air inflow over a scramjet cavity introduces a strong coupling between fluid dynamics, combustion, and regression time scales. Existing models often use simplified treatments of melt-layer conditions and combustion models that over-predict experimental rates, along with highly dissipative numerical schemes that inhibit the study of thermo-acoustic interactions between coherent pressure waves and the burning walls of the cavity. These limitations in current models suggest the need for a Navier-Stokes solver based on a high-order, discontinuous Galerkin method, incorporating melt layer equations and enhanced combustion manifolds. These manifolds should account for the effects of pressure and high oxidizer temperatures on flamelet dynamics. The focus is on modeling the flow field with accurate chemical heat release and residence time, to better study the effects of heat flux on the solid surface and the resulting coupling.

An investigation of solid fuel scramjets was performed, and the numerical methodology with which the problem was tackled is described. A novel combustion mechanism was developed using a counterflow burner to study the combustion and regression of solid

model fuel polymethyl methacrylate (PMMA). The diffusion flame between the fuel and oxidizer was studied numerically using a solid fuel decomposition and melt layer model to simulate convection and pyrolysis of the material. This model was validated using new experimental data as well as previously published works. The foam layer parameters are critical to the success of the validation. Results showed that the increased residence time of the gas in the bubbles facilitates the fuel breakdown. Fully coupled fuel injection and solid fuel surface monitoring was implemented based on this counterflow model and was a function of heat flux. Fuel regression was handled using adaptive control points for a B-Spline basis that updates based on surface movement. This methodology was used due to its resilience against the creation of surface discontinuities likely to result from large temperature gradients during combustion. Fourth-order computational simulations of ramjet combustion without regressing fuel walls using an in-house Discontinuous Galerkin approach were performed with a fully conjugate solution for the thermal wave in the solid. Results in ramjet geometries showed the turbulent combustion strongly affects the heat feedback to the walls and thus increases both the regression and fuel injection rates. Scramjet geometries were also simulated using the flamelet-progress variable approach in two different oxidizer conditions. All of these simulations showed strong agreement with experimental data and helped to uncover flame holding characteristics of the scramjet cavities and the strong coupling between the recirculation region and pyrolysis of fuel.

The analysis has led to a better understanding of the effects of solid fuel scramjet geometries on mixing, enhanced modeling of acoustic instabilities in solid fuel air-breathing propulsion, and improved fuel chemistry modeling. It has been shown that cavity design significantly influences heat transfer to the solid fuel in both ramjet and scramjet conditions. The presence and thickness of the melt layer will guide designs that aim to reduce or enhance mechanical removal of fuel. Additionally, ramjet results indicate that longer cavities can couple with acoustics to induce self-excited conditions, leading to increased heat transfer to the solid. The importance of self-sustained instability and its coupling with melt layer fuel injection will contribute to improved acoustic stability. Developing pressure/temperature-dependent manifolds and melt layer models will advance our

understanding of solid fuel supersonic combustion and its effects on phenomena such as blowout, fuel residence time, and solid fuel dual-mode transition.

Pyrolysis and Flamelet Model for Polymethyl Methacrylate in Solid Fuel Sc(ramjet) Combustors

Henry R. Pace

General Audience Abstract

Scramjets, a type of high-speed jet engine, could one day replace rockets due to their efficiency at very high speeds. By introducing solid fuels into these engines, researchers can use advanced manufacturing techniques to shape fuel cavities, potentially enhancing the engine's performance. This study focuses on developing a sophisticated computational model to understand how changes in engine geometry affect the combustion process in solid fuel scramjets. The research aims to better understand the complex interactions between airflow, combustion, and fuel consumption, with the ultimate goal of improving engine design.

The findings from this research provide valuable insights into how different scramjet designs impact fuel combustion. For instance, the design of the fuel cavity can significantly affect heat transfer, influencing the efficiency and stability of the engine. The study also highlights the importance of understanding the interaction between airflow and fuel injection, which is critical for optimizing engine performance and ensuring reliable operation at high speeds. Overall, this research advances our understanding of solid fuel scramjets and contributes to the development of more efficient and stable high-speed propulsion systems. By improving our ability to model and predict the behavior of these engines, the findings will guide future designs, potentially leading to more effective and reliable scramjets for various applications, including space exploration and high-speed flight.

Dedication

To my loving wife Kayla

Acknowledgments

I would like to first thank my advisor, Dr. Luca Massa, who's continued insights have been critical in both the development of the research herein and my professional career as an engineer. I hope his work ethic and critical mind will continue to give me inspiration as I continue my career. I would also like to thank the other members of my committee, Dr. Gregory Young, Dr. Joseph Schetz, and Dr. Joseph Meadows for their direction and recommendations throughout the course of this work. I would also like to thank my family for their continued love and support throughout my life both when I am with them and when I am away. This PhD would not have been possible without both the insights from my advisors and the support from my loved ones.

Contents

List of Figures **IX**

List of Tables **XV**

1 Introduction **1**

1.1 Brief Overview 1

1.2 Motivation 3

1.3 Dissertation Organization 4

1.4 Publications 5

1.5 Key Contributions 6

2 Review of Literature **8**

2.1 Supersonic Air-breathers 8

2.1.1 Ramjets 8

2.1.2 Scramjets 10

2.2 Solid Fuels 13

2.3 Surface Regression 17

2.4 Computational Fluid Dynamics 18

2.4.1 Reynolds Averaged Navier Stokes 20

2.4.2 Large Eddy Simulations 20

2.4.3 Discontinuous Galerkin Solver 22

2.5 Numerical Surface Regression and Grid Adaptation 23

2.6 Chemical Reaction Modeling 25

2.6.1 Flamelet-Progress Variable Approach 30

3 Solid Fuel Decomposition and Mechanism 32

3.1 Counterflow Burner 32

3.2 Sublimation Model 33

3.3 Melt Layer Model 34

3.3.1 Effect of Foam parameters on Regression Rate 39

3.3.2 Comparison of Regression Rate and Flame Stand off versus Experiments 41

4 Discontinuous Galerkin Solver 43

5 Flamelet Generated Manifolds 48

5.1 Low Temperature Manifold 51

5.2 High Temperature Manifold 53

5.2.1 Ignition Manifold 55

5.3 Summary 56

6 Comparisons of Finite Rate Chemistry and Flamelet Generated Manifold Solutions 58

6.1 Deep Cavity Case 59

6.1.1 Visual Comparison of FRC and FGM Simulations 60

6.1.2 Graphical Comparison 63

6.2 Unstable Boundary Layer Flame Case 66

6.2.1 Visual Comparison 67

6.2.2 Graphical Comparison 70

6.3 Conclusions 73

7 (sc)Ramjet Simulations 74

7.1 Experimental Procedures and Geometry 74

7.1.1 Ramjet Setup 74

7.1.2 Scramjet Setup 75

7.2 Non-Reacting Scramjet Case 76

7.2.1 Contribution of the Subgrid Model 77
7.2.2 Effect of Polynomial Order of Solution 79
7.2.3 Contribution of Rough Walls 80
7.2.4 Contribution of the Exhaust Plume 82
7.2.5 Different Cavities 82
7.2.6 Spectral Proper Orthogonal Decomposition (SPOD) of Cold Flow Modes 83
7.3 Low Temperature Manifold Simulations 85
7.3.1 Reacting Ramjet Case 85
7.3.2 Reacting Scramjet Case 89
7.3.2.1 Numerical Solution Fields 90
7.3.2.2 Validation 93
7.3.2.3 Discussion 99
7.3.3 B-Spline Surface Movement 100
7.4 High Temperature Manifold Simulations 105
7.4.1 Numerical Solution Fields 106
7.4.2 Validation 110
7.4.3 Discussion 114

8 Conclusions and Recommendations for Future Work 116

Bibliography 119

Appendices 138

A Additional Figures 140

List of Figures

2.1 Basic schematic of ramjet combustor 9

2.2 Characteristic performance by engine type [1] 10

2.3 Basic schematic of scramjet combustor 12

2.4 Schematic diagram of an SFRJ com bus tor showing the fluid dynamic and combustion characteristic [2] 13

2.5 Configuration of a) subsonic and b) supersonic combustion solid fuel ramjets [3] 14

2.6 Combustion wave for a typical solid fuel [4] 16

2.7 Sketch of solid fuel used in counterflow, stagnation flame 17

2.8 PMMA regression rate model using heat of vaporization [5] 18

2.9 Density contours of several combustor geometry simulations performed by Kummitha [6] 19

2.10 Temperature solution for the HIPPO nozzle assuming finite-rate chemistry. Material response domain is indicated by gray region. [7] 25

2.11 Model sizes: number of reactions as a function of the number of species for gas phase kinetic models of pyrolysis, oxidation, and combustion processes. The secondary axis is the number of heavy (non-hydrogen) atoms in the reactant molecule(s) [8] 27

2.12 Mixture fraction and temperature from a steady-flamelet solution in physical space. Methane–air combustion [9] 31

3.1 Computed species mole fractions at oxidizer inlet conditions of 573 K and 0.432 $kg/(s * m^2)$ 33

3.2 Experimental vs sublimation model results 34
3.3 Comparison of two models inside a foam layer with heat flux of 17.38 kW of heat flux applied to surface 38
3.4 Fuel inlet conditions as a function of mass flux 39
3.5 Effect of foam parameters on the burn rate in nominal counter flow conditions. The left plots has $n = 50\text{mm}^{-3}$, the right plot has $s = 0.5$; legend: — "RhoU"; --- "V". 41
3.6 Validation of mechanism comparing the regression rate and flame standoff distance versus experiments. Legend: — Modified; --- Original, (●) Measurements. [10] 42
3.7 Foam layer solid decomposition model. 42

5.1 CO_2 mass fraction at maximum temperature vs distance between inlets, L. 49
5.2 Turbulent library storage of CO2 net production 50
5.3 CO_2 mass fraction vs mixture fraction at multiple flame states with 1 being fully extinct and 10 being adiabatic 53
5.4 Flame states as a function of progress variable and mixture fraction with interpolation points 54
5.5 Turbulent library storage of CO_2 production rate with high (1200K) oxidizer temperature using extinction to model unstable burning branch . . 55
5.6 Turbulent library storage of CO_2 production rate with high (1200K) oxidizer temperature using ignition to model unstable burning branch . . . 56

6.1 Deep cavity FRC geometry 59
6.2 Instantaneous FRC solution shortly after autoignition for geometry with deep cavity 60
6.3 Comparison of instantaneous production of CO_2 between two FGMs and finite rate chemistry in deep cavity 61
6.4 Comparison of instantaneous production of CO_2 between two FGMs and finite rate chemistry in deep cavity after 2.5e-4 seconds of independent running 62

6.5 Comparison of instantaneous temperature between two FGMs and finite rate chemistry in deep cavity after 2.5e-4 seconds of independent running 63
6.6 Comparison of CO_2 production as a function of mixture fraction and flame progress 65
6.7 Flat plate with boundary layer geometry 66
6.8 Instantaneous FRC solution shortly after autoignition for geometry with boundary layer blowoff 67
6.9 Comparison of instantaneous production of CO_2 between two FGMs and finite rate chemistry in boundary layer blowoff 68
6.10 Comparison of instantaneous production of CO_2 between two FGMs and finite rate chemistry in boundary layer blowoff after 2.5e-4 seconds of independent running 69
6.11 Comparison of instantaneous temperature between two FGMs and finite rate chemistry in boundary layer blowoff after 2.5e-4 seconds of independent running 70
6.12 Comparison of CO_2 production as a function of mixture fraction and flame progress 72

7.1 Experimental diagram of ramjet combustor sections and relevant dimensions [11, 12] 75
7.2 Scramjet test section schematic with labeled probe locations 76
7.3 FG11 pressure comparison in cold, non-reacting flow 77
7.4 Effect of Subgrid Model on cold flow predictions in FG14 78
7.5 Mean Mach number profiles of optically accessible scramjet test cases FG14 79
7.6 Experimental shadowgraph of FG14 flow bias in cold, non-reactive flow . 79
7.7 Effect of polynomial order on cold flow predictions in FG14 80
7.8 Instantaneous pressure field of FG14 with rough walls in the expandion section 81
7.9 Effect of wall roughness on cold flow predictions in FG14 81

7.10 Comparison of the effect of plume exit conditions on the pressure in the FG14 combustion chamber. 82
7.11 Comparison of measured and computed wall pressures for the shorter cavity, FG25. 83
7.12 SPOD modes spectral energy density in bar $\cdot$ m^3 84
7.13 SPOD modes dimensionless eigenfunctions at the first three frequencies marked by open circles in figure 7.12. 85
7.14 Schematic of the boundary conditions for the Ramjet simulations 86
7.15 LES mean ramjet mixing chamber pressure compared to the experiments 86
7.16 Comparison of ramjet LES regression rates (solid lines) versus the experiments (dashed lines) 87
7.17 Comparison of ramjet LES heat fluxes (feedback to the fuel) for shallow geometries 88
7.18 Mixture fraction in the LES ramjets at an instant in time during the statistically stationary evolution 89
7.19 Calculated time-averaged temperature fields in the ramjet 89
7.20 3D mesh of FG11 with boundary labels 90
7.21 Instantaneous snapshots of the FG11 solution fields 91
7.22 Mean distribution of FG11 fluid field solutions 92
7.23 Burn rate of FG11 solid fuel walls, mm/s 93
7.24 Wall pressure at 7 probe locations in FG11 reacting case 94
7.25 Standard deviation of wall pressure in FG11 reacting case 95
7.26 Regression rate on four different FG11 grids 97
7.27 Spectral energy frequency of pressure fluctuation in FG11 solid fuel scramjet (atm/(cm^{3}Hz)). 98
7.28 Real and imaginary parts of the most amplified FG11 SPOD mode . . . 98
7.29 FG11 instantaneous mixture fraction and heat release rate in W/mm^3 . . 99
7.30 Mach number visualization at different times during combustion with black contour line representing the sonic condition 103

7.31 Static pressure visualization at different times during combustion with black contour lines representing streamlines 104
7.32 2D structured meshes 106
7.33 Mean Mach number at three stages of FG14's deformation with black contour line representing the sonic condition 107
7.34 Mean pressure at three stages of FG14's deformation with black lines representing streamlines 109
7.35 Mean temperature at three stages of FG14's deformation 110
7.36 Comparisons of pressure along the fuel surface at ignition 111
7.37 Comparisons of pressure along the fuel surface after 2.67 seconds of combustion 112
7.38 Comparison of fuel regression rate at time of ignition 113
7.39 Comparison of fuel regression rate 2.67 seconds after ignition 114

A.1 Temperature distribution inside flamelet generated manifold for MMA at low (600K) oxidizer temperature 140
A.2 Comparison of instantaneous CO_2 mass fraction between two FGMs and finite rate chemistry in deep cavity after 2.5e-4 seconds of independent running 141
A.3 Comparison of instantaneous heat release between two FGMs and finite rate chemistry in deep cavity after 2.5e-4 seconds of independent running 141
A.4 Comparison of instantaneous heat release between two FGMs and finite rate chemistry in boundary layer blowoff after 2.5e-4 seconds of independent running 142
A.5 Comparison of instantaneous CO_2 mass fraction between two FGMs and finite rate chemistry in boundary layer blowoff after 2.5e-4 seconds of independent running 143
A.6 Temperature visualization at different times during combustion for 2D FG11 geometry 143

A.7 Mixture fraction visualization at different times during combustion for 2D FG11 geometry 144

A.8 Wall shear force during FG14 combustion at three stages of solid fuel deformation 144

List of Tables

7.1 Experimental Combustor Specifications 76

Chapter 1

Introduction

1.1 Brief Overview

Combustion has been at the center of society for thousands of years and has led to countless idioms such as 'the spark of civilization' and mythology like the story of Prometheus. As the human race has advanced, so too has our ability to wield combustion to our benefit [13]. In more recent centuries, the primary medium of combustion has shifted from wood to fossil fuels, which provide a much greater energy release and relatively low auto-ignition temperatures. The use of these fossil fuels in engines has traditionally focused on mixing liquid or gaseous fuel with air to induce combustion and increase gaseous temperature.

While not widely used in the past, solid fuel air-breathers are under investigation due to the high performance of solid fuels in propulsion, dating back as early as 1,000 years ago in early Chinese rockets [14, 15]. While rockets have been highly effective, the need to carry both the oxidizer and fuel on board results in decreased specific impulse and performance characteristics. This has led researchers to evaluate the combination of air-breathing propulsion systems with solid fuels. While liquid hydrocarbons have been heavily utilized in air-breathers over the past century, the use of solid fuels in air-breathing propulsion applications such as hybrid rockets is now under investigation due to their ability to increase fuel-carrying capacity, simplify injection methods, and improve long-term storage capabilities [16, 17, 18].

The improved storage capabilities and simplified injection benefits are easy to com-

prehend. Solid fuels are not as reliant on pressurized containers, nor are they as prone to leaking as gaseous and liquid fuels. Solid fuels also rely on pyrolysis, allowing for a reduction in the complexity of valves and pumps that would otherwise be needed to inject gaseous fuels. Solids generally possess a higher density than other states of matter which, coupled with the lack of weight addition from pumps and valves, means one is able to increase the amount of stored fuel energy on an aircraft. However, all technologies have limitations, and solid fuels are no exception. While there are many advantages such as those listed above, high ignition temperatures, changing geometries due to pyrolization, and thrust modulation issues cause complications when implementing solid fuels into real world applications [19, 20].

Polymers are commonly used as model fuels in various propulsion systems such as hybrid rockets, solid fuel ramjets, and solid fuel scramjets [21, 22]. Air-breathing propulsion systems supported by the combustion of pyrolyzing fuel walls have several advantages when compared to rocket propulsion, including an enhanced stability of the deflagration, higher payload, drastically increased specific impulse, and their ability to perform without an on-board supply of oxidizer; however, due to their reliance on the ambient medium through which they travel, the operational range is reduced to within the atmosphere at high air speeds. The range where the solid fuel scramjet is preferred to the rocket analog depends on the aero-thermal enhancement of the flame [23], which represents the fraction of the friction entropy loss that is transferred to the combustion region. The internal circulatory flow within a cavity reduces the frictional/aero-thermal transfers to the fuel, but it increases the chemical residence time; therefore, a cavity design that optimizes both aero-thermal transfers and residence time is key to the success of air-breathing solid fuel scramjets. These values are heavily affected by the energy released during combustion as well as the rate of fuel consumption and thus the regression of the walls within a solid fuel cavity.

Numerical models are used to better understand the predominant physics in a complex system in order to predict the outcome and dissect data that might be difficult to obtain through experimental methods. In order to create these models, one must have

an understanding of the phenomenon at play and the ability to reduce the complexity in order to produce timely results. So how can one create a solid fuel scramjet model that is as simple as it should be, but no simpler?

1.2 Motivation

The escalation and emergence of various threats have led to the need for new projectile and aircraft delivery systems with increased range and speed [24]. High-speed missiles have traditionally utilized rocket propulsion. However, the range associated with these systems is often limited because they must carry both the oxidizer and fuel within the propellant. Air breathers such as ramjets have been used to greatly increase missile range due to increased specific impulse. Unfortunately, ramjets begin to perform poorly in the hypersonic regime due to the increased heating and pressure losses from decelerating air to subsonic speeds inside the combustor. To mitigate these losses, scramjets can be used, as they do not require deceleration to subsonic flow through the combustor [25].

While liquid-fueled scramjets have shown promise in the field [26, 27], many DoD applications require long-term fuel storage, which is impractical with jet fuels and nearly impossible with hydrogen. Because of this, solid fuels are preferable to liquids in many applications. In addition to storage benefits, solid fuels also do not require the pumps and valves necessary in liquid systems. These benefits, coupled with the increased energy density of solid fuels, present the potential for a powerful scramjet propulsion system.

While experimental testing is necessary to obtain a general understanding of the predominant physics in a system, a more detailed description can often be found using a computational fluid dynamics (CFD) model. Computational models can also be far cheaper and faster to run than their experimental counterparts which allows for quicker design optimization [28, 29]. The conditions inside a scramjet combustor make the modeling of reactive flow challenging; however, in recent years flamelet-progress variable (FPV) approaches have shown promise in modeling reactive flow under compressible conditions [30, 31].

1.3 Dissertation Organization

Chapter 2 reviews the existing literature on solid fuel (sc)ramjet combustion and numerical chemistry modeling, with an emphasis on scramjets and combustion.

Chapter 3 discusses solid fuel decomposition and the chemical mechanism used within this work. The investigation into the PMMA regression rate and the counterflow burner method for its characterization is also discussed. Special attention is paid to the numerical modeling efforts to recreate the multi-phase foam layer present during PMMA decomposition, and the foam layer's effects on regression rate are examined.

Chapter 4 is relatively brief but provides key insights into the numerical methodology used when discretizing and investigating the flow. The discontinuous Galerkin solver is discussed, and the incorporation of the flamelet-progress variable approach is explained in order for the reader to better understand the flamelet tracking and energy balance equations considered.

Chapter 5 begins by explaining the flamelet generated manifolds (FGMs) in general and how they are implemented into the flamelet-progress variable approach. Three different manifolds are then discussed where the oxidizer temperature is varied as well as the modeling of the unsteady portions of the manifolds. The "low" temperature manifold was created with the oxidizer below the autoigniton point of MMA, and the two "high" temperature manifolds were created with the oxidizer above this point. Because of this high temperature oxidizer, one of these FGMs were created using ignition as opposed to extinction. The key differences between these three manifolds is the flamelet progress source term being much greater in the high temperature manifolds - especially when modeled using extinction.

Chapter 6 discusses how finite rate chemistry simulations are performed in simplified geometries that complement the combustion seen in the supersonic scramjet combustors. These results were used to validate the flamelet-progress variable solutions in the high

temperature extinction and ignition manifolds and to gain a better understanding of the FGM performance. The goal of this chapter was to identify FGM shortcomings and how they can be improved upon in the future.

Chapter 7 comprises the bulk of this dissertation, and discusses comparisons between numerical (sc)ramjet results and their experimental counterparts. Non-reacting cold flows in the scramjet cavities are first discussed in order to gain confidence in the fluid solvers used and to gain a better understanding of the predominant physics such as acoustic modes, recirculation zones, supersonic shear layers, and expansion regions. Reacting simulations are then discussed, and the performance of the flamelet-progress variable approach is assessed. Both "low" and "high" temperature FGMs produced reasonable results when compared to experimental data and helped to offer insight into solid fuel cavity flameholding and the effects of varying geometry. A novel free-form deformation (FFD) box approach was implemented when investigating the "low" temperature FGM in SFSJ conditions in order to observe transition of the core flow from trans to supersonic throughout the combustor.

Chapter 8 is a recapitulation of all the work in a concise manner. Key takeaways and recommendations for future work are provided.

1.4 Publications

Peer-reviewed Journal Publications

1. **Pace, H.**, Arnold, C., Gallegos, D., Young, G., and Massa, L., "Acoustics in Flameholding Solid-Fuel Ramjet Fuel Grains," *AIAA Journal*, Vol 61, No. 10, 2023, pp 4579-4597

2. Gallegos, D., **Pace, H.**, Arnold, C., Massa, L., and Young, G., "Regression and Flame Structure in Cavity Flameholding Solid-Fuel Ramjet Fuel Grains," *Journal of Propulsion and Power*, Vol. 39, No. 6, 2023, pp. 800-810

3. **Pace, H.**, Schlussel, E., Young, G., and Massa, L., "Contribution of Unsteadiness to Solid Fuel Burning Characteristics in a Scramjet Combustor," *Journal of Propulsion and Power*, in press

4. Schlussel, E., Gallegos, D., **Pace, H.**, Massa, L., and Young, G. Flow characteristics in an optically accessible solid fuel scramjet. *Journal of Propulsion and Power*, in press

Conference Proceedings

1. **Pace, H.** and Massa, L., Combustion of PMMA in Solid Fuel Scramjet Cavities, in *AIAA AVIATION 2022 Forum*

2. **Pace, H.** and Massa, L., Analysis of Acoustic Modes in Solid Fuel Ramjet Cavities, in *75th Annual Meeting of the Division of Fluid Dynamics*, Vol. 67, No. 19

3. **Pace, H.**, Arnold, C., and Massa, L., PMMA Solid Fuel Flamelet Model for High Speed Flows, in *AIAA AVIATION 2023 Forum*

4. **Pace, H.** and Massa, L., Large Eddy Simulations of Solid Fuel Scramjet with Deformed Wall Geometry, in *AIAA SCITECH 2024 Forum*

1.5 Key Contributions

Completed:

1. Development of a detailed PMMA combustion model by simulation of counterflow diffusion flames which included prediction of flame temperature, standoff distance, and regression rate.

2. Development of a melt layer multiphase model and its coupling to the gas phase reactions. This novel contribution was tabulated as a function of heat flux such that it could later be implemented into scramjet simulations to accurately predict fuel injection and pyrolysis rates.

3. Investigation and validation into flamelet generated manifolds and application of novel polynomial curve fit approaches to account for compressibility effects and pressure variations in the scramjet combustion chamber.

4. Two FGM manifolds created at different temperatures and two related methods for searching and optimizing these manifold solutions in order to account for varying properties of the chosen progress variable.

5. Comparison and validation of flamelet-progress variable models using a finite rate chemistry mechanism inside simplified geometries to test flow profiles.

6. Cold flow CFD analysis of several lab scale scramjet combustion chambers. Investigation of the effect of geometry, roughness effects, and plume conditions on the coherent pressure modes as well as an investigation into several sub-grid scale LES models and their performance inside a scramjet combustor geometry.

7. Reacting flow, fixed walls, analysis of parameterized lab scale scramjet combustion chambers. Investigation of the effects of geometry and combustion manifolds on the fuel burn rate. Exploration of the effects of a regressed geometry on the flow characteristics and fuel regression rates seen within a reacting SFSJ.

8. Scramjet regression analysis and application of a novel FFD boxes regression algorithm to investigation of the effect of geometry changes on the combustion field.

Chapter 2

Review of Literature

2.1 Supersonic Air-breathers

High-speed, long-range aircraft have been at the forefront of technological development for many years, following the demonstrated capabilities of air power in WWI and WWII [32, 33]. Although rocket engine planes were prevalent in the early history of high-speed flight, supporting the first supersonic flight in 1947 [34, 35], their use quickly diminished due to the requirement of carrying both oxidizer and fuel onboard. High-speed, air-breathing propulsion took over the following decades due to the increased specific impulse that allowed for improved mission duration and distance.

Utilizing air as the oxidizer reduces the weight of onboard fuel and oxidizer systems; however, this approach introduces other challenges. Before combustion occurs within a jet engine, the air must be compressed to achieve optimal pressure gain, traditionally accomplished through large blade structures. These 'turbojets' are highly efficient in subsonic and low supersonic conditions, but as the demand for faster air travel increased in both civilian and military aviation, the need for more efficient propulsion systems became evident.

2.1.1 Ramjets

Another popular option for high-speed travel is the 'ramjet,' which, similar to rockets, simplifies the mechanical complexity of a turbojet by eliminating the fan and turbine

blades and using shocks to reduce the flow to subsonic conditions [1]. Like turbojets, ramjets have an advantage over rockets in long-distance missions because they do not need to carry onboard oxidizer supplies. However, their simplified geometry and high-speed capabilities make them superior to turbojets in flight conditions exceeding Mach numbers 3 to 5[36].

As previously mentioned, the geometries within ramjet tend to be very simple as seen in Figure 2.1. Supersonic air enters the intake, is reduced to subsonic conditions via a series of shocks, and enters the combustion chamber. Here, fuel is injected and mixes with the incoming air to produce combustion and a temperature increase. Mixing chambers are also sometimes incorporated downstream to aid in complete combustion, but that is not included in this diagram. The flow is choked, and, due to the enthalpy increase experienced during combustion, it can be expanded to reach supersonic speeds once more. These high temperature, supersonic products provide thrust for the vehicle as they exit.

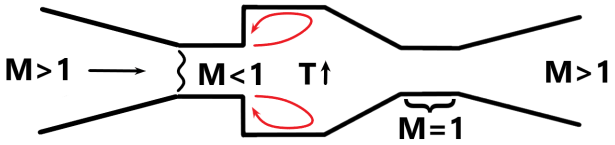


Figure 2.1: Basic schematic of ramjet combustor

Despite their advantages, the operational range of ramjets is limited by both upper and lower Mach number bounds. Ramjets require a minimum airflow velocity to operate efficiently, rendering them impractical for low-speed and subsonic flight regimes. Moreover, their efficiency drops significantly as airspeed decreases, limiting their applicability in transonic and subsonic flight conditions. Consequently, ramjets are often paired with other propulsion systems, such as rockets, to supplement their performance and versatility, especially in scenarios requiring rapid acceleration and altitude gain.

At higher speeds, ramjets encounter different but equally hazardous issues. As the flow Mach number increases, the shocks designed to reduce the flow to subsonic conditions become stronger. In the hypersonic regime, these strong shocks can result in significant total pressure losses and drastic temperature increases. The total pressure losses pose a

very clear concern due to these losses needing to be compensated for during combustion in order to provide a net increase in pressure and thus produce thrust. The increased temperatures can cause both structural and chemical problems including material failure and dissociation of the incoming air.

2.1.2 Scramjets

Depending on the aerothermal properties and the initial Mach number of the fluid, strong shocks could cause dissociation of oxygen in ramjets, leading to a decrease in potential chemical energy prior to combustion. This leads to a relative pressure loss and thus a decrease in combustion performance [37]. Scramjets are supersonic combustion ramjets that rely on high-speed airflow through the engine to compress and heat incoming air. Unlike ramjets, scramjets do not need to reduce the flow to subsonic speeds. Scramjets have been successfully tested in various experiments, including NASA's X-43A [38], which set a world speed record of Mach 9.6 in 2004. Figure 2.2 visualizes how strong shocks in ramjets can cause performance drops at high Mach numbers and shows the specific impulse for various propulsion types using both hydrogen and hydrocarbon fuels as a function of Mach number. As one can see, with an increase in the free-stream Mach number, one must adjust the type of propulsion used in order to maintain peak performance.

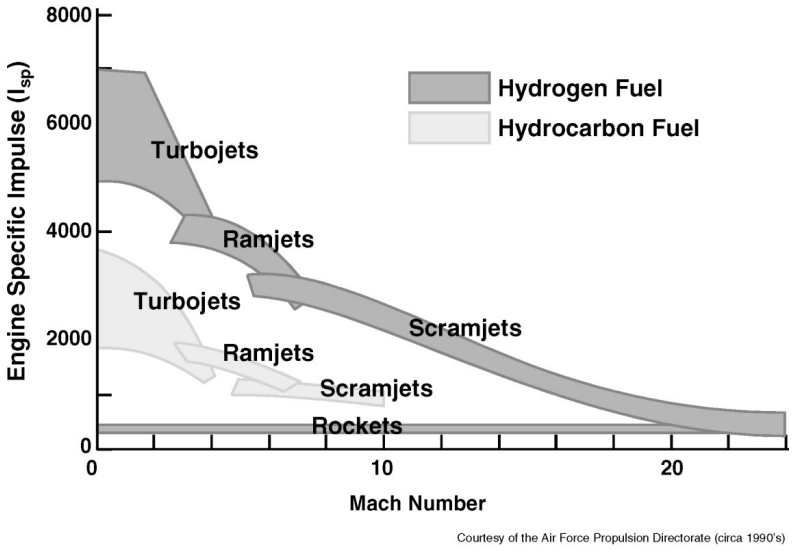


Figure 2.2: Characteristic performance by engine type [1]

From Figure 2.2, one might expect hydrogen to be an obvious choice in scramjet fuel, but, while it is a common fuel, there are several drawbacks to its usage. The cause of hydrogen's high specific impulse comes from its high "Lower Heating Value" [39]; however, due to the low density of liquid hydrogen its volumetric heating value is actually quite low in comparison to other hydrocarbon/metallic jet fuels. For example, some fuels, such as RP-1, possess potential energy densities 400% greater than liquid hydrogen [40]. The result of this is that while hydrogen may have incredible energy storage properties on a molar basis, its low density makes onboard vehicle storage rather cumbersome. For long distance missions, the volumetric storage of hydrogen is likely to strongly affect aerodynamic vehicle design.

There are several design factors that must be taken into consideration when designing a scramjet-combustion system due to the nature of the supersonic flow throughout as seen in Figure 2.3. Two such large areas of concern include scramjet unstart and blowout. Unstart in scramjet engines is a highly undesirable event that can severely disrupt engine performance and even lead to catastrophic failure. This can be a product of inlet geometry, flow conditions and even combustion processes such as thermal choking if no isolator is present [41, 42]. While inlet design is not directly relevant to the current work, and inlet flow conditions remain relatively constant due to upstream chamber conditions, heat release within the combustor causing thermal choking can result in unstart as well [43, 44]. Increased temperatures and additional mass due to fuel addition in the combustion chamber can result in a pressure wave that propagates upstream, causing a sudden loss of airflow compression and combustion efficiency at the inlet.

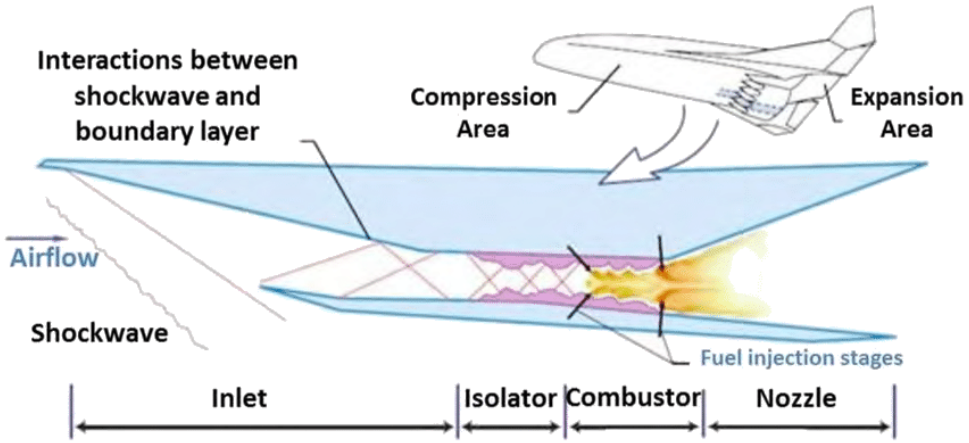


Figure 2.3: Basic schematic of scramjet combustor

Blowout in scramjet engines is a critical phenomenon that can severely impact engine performance and efficiency [45]. It occurs when the supersonic flow within the engine separates from the combustor walls and flameholders, leading to a loss of combustion stability and, ultimately, flame extinction. Understanding the mechanisms and conditions that contribute to blowout is essential for the design, development, and operation of scramjet engines.

One of the primary factors contributing to blowout in scramjet engines is the complex interaction between the high-speed airflow and the combustion process. At high Mach numbers characteristic of hypersonic flight, the airflow experiences significant compression and heating as it enters the combustor, which aids in combustion but can also increase transient flow phenomena due to the potential for shocks and pressure waves. Additionally, the high levels of shear present in scramjet flows further exacerbate the risk of blowout by disrupting the flame front and increasing strain, which can reduce mixing and thus hinder combustion [46].

In order to prevent blowout, flow anchoring mechanisms must be employed. This is generally done using either struts or cavities. Strut flame-holding geometries usually utilize intrusive surface geometries that cause flow separation where fuel can be injected, thus increasing mixing [47, 48, 49]. Cavity flame-holding geometries implement a sharp surface recession that creates a lid-driven flow [50], where supersonic flow over the top of the cavity drives the recirculation region. Fuel is commonly injected directly before or

inside the cavity in order to improve mixing and residence time of species [51, 52]. The geometry of these cavities and the injection location greatly affect recirculation within the cavities and thus the residence time of potential fuels, so both of these attributes must be considered carefully.

2.2 Solid Fuels

The combination of scramjets and solid-fuel propulsion systems has gained attention in aerospace engineering due to their potential to achieve hypersonic speeds and their applications in missile systems, and high-speed transportation. Solid fuel ramjets (SFRJs) and scramjet systems (SFSJs) are two propulsion systems that have been individually explored for decades. SFRJs are a subclass of ramjet engines that utilize solid fuel as the combustion source. One of the main advantages of SFRJs is their simplicity and reliability, as they do not require additional fuel delivery systems or fuel pumps, as seen in the schematic in Figure 2.4. The lack of pumps and valves, while reducing complexity, also diminishes the ability to directly change combustion characteristics such as fuel injection location and equivalence ratio. Because of this, more information must be known prior to combustion in order to determine how the thrust and fuel consumption will vary with time. One way to affect these characteristics is by adjusting the fuel grain geometry; however, most of the open literature only shows control over equivalence ratios much less than 1 [2, 53].

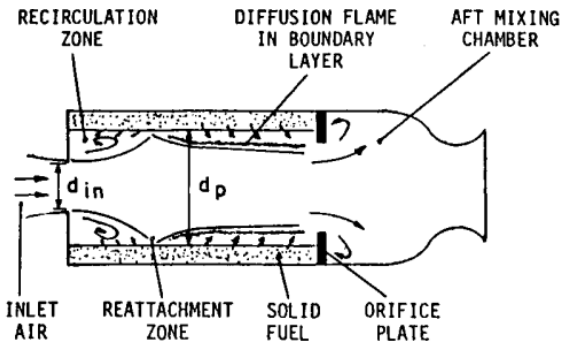
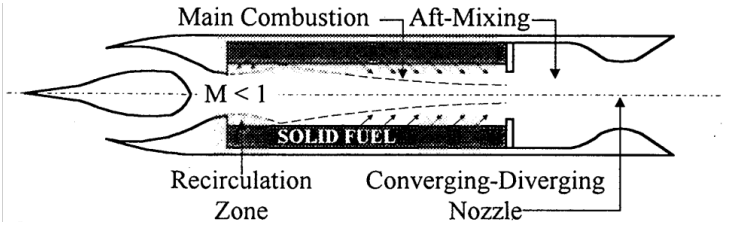


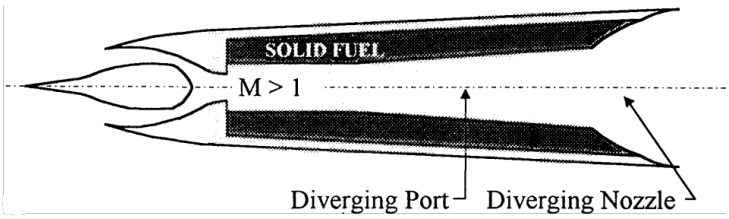
Figure 2.4: Schematic diagram of an SFRJ com bus tor showing the fluid dynamic and combustion characteristic [2]

Also, due to the nature of solid fuels, it is much easier to store for long periods,

which is very desirable for locations where constant restocking is not an option, such as on an aircraft carrier [54]. Solid fuels' increased density also produces an increased volumetric heating value, which reduces the amount of fuel storage space required on an air vehicle. SFRJs have been used in various missiles, such as the AIM-54 Phoenix and the French MICA [55]. While no SFSJs are currently in active use, their theoretical advantages over traditional fuel injection methods are similar to those of the SFRJ, but now applicable in the hypersonic regime [56]. Side-by-side depictions of an SFRJ and an SFSJ can be seen in Figure 2.5, where the SFSJ does not utilize an aft mixing chamber but instead incorporates a diverging nozzle in order to avoid the previously mentioned thermal choking discussed in Section 2.1.2.



(a) SFRJ



(b) SFSJ

Figure 2.5: Configuration of a) subsonic and b) supersonic combustion solid fuel ramjets [3]

Most research on scramjet combustion has involved either liquid hydrogen or hydrocarbons, and until recently, research on SFSJs has been limited in the open literature. Early efforts at demonstrating the SFSJ's capabilities were published toward the end of the 20th century; however, the combustion was also aided by injection of hydrogen upstream [57, 58]. Near the turn of the century, researchers at the Technion [56] were the first to achieve self-ignition and flame holding in an SFSJ using polymethyl methacrylate (PMMA) as a fuel. Shortly thereafter, Cohen-Zur [3] published a continuation of the work where the SFSJ operational range was increased and performance characteristics

were obtained. In 2019, through the use of an arc heater, the simulated flight conditions were expanded to include Mach number 5.5 flight conditions at various altitudes in order to better understand the sustainability of the flame and the aerodynamic aspect of the flow acceleration [59].

A major concern in solid fuel propulsion systems is the changing geometry associated with fuel pyrolysis, which can lead to various phenomena such as varying thrust or blowout. In order to account for this in a numerical model, fuel regression must be properly implemented. The rate of pyrolysis has been shown to be dependent on several factors including oxygen concentration, pressure, and heating rate, where all show a positive correlation with the regression rate [60]. Many polymer pyrolysis models use sublimation to simulate the polymer breakdown into a gaseous monomer; however, they often rely heavily on empirical data and curve fitting, as opposed to modeling physical phenomena [61].

Figure 2.6 displays an example of a typical combustion wave during solid fuel decomposition [62]. On the right side of the figure, one can see the high-temperature flame zone. This ideally occurs after all fuel and oxidizer species have properly mixed and reacted to produce an adiabatic flame at temperature T_F. The gas-phase reaction zone is determined by the convective, diffusive, and reaction times of the fuel and oxidizer species. In the case of greater convection, diffusion, or lower reaction time, one may observe a steeper slope in this section of Figure 2.6 due to the gas-phase reactions. The burning-surface and condensed-phase reaction zones occur near where the solid and gaseous species meet. While the inner portions of the condensed phase do not mix with the air, thermal decomposition can still take place [63]. Material below the decomposition temperature T_D acts as a solid, allowing a conductive thermal wave to travel through it to some initial fuel temperature T_i.

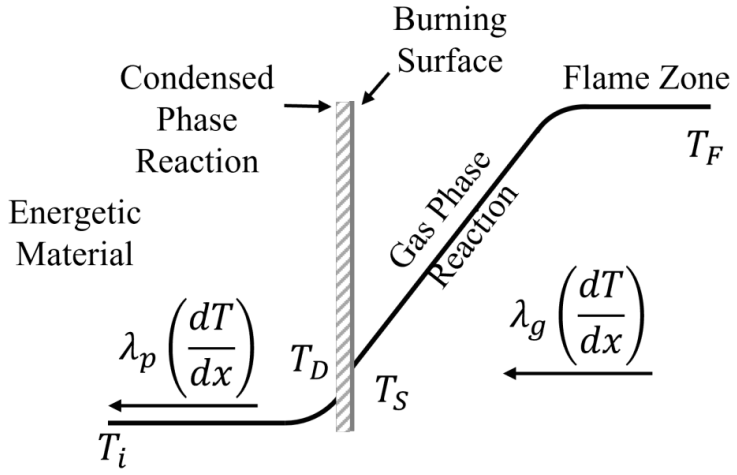


Figure 2.6: Combustion wave for a typical solid fuel [4]

Obviously, the speed at which a solid fuel pyrolyzes is dependent on the heat feedback from the flame zone, so in order to better understand the heat-flux feedback and pyrolysis of solid fuels, counterflow burners are often employed. A traditional counterflow burner consists of gaseous fuel and oxidizer jets impinging axially on one another, thus creating a region of diffusive mixing where combustion occurs near the stoichiometric ratio. This mixing creates a laminar diffusion flame [64]. This counterflow experiment can be modified by using a solid fuel pellet in place of gaseous fuel as seen in Figure 2.7. As the solid fuel becomes gaseous and mixes with the oxidizer, it stabilizes in a flame zone and releases heat. This energy travels via convection and radiation back to the fuel pellet surface, thus pyrolyzing more fuel to continue the cycle. This cycle has been referred to as and continues to be referenced as the "heat-feedback" process. The study of the heat-feedback loop in counterflow fuel pellet scenarios has been investigated by various researchers, such as Young et al. [65], who tracked the regression rate as a function of various factors such as oxidizer temperature, velocity, and composition.

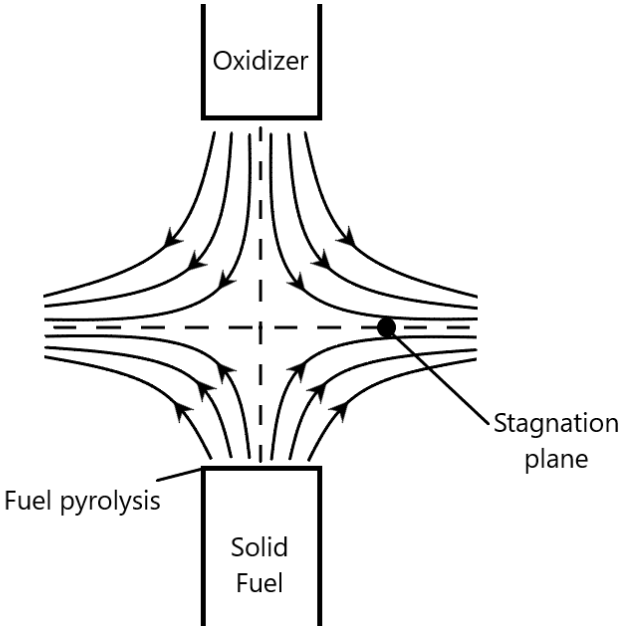


Figure 2.7: Sketch of solid fuel used in counterflow, stagnation flame

2.3 Surface Regression

Because the fuel grain geometry affects the rate at which fuel is pyrolyzed, and thus the thrust of the combustor [3], it is important to understand how the geometry changes with time. Lautenberger and Fernandez-Pello [66] discuss various pyrolysis modeling strategies and emphasize the importance of making sufficient simplifications so that the number of variables remains manageable while not compromising the generality of the model or neglecting the important physics and chemistry behind the problem. In the combustion of sublimating polymers, heat of volatilization ΔH_v is of utmost importance if the model is to accurately predict the regression rate. Unfortunately, it is often difficult to characterize due to the breakdown of polymer chains (decomposition) and the changing of the monomer states (vaporization). The first of these values, decomposition, is often assigned the negative value of the heat required to polymerize the solid fuel. This is a well-known value in constant temperature processes; however, reality dictates a range of values within which decomposition and vaporization actually occur.

Several researchers, such as Gany et al. [5], have attempted to model PMMA decomposition rates using Arrhenius-type equations and energy balances between the heat flux

and the solid's heat of vaporization, such as the one below:

$$\dot{r} = \frac{\dot{q_w}}{\rho_f H_{\text{v,eff}}} \tag{2.1}$$

Where $\dot{r}$ is the regression rate, $\dot{q_w}$ is the heat flux to the wall, ρ_f is the density of the fuel, and $H_{\text{v,eff}}$ is the effective heat of vaporization for a given fuel. As one can see in Figure 2.8, the resulting model does a good job predicting the regression rate, but the PMMA, like all other fuels in this investigation, showed lower experimental regression rates than those predicted by the model.

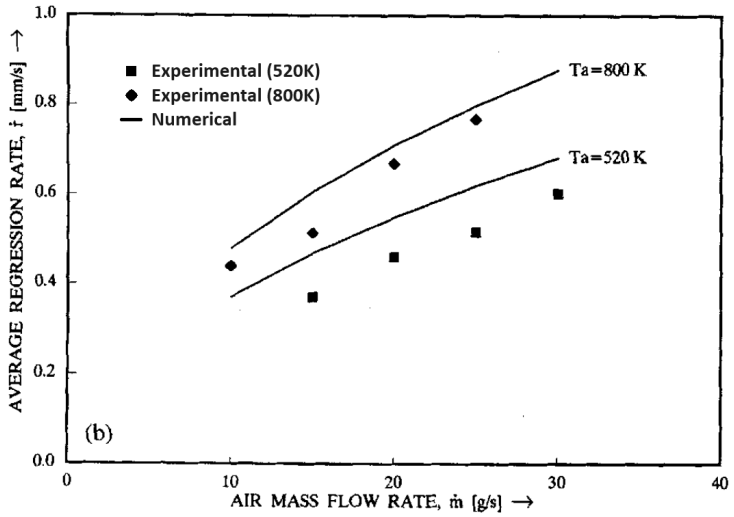


Figure 2.8: PMMA regression rate model using heat of vaporization [5]

2.4 Computational Fluid Dynamics

Computational Fluid Dynamics (CFD) represents a critical advancement in the simulation and analysis of fluid flows, providing insights into the complex dynamics of gases and liquids in motion. This computational tool allows engineers and scientists to model and predict fluid behavior in an array of applications, ranging from aerospace engineering to environmental studies, where direct experiments are either infeasible or prohibitively expensive. The significance of CFD lies in its ability to provide detailed visualizations and quantitative predictions of fluid flow phenomena, such as turbulence, heat and mass transfer, and chemical reactions, which are essential for optimizing the design and per-

formance of engineering systems [67, 68].

In the realm of combustion, CFD plays a crucial role in the design and optimization of combustion chambers for engines and power plants. By simulating the intricate processes of fuel decomposition, mixing, ignition, and combustion across various conditions, CFD helps in improving fuel efficiency and reducing emissions. Lazik et al.'s 2008 research with Rolls-Royce [69] highlights how CFD analysis has been instrumental in minimizing NOx emissions and narrowing down optimal configurations that can then be validated using experimental follow-up investigations. Similarly, for high-speed propulsion systems, such as scramjets, Obula Kummitha's study, "Numerical analysis of passive techniques for optimizing the performance of scramjet combustor" [6], underscores CFD's important role in understanding the complex shock wave patterns (Figure 2.9) and high-temperature gas dynamics, and how wall features can aid in fuel mixing at supersonic and hypersonic speeds. Studies like these are indispensable in visualizing and better understanding the phenomena taking place in complex systems such as the combusting and shock dominant scenarios shown below.

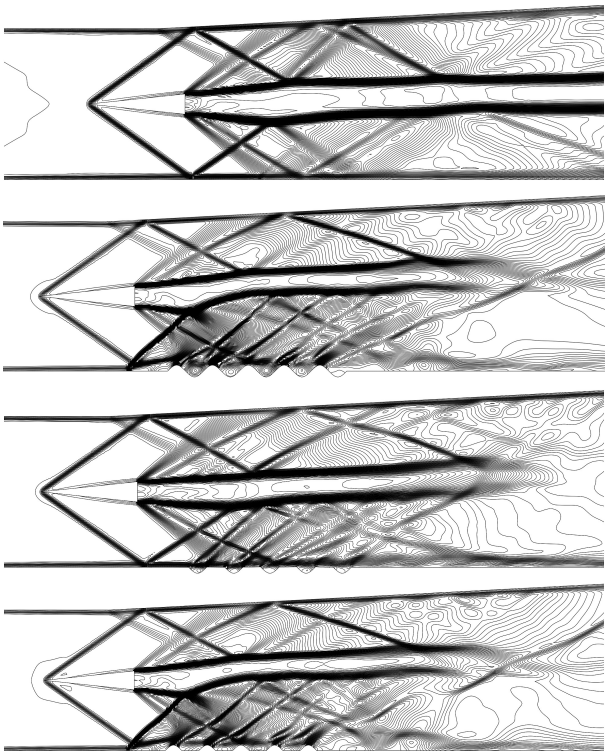


Figure 2.9: Density contours of several combustor geometry simulations performed by Kummitha [6]

The use of CFD in these areas underscores its importance not only in advancing theoretical understanding but also in practical application towards more efficient, safer, and environmentally friendly technologies. The applications of CFD encapsulate a broad spectrum of real world problems with multiple strategies suited for various challenges [70].

2.4.1 Reynolds Averaged Navier Stokes

The Reynolds-Averaged Navier-Stokes (RANS) approach is a fundamental tool in computational fluid dynamics (CFD), especially for modeling turbulent flows in combustion systems and high-speed propulsion applications. RANS equations simplify the complex nature of turbulent flows by averaging the fluid motion over time, which significantly reduces the computational resources required compared to more detailed approaches, such as Direct Numerical Simulation (DNS) or Large Eddy Simulation (LES). Because of the significant reduction in computational cost, RANS can often be used as an initial approach in order to understand the dominating characteristics of a flow field.

In the context of high-speed flight, RANS models have been modified to predict transitional regions on scramjet forebodies [71]. The ability to quickly run large-scale RANS simulations to obtain data like surface heat flux is invaluable in the application of optimizing hypersonic vehicle designs. Researchers have also attempted to use RANS to recreate chemically reacting flows; however, these solutions become very heavily dependent on the turbulence models used, and it is essential to have some preexisting knowledge of the flow field prior to simulation. While an effective and quick tool in predicting flow properties such as flow rate, these models tend to struggle with intermediate species concentrations and temperature profiles due to the assumptions made in the simplified turbulent mixing models [72].

2.4.2 Large Eddy Simulations

Large Eddy Simulations (LES) have emerged as a vital computational fluid dynamics technique, offering a middle ground between the high accuracy of DNS and the com-

putational efficiency of RANS methods. LES is particularly valuable in applications requiring detailed understanding of turbulent flows, such as in combustion processes and high-speed air-breathing propulsion systems, such as ramjets, scramjets, and rotating detonation engines. These applications are critical in advancing propulsion technology but present significant challenges due to the complex interplay of fluid dynamics and chemical reactions under extreme conditions [73].

LES distinguishes itself from RANS by resolving large-scale turbulent structures directly while modeling the effects of smaller scales. This approach allows LES to capture transient phenomena and detailed flow structures more accurately than RANS, which averages these details out. Thus, RANS solutions have shown promise in modeling general flow trends, but transient, quantitative results are far more accurate through the use of LES [74]. For example, LES has been instrumental in studying high-speed combustion applications, where it can account for complex interactions such as turbulence-chemistry coupling, shock waves, and boundary layer effects. The ability to simulate these interactions with greater fidelity makes LES a powerful tool in designing more efficient and reliable propulsion systems [75].

A common geometry seen in high-speed air-breathers is a flameholding cavity. Flame stabilization is necessary to produce sustained combustion, and numerical simulations have been essential in better understanding how these flame anchoring mechanisms help to create recirculation regions and increased residence time of fuel and oxidizer species. LES has been key in understanding the turbulent mixing that occurs in these recirculation zones [76, 77].

Despite its advantages, LES does come with its own set of challenges, primarily related to computational costs and the need for detailed modeling of subgrid-scale (SGS) physics. Many different SGS models exist that have been optimized for various flows; however, due to the various time and length scales involved in supersonic combustion, finding an optimal SGS model can be difficult due to its effects on the mixing timescales and shear stress. Both of these quantities have been shown to affect the SGS turbulence and Mach number, and thus the combustion characteristics in compressible flows [78]. As high-

performance computing resources become more widely available, the accessibility of LES for industrial and research applications continues to improve, facilitating its adoption in a wider range of applications. Yet, ensuring the reliability and accuracy of LES models, especially in the nuanced realm of high-speed combustion, remains a critical area of ongoing research.

2.4.3 Discontinuous Galerkin Solver

Discontinuous Galerkin (DG) methods appeared in the early 1970s from a set of applied mathematics and form a class of numerical methods for solving differential equations. They combine features of the finite element [79] and the finite volume [80] methods and have been used to solve various numerical problems, ranging in nature from hyperbolic to parabolic to elliptic as well as mixed forms in between. While they have been used in a wide range of applications, their primary usage has been in problems containing a dominant first-order term such as the fields of electrodynamics, CFD, and plasma physics [81, 82, 83].

Similar to the continuous Galerkin (CG) method [84], DG utilizes a weak formulation of the finite element method. The distinction between CG and DG methods (and reason for the apt naming) is that while CG uses conforming functions, DG creates a trial space of functions requiring piecewise continuity. This allows DG to encompass more inclusive function spaces than its CG counterpart. In a simple example, we can look at an initial value problem for an ordinary differential equation (ODE) approximation using a DG method [85]. Suppose one is presented with the problem:

$$\frac{d}{dt}\phi(t) = f(t)\phi(t), t \in (0,T), \phi(0) = \phi_0 \tag{2.2}$$

where one wants to approximate ϕ as ϕ_h on the interval $(0,T)$. Using a DG method, one would first find a partition of the interval $(0,T), t^n{}_{n=0}^{N}$ and set $I^n = (t^n, t^{n+1})$ for $n = 0, ..., N-1$. One then searches for a function ϕ_h on the interval I^n with a highest polynomial degree, k^n, such that ϕ_h satisfies:

$$-\int_{I^n} \phi_h(s)\frac{d}{dt}\psi(s)ds + \hat{\phi_h}\psi|_{t^n}^{t^{n+1}} = \int_{I_n} f(s)\phi(s)\psi(s)ds \tag{2.3}$$

for all polynomials ψ of at most degree k^n. In order to fully define this function, one must identify the quantity $\hat{\phi_h}$. One such piecewise definition that would satisfy the function would be:

$$\hat{\phi_h} = \begin{cases} \phi_h & \text{if } t^n = 0 \\ \lim_{\epsilon\to 0} \phi_h(t^n - \epsilon) & \text{otherwise} \end{cases} \tag{2.4}$$

The $\hat{\phi_h}$ term in this example is known as the numerical trace, and the way the user defines this function is crucial due to its ability to affect the consistency, stability, and accuracy.

2.5 Numerical Surface Regression and Grid Adaptation

When it comes to accurately transposing surface regression onto a numerical grid solution, many methodologies exist. Many such approaches have been developed for ablative surface prediction, but due to the differing flow characteristics between ablative surfaces and internal combustion, many rely on the creation or destruction of mesh elements [86, 87]. For relatively uniform recessing surfaces, this approach works well due to the infrequency with which one needs to create additional elements; however, in the presence of large heat gradients like inside a scramjet combustion chamber, the iterative process of creating new surface elements and then updating them several times in order to obtain an optimal mesh becomes more computationally expensive.

A very computationally inexpensive approach is to solve a linear elastic equilibrium problem where a surface is regressed, and an arbitrary elasticity tensor is applied to it, such that a new displacement boundary condition can be applied to the original mesh that is equivalent to the amount of mesh recession [88]. This methodology relies heavily on already knowing the expected surface shape post recession and is likely to smooth out areas of high or low recession unnaturally. One approach to mitigate this smoothing effect is to instead utilize control points when deforming the surface. Several other ablative

deformation codes use these control points by projecting node displacements onto the control points and then reapplying the displacement to the nodes based on the control point movement and weighting function [89, 90]. These methodologies have been shown to perform quite well in both the recreation of the recessed surface and the conservation of cell volume.

In pyrolyzing combustor geometries, the geometry is rarely as simple as those seen in ablative studies, so the use of a single set of control points can become unreliable if careful consideration is not paid to the basis used and original proximity of the control points. Due to this, researchers such as Qiang Li et al. [91] have opted for the previously mentioned re-meshing approach where elements are created and destroyed in order to better resolve the mesh. Codes such as the Mesh Quality Improvement Toolkit (Mesquite) [92], developed by Sandia National Laboratory, provide the ability to optimize a mesh while still utilizing parallel computing. Unfortunately, tools such as these are optimized for interior elements and do not handle surface elements well - especially if the element has been largely skewed or distorted. For this reason, when Li's research group performs re-meshing steps, the parallel CFD steps must be paused while a separate processor generates a new grid. This increases computational costs drastically, so re-meshing is done infrequently which hinders potential fluid/solid coupling and interaction.

A simplified approach to surface regression in solid rocket motors is to treat the mesh as a linearly elastic solid by solving the elastic solid mechanics equations [93, 94]. One such implementation of this methodology was conducted by Boyd and Cross [7, 95] to investigate the HIPPO rocket nozzle shown in Figure 2.10. This work utilized finite rate chemistry in the University of Michigan's LeMANS flow solver [96]. In early work that did not include surface chemistry, the recession prediction was shown to be erroneous, with regression being over predicted by nearly 100% at the throat [7]. The inclusion of surface chemistry was later introduced to greatly improve results [95]; however, this new strategy still produced over prediction of regression rates by approximately 30%. When discussing improvements for future ablating/pyrolyzing grid studies, researchers discussed the incorporation of finite-rate surface chemistry and better material models.

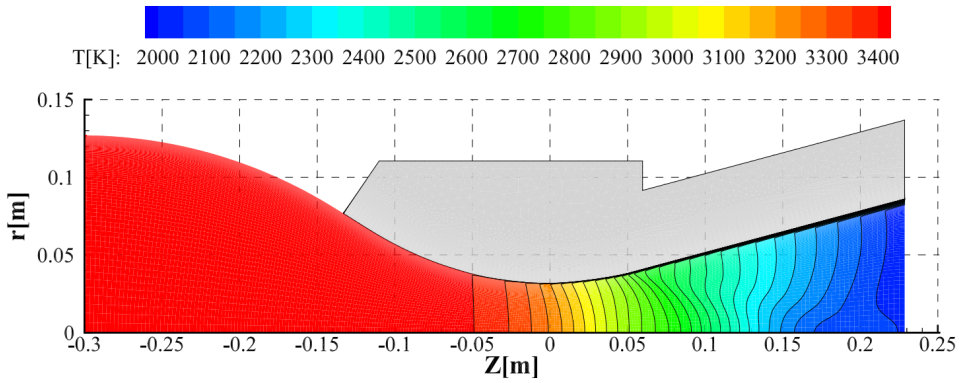


Figure 2.10: Temperature solution for the HIPPO nozzle assuming finite-rate chemistry. Material response domain is indicated by gray region. [7]

2.6 Chemical Reaction Modeling

Properly recreating turbulent mixing is of limited benefit if the appropriate chemistry is not considered. Combustion significantly alters the nature of turbulent mixing, so an accurate chemistry model must be applied to capture energy release within the flow on the correct time scales. This challenge is compounded by the multiple time scales involved in high-speed flow simulations. With speeds varying greatly both above and below the supersonic shear layer, the residence time of species must be precisely tracked. The most reliable method for computing this is through finite rate chemistry (FRC) models [97, 98]. However, FRC models are computationally expensive because each species must be tracked as a scalar, and additional Arrhenius equations must be solved at each time step. The computational cost depends on the fuel breakdown pathways and mechanisms used. Therefore, a strong understanding of numerical combustion reproduction and common strategies in chemical kinetics modeling is crucial.

Chemical kinetics modeling is a sophisticated field that bridges experimental observations with theoretical chemistry, offering profound insights into the dynamics of chemical reactions. At the core of developing these models lies experimental kinetics, where researchers meticulously measure reaction rates under varied conditions to gather data on how different factors like temperature, pressure, and concentration affect reaction velocities. These experimental endeavors provide the raw data necessary to formulate reaction

rate equations, which are fundamental to constructing accurate kinetic models. In order to accurately quantify reaction rates, experimentalists commonly use equipment like shock tubes in order to produce a clearly defined reaction zone at high-speeds [99, 100, 101].

Parallel to experimental efforts, computational kinetics plays a crucial role. Advances in computational power and algorithms allow scientists to simulate complex chemical reactions at the molecular level [102]. Methods such as molecular dynamics simulations provide detailed insights into the potential energy surfaces, transition states, and molecular interactions that govern chemical processes. By combining these computational predictions with experimental data, kinetic models can achieve a higher degree of accuracy and predictive power.

The application of chemical kinetics modeling spans a broad spectrum. In combustion engineering, for example, these models are crucial for designing more efficient engines with lower NOx and soot emissions, directly impacting environmental sustainability and energy efficiency [103].

Though several methods exist to model combustion, most utilize pre-built chemical "mechanisms." These mechanisms are constructed via the use of both chemical and experimental trials as previously mentioned and define specific reaction rate, activation energies, and transport properties of the mechanism's species. A generally, the more complex the fuel or oxidizer, the more species and reactions are required to properly define the molecules' breakdown. A visualization of this trend can be seen in Figure 2.11 where the most complex mechanisms shown (top right of plot) describe the breakdown of methyl stearate ($C_{19}H_{38}O_2$) [104]. Several less expensive mechanisms not shown in Figure 2.11 describe the breakdown of hydrogen such as the Princeton Li-Dryer mechanism [105] which only includes nine species and twenty one reactions.

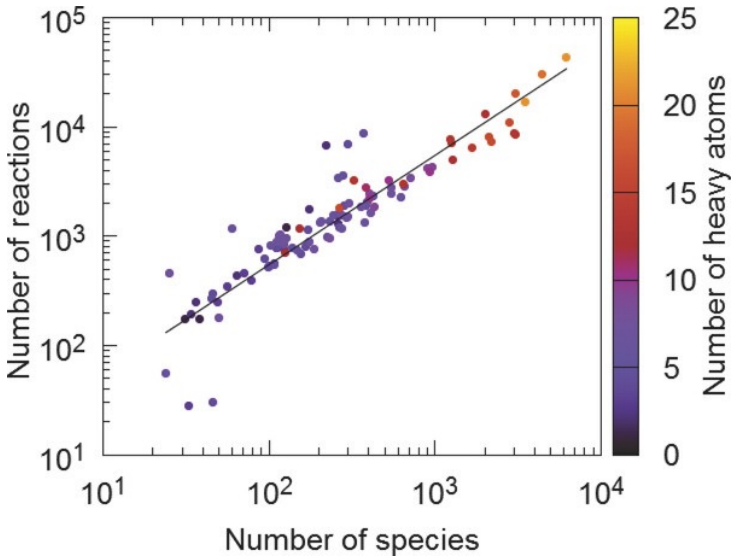


Figure 2.11: Model sizes: number of reactions as a function of the number of species for gas phase kinetic models of pyrolysis, oxidation, and combustion processes. The secondary axis is the number of heavy (non-hydrogen) atoms in the reactant molecule(s) [8]

For many applications where the flow is extremely fast or slow, assumptions can be made to greatly aid in computational combustion. For example, when the flame speed is much faster than the flow speed, instantaneous reactions can be assumed [106]. This assumption is valid in certain regimes due to the time required for reactants to fully decompose into products is much smaller than the transport scales of the flow. On the opposite end of the spectrum when the time scales associated with the flow speed are much smaller than the time scales of combustion (such as in hypersonic flow), the chemical reactions can be considered "frozen" [107]. In this scenario, chemical reactions do not occur because it is assumed that they do not have the residence time required to do so. Unfortunately, there are scenarios where neither of these assumptions are valid due to various time scales being modeled in a single domain. In this case, one must more accurately represent the time scales of combustion in order to predict where heat release occurs.

In the scenarios where instantaneous or frozen chemistry cannot be assumed, finite rate chemistry (FRC) modeling can be used [108]. FRC represents an intricate approach to simulating chemical reactions, distinguishing itself by meticulously accounting for the individual rates at which chemical species react. This detailed consideration is crucial for

accurately depicting the dynamics within reactive flows, particularly in systems where chemical reactions significantly influence the overall behavior, such as in combustion processes or atmospheric chemistry.

At the heart of developing finite rate chemistry models lies the integration of comprehensive chemical kinetics data — derived both from experimental investigations and theoretical calculations. This data includes reaction rate coefficients, activation energies, and species concentration dependencies, which are paramount for constructing reaction mechanisms that can predict the outcome of complex chemical interactions under various conditions [109].

The development and refinement of finite rate chemistry models are heavily reliant on advancements in computational capabilities. High-performance computing allows for the simulation of increasingly complex reaction mechanisms involving numerous species and reactions, providing a more nuanced understanding of chemical processes. Moreover, the integration of machine learning and data analytics into model development is beginning to offer new pathways for enhancing model accuracy and predictive power [110].

Unfortunately, despite the advances in computational capabilities and new involvement of machine learning, FRC can become very expensive in larger mechanisms. In order to understand how computationally expensive these FRC simulations can become, let us begin by looking at the simple 3D Euler equations without tracking any species or chemistry modeling. The five equations in vector form (one continuity, three momentum equations, and one energy equation) can be written in the simple form below [111].

$$\frac{\partial \bar{U}}{\partial t} + \frac{\partial \bar{F}}{\partial x} + \frac{\partial \bar{G}}{\partial y} + \frac{\partial \bar{H}}{\partial z} = \bar{J} \tag{2.5}$$

Where

$$\bar{U} = \begin{Bmatrix} \rho \\ \rho u \\ \rho v \\ \rho w \\ \rho e_t \end{Bmatrix}, \bar{F} = \begin{Bmatrix} \rho u \\ \rho u^2 + p \\ \rho uv \\ \rho uw \\ \rho u h_t \end{Bmatrix}, \bar{G} = \begin{Bmatrix} \rho v \\ \rho uv \\ \rho v^2 + p \\ \rho vw \\ \rho v h_t \end{Bmatrix}, \bar{H} = \begin{Bmatrix} \rho w \\ \rho uw \\ \rho vw \\ \rho w^2 + p \\ \rho w h_t \end{Bmatrix} \tag{2.6}$$

, $\bar{J}$ is a source term that can include effects such as viscosity, and $u, v,$ and w are the velocity components of the $x, y,$ and z Cartesian directions (respectively), ρ is the fluid density, p is the pressure, e_t is the total energy, and h_t is the total enthalpy. With these equations, one can solve continuum fluid dynamics problems without chemistry effects and assuming an ideal fluid. If one wanted to track species inside the fluid using diffusion, for each species added, the following values would need to be added to the $\bar{U}, \bar{F}, \bar{G},$ and $\bar{H}$ vectors for each species added:

$$\bar{U} = \left\{ \rho Y_i \right\}, \bar{F} = \left\{ \rho u Y_i + \mathcal{D} \frac{\partial Y_i}{\partial x} \right\}, \bar{G} = \left\{ \rho v Y_i + \mathcal{D} \frac{\partial Y_i}{\partial y} \right\}, \bar{H} = \left\{ \rho w Y_i + \mathcal{D} \frac{\partial Y_i}{\partial z} \right\} \tag{2.7}$$

Where Y_i is the mass fraction of species i and $\mathcal{D}$ is the diffusion coefficient of a given species in a mixture.

On top of this, if one wished to include reactions of these tracked species, a source term, $\dot{\omega}_i$ would need to be introduced such that species can be created and destroyed. This source would have as many terms as reactions it is involved in within the mechanism. For example, the regular Euler equations shown in Equation 2.6 include five equations. Using a very simple mechanism, lets take Li-Dryer's hydrogen mechanism, the number of equations in Equation 2.6 would become eleven - more than double the original. If chemistry was included and source terms were computed, each $\dot{\omega}_i$ would include around an additional 10-14 reactions needed to be solved in order to determine the individual specie's creation/destruction rate. While this is viable using a simple hydrogen mechanism, it is not hard to comprehend how expensive this can become on larger mechanisms. For example, using FRC to simulate the breakdown of methyl stearate using the mechanism

created by Oliver et. al. [104] would require over six thousand tracked species and almost four million reactions. Modeling anything on a large scale with this method would likely take several lifetimes of continuous simulation in order to obtain results.

2.6.1 Flamelet-Progress Variable Approach

Because of the issues described above, more efficient approaches have been pursued. Flamelet generated manifold (FGM) models have been studied by both Pierce and Moin [9], Oevermann [112], and others to account for turbulent mixing and compressible effects. FGM models utilize one-dimensional, counterflow models to characterize stable laminar diffusion flames. This allows the user to map the themochemical properties, ϕ, as a function of the mixture fraction, Z, instead of the physical space. The mixture fraction is the ratio of fuel to oxidizer species such that it is one at the fuel surface and zero in the oxidizer and this must be monotonic such that a single solution exists in the transformation $Z(x)$ to $x(Z)$. Figure 2.12 shows an example methane-air flame where one can see the max temperature is located in the fuel-lean location of approximately $x/L = 0.15$, and it is easy to see the monotonic relationship between the mixture fraction and physical space. Multiple states of the flame can be simulated by altering the strain rate and thus the dissipation, χ, at the flame stoichiometric location. The dissipation is generally mapped to the mass fraction of a species or group of species. In the current work, the species chosen was CO_2 due to the monotonic relationship to dissipation; however, there are other common choices including H_2O, CO, and HO [113].

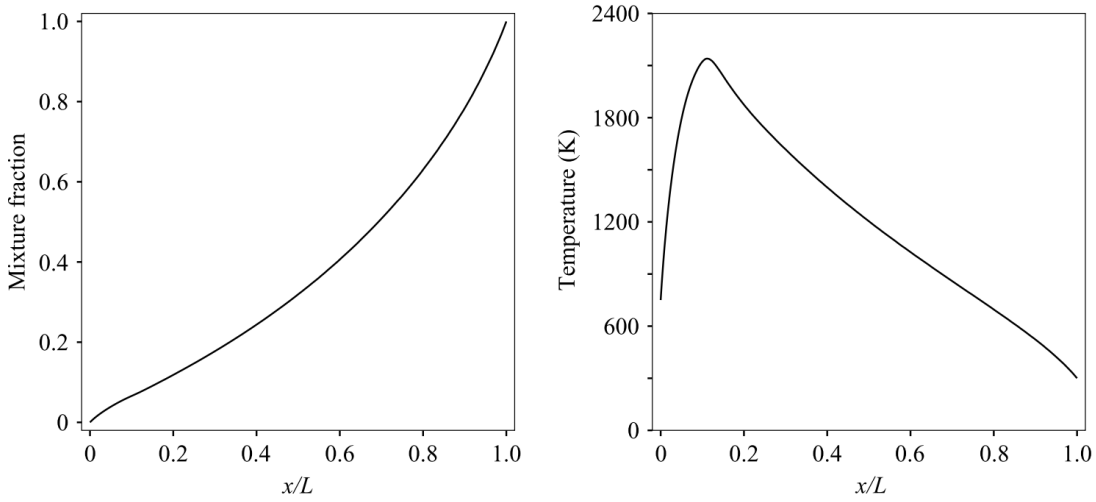


Figure 2.12: Mixture fraction and temperature from a steady-flamelet solution in physical space. Methane–air combustion [9]

This allows the flame properties to become a function of $\phi(Z, \chi)$. All states of a laminar flame can now be represented, and the turbulent flame can be represented as wrinkled laminar flames using a presumed joint probability distribution function (PDF). The mixture fraction and dissipation are independent of each other, their PDFs can be taken independently such that the mean mixture fraction, $\bar{Z}$, and mixture fraction variance, $\bar{Z''}^2$, can be introduced. All states of a turbulent diffusion flame are now represented by the function $\phi(\bar{Z}, \bar{\chi}, \bar{Z''}^2)$. $\bar{\chi}$ can be mapped to a scaled progress variable, $\bar{C}$ such that this is track instead of $\bar{\chi}$. Scalar transport equations can be used to track $\bar{Z}$ and $\bar{C}$ inside a flamelet simulation given by

$$\begin{cases} \frac{\partial \bar{\rho}\bar{Z}}{\partial t} + \boldsymbol{\nabla} \cdot \left(\bar{\rho}\bar{u}\bar{Z}\right) = \boldsymbol{\nabla} \cdot \left(\bar{\rho}(\bar{\alpha_Z} + \alpha_t)\boldsymbol{\nabla}\bar{Z}\right) \\ \frac{\partial \bar{\rho}\bar{C}}{\partial t} + \boldsymbol{\nabla} \cdot \left(\bar{\rho}\bar{u}\bar{C}\right) = \boldsymbol{\nabla} \cdot \left(\bar{\rho}(\bar{\alpha_C} + \alpha_t)\boldsymbol{\nabla}\bar{C}\right) + \bar{\rho}\bar{\omega_C} \end{cases} \tag{2.8}$$

Now, instead of tracking multiple species as is required in the FRC model, only two scalars must be tracked. Also, instead of solving reaction equations to obtain the production rate of all species, a pre-tabulated manifold is used to search for the appropriate production rate of the progress variable, $\bar{\omega_C}$. Creation/destruction of all other species can also be found in this table in order to balance the enthalpy equation and account for compressible flow effects [112].

Chapter 3

Solid Fuel Decomposition and Mechanism

3.1 Counterflow Burner

The chemical mechanism used here was based on 89 species and 629 reactions scheme appearing in previously published work [114], with several changes to the transport properties based on newly obtained results in computational chemistry as well as the added MMA condensed species. The flamelet and passive scalars models were implemented in a framework that facilitates the solution of multi-physics and multi-fidelity problems by interpolating the source terms for energy and mass exchange at the boundaries between physics zones.

This mechanism was implemented in Cantera [115] with a few variations from the original formulation mainly regarding adjustments to the transport properties and the kinetic rates of C3-C5 species as reflected by published data. The NASA-7 transport model parameters have been re-evaluated to better fit the data range without discontinuities, which prevented the Newton method from converging in the evaluation of the response of the fuel pyrolysis to changes in strain rate. Such a response is used to approximate the flamelet tabulated rates beyond the maximum strain conditions.

Self-similar counter-flow diffusion flames were obtained at steady state and in one-dimension using a Newton method algorithm with adaptive mesh refinement. The species

at the fuel inlet were interpolated from previously run foam simulations at a given heat flux and were mainly comprised of gaseous MMA ($C_5H_8O_6$). The oxidizer inlet ejected air comprising O_2 with molar fraction 0.21 and N_2 with fraction 0.79.

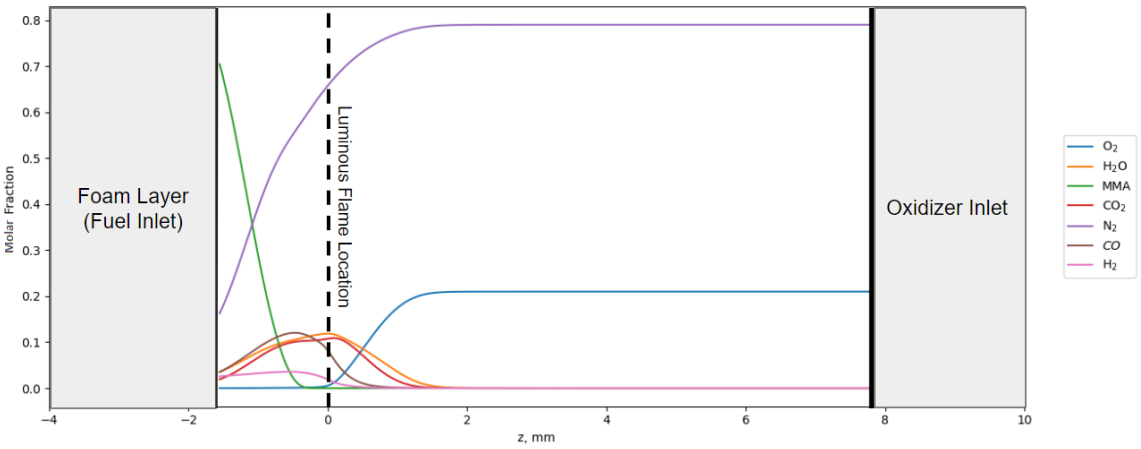


Figure 3.1: Computed species mole fractions at oxidizer inlet conditions of 573 K and 0.432 $kg/(s * m^2)$

Several species concentrations were plotted for the reader's benefit in Figure 3.1. The z axis in this case stretched between the oxidizer (right) and fuel (left) inlets and referred to the distance in millimeters from the maximum flame temperature. Note that many species were present in the $-2mm < z < 1mm$ region near the flame; however, they did not exist in large quantities and are thus not shown.

3.2 Sublimation Model

Initially, a sublimation model was used to predict the regression rate of the solid fuel PMMA pellet where the solid phase thermal decomposition was calculated as a first-order decomposition reaction [116] by solving the multiphase flow in the solid using a one-dimensional approach with gasseous MMA ($C_5O_2H_8$) as the fuel. A fixed point iteration method was used to balance the heat flux and the sublimation rate until equilibrium was established and the flame was stabilized. The heat of volitalization is known to greatly affect fuel the regression rate, and as seen in the works of Peterson [117] and Dakka [118], the range for ΔH_v is quite large and has a lower bound of slightly exothermic in a pure oxygen environment and increases to 1080 kJ/kg when observed in a nitrogen rich

environment. Because of this, several values of ΔH_v were simulated, but a value 941 kJ/kg is shown below due to the temperature profile's close resemblance to results recorded by Seshadri and Williams [119]. Unfortunately, as one can see in Figure 3.2, the model poorly predicted the regression rate of the solid fuel with an offset of approximately 20% where the error bars represent the heat of volitalization range. All experimental counterflow comparisons shown herein were drawn from the works of Pace and Jessup [10].

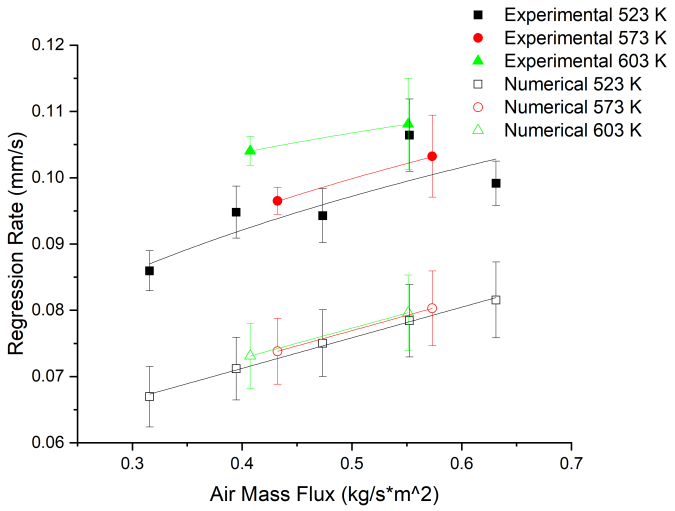


Figure 3.2: Experimental vs sublimation model results

3.3 Melt Layer Model

Because the experiments under discussion revealed that the foam thickness is comparable to the flame standoff distance, a foam model was implemented between the gas and solid phases of the fuel. It is also important to note that while thermal decomposition of PMMA produces mainly 90% methyl methacrylate (MMA, $C_5H_8O_2$), approximately 10% of the products are carbon dioxide [120]. This means decomposition begins to occur inside the foam layer making it an important part of the physics involved. The volumetric fraction of these two compounds does not vary significantly in the range of surface temperatures relevant to (sc)ramjet combustion $400 - 700°C$, although it does vary weakly with pressure [121]. The foam model used is based on the work of Beckstead and Yang [63] and utilizes a void fraction, ϕ_f, ratio inside the foam. This is the area

ratio of gaseous bubbles to condensed, liquid MMA; therefore, it ranges from zero at the solid/foam interface to 1 at the foam/gas surface. The value of ϕ_f is defined as

$$\phi_f = \frac{A_g}{A} \tag{3.1}$$

where A is the cross-sectional are of the fuel, and A_g denotes the area inside the cross section consisting of gaseous species.

The presence of bubbles inside the foam layer allows for evaporation and decomposition before the MMA reaches the gas interface. The net evaporation rate, $\dot{w}_{evap}$, is a function of the specific surface area, A_{sp}, and the mass flux, $\dot{m}_{net}$ as shown below:

$$\dot{w}_{evap} = A_{sp}\dot{m}''_{net}. \tag{3.2}$$

The mass flux and specific surface area are found using the following equations:

$$A_{sp} = (36\pi n)^{1/3}\phi_f^{2/3}, \phi_f < 1/2 \tag{3.3}$$

$$A_{sp} = (36\pi n)^{1/3}(1-\phi_f)^{2/3}, \phi_f > 1/2 \tag{3.4}$$

$$\dot{m}''_{net} = s\frac{1}{4}\sqrt{\frac{8R_uT}{\pi W_{MMA}}}\frac{pW_{MMA}}{R_uT}\left(\frac{p_{v,eq}}{p} - X_{\mathrm{MMA}}\right) \tag{3.5}$$

The sticking coefficient is the probability of a molecule sticking to a surface after collision (ranging from 0-1) and is usually a function of temperature, but a fixed value was used in this study. The number density, n, is defined as the number of bubbles of any size per cubic meter of the foam and commonly ranges $10^3 - 10^5$ cells/cm^3 in polymers. Because little empirical data could be found for bubble number density of MMA at the temperatures observed in this work, several values were simulated in order to gain a more comprehensive idea of the value's effects, and this is explained in more detail in Section 3.3.1. The total mass loss by the solid phase is obtained by adding the thermal decomposition rate $\dot{m}'$ to the net evaporation rate. Thermal decomposition is necessary to start the process of fuel gasification, since the initial volume fraction at the glass transition temperature is assumed zero and the rates in eq (3.3) are null. The latter

is obtained assuming a linear pyrolysis model [122]. The rates of Korobeinichev et al. [123] are used,

$$K(T) = k_0 \exp\left(-E_0/(RT)\right), \tag{3.6}$$

$$\dot{m}' = \rho_v K(T), \tag{3.7}$$

where $\rho_v = \rho_c\,(1-\phi_f)$ is the density of the multi-phase foam and $\rho_c = 1190\ \frac{\text{kg}}{\text{m}^3}$ is the density of the molten polymer at the glass transition temperature [124]. The parameters of the thermal decomposition relation are $k_0 = 10^{12.3}\ \text{s}^{-1}$ and $E_0 = 171.4$ kJ/mol [123]. The evaporation model is strongly coupled to the gas phase chemistry in the bubbles because of the last term in eq (3.5), which quickly saturates $\frac{p_{v,eq}}{p} \to 1$ and is zero if X_{MMA} does not decrease from the initial evaporation value of one. The following expression for the vapor pressure of MMA in terms of the local bubble temperature T is adopted in this study [125],

$$\log_{10}\left(\frac{p_{v,eq}}{1\ \text{bar}}\right) = 5.3 - \frac{1945.56\ \text{K}}{T - 7.569\ \text{K}}. \tag{3.8}$$

The conservation equations inside the foam are written in the following form in which the liquid (condensed phase) phase is assumed of constant composition and the mass diffusion in the multi-phase foam bubbles is neglected. The equations differ slightly from what was reported elsewhere [63].

$$\frac{\partial}{\partial x}(\phi_f(\rho_g u_g) + (1-\phi_f)(\rho_c u_c)) = 0 \tag{3.9}$$

$$\frac{\partial \phi}{\partial t} + u_c \frac{\partial \phi}{\partial x} = (1-\phi)\frac{\partial u_c}{\partial x} - \frac{\dot{w}_c}{\rho_c Y_c} \tag{3.10}$$

$$\phi \frac{\partial Y_{g,k}}{\partial t} + \phi u_g \frac{\partial Y_{g,k}}{\partial x} = \frac{(\dot{w}_c Y_{g,k} + \dot{w}_{g,k}\phi_g - \delta_{g,MMA}\dot{w}_c)}{\rho_g} \tag{3.11}$$

$$\rho c_f = (1-\phi)\rho_c c_c + \phi \rho_g c_g \tag{3.12}$$

$$\rho u_f c_f = (1-\phi)\rho_c u_c c_c + \phi \rho_g u_g c_g \tag{3.13}$$

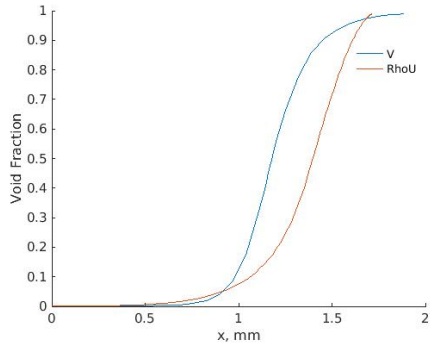
$$\lambda_f = \frac{(1-\phi)\rho_c u_c \lambda_c + \phi \rho_g u_g \lambda_g}{(1-\phi)\rho_c u_c + \phi \rho_g u_g} \tag{3.14}$$

$$\rho_f c_f \frac{\partial T}{\partial t} + \rho_f u_f c_f \frac{\partial T}{\partial x} = \frac{\partial}{\partial x}\left(\frac{\lambda_f \partial T}{\partial x}\right) - \phi \sum_j \dot{w}_{g,j} h_{g,j} - \dot{w}_c (h_{MMA,l} - h_{MMA,g}) \tag{3.15}$$

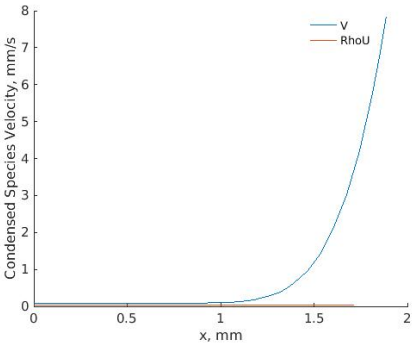
where u is the velocity and the subscripts $_{g,c}$ denote the gaseous and condensed species, respectively, and δ is the Kronecker delta. Two different momentum models were explored inside the foam layer. Model 1 assumed no momentum transfer between the bubbles and condensed region when solving the conservation equations inside the foam, so bubbles were modeled as passing through the liquid without viscous effects. This model will be referred to as the "RhoU" model because the mass flux at each node in the simulation was solved such that $(\rho \times u)_g = (\rho \times u)_c$ at each node point in the simulation. In this first model the condensed species velocity is assumed constant in space and equal to the value at the melting point, which is evaluated by simple mass conservation balance with the solid material mass flow rate. Thus, the partial derivative of the condensed velocity u_c is neglected in eq (3.10). While this model is intuitive, combustion in the multiphase is insignificant, and the foam additions do not affect the regression rate significantly. The second model, referred to as the "V" model, assumes a bubble driven flow in which the condensed, liquid MMA was forced to move with the speed of the bubbles. The conservation equation in this model used $u_g = u_c$ such that the mass flux of gas and condensed species was not equivalent at every point in the foam layer. The main feature of the latter model is the reduction in the speed of the bubbles in the foam layer near the solid-liquid interface.

Plots of ϕ_f, liquid MMA velocity, temperature, and MMA concentration inside the foam layer are included in Figure 3.3 in order to help the reader better understand the transition zone between the solid and gaseous fuel regions. One can see that the "V" model produces a slightly thicker foam layer in comparison to the "RhoU" model. Even though it can be seen that condensed species pass through the foam more quickly in 3.3b, this forces the bubbles to slow down thus allowing the gaseous MMA more time to

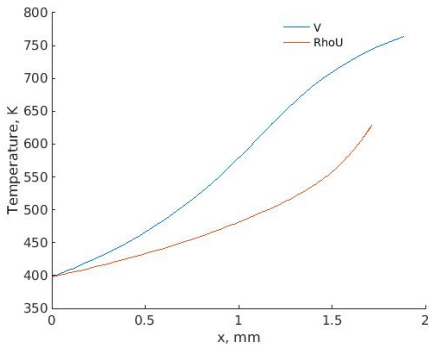
decompose in comparison to the "RhoU" case where the bubbles can pass unimpeded. It can be seen in Figure 3.3c that the foam is able to reach higher temperatures even at the same heat flux to the surface. This further contributes to the decomposition of MMA in the foam layer. The results of the bubble velocity and temperature effects can be seen in 3.3d where the mass fraction of MMA in the foam layer decreases much more rapidly in the "V" model.



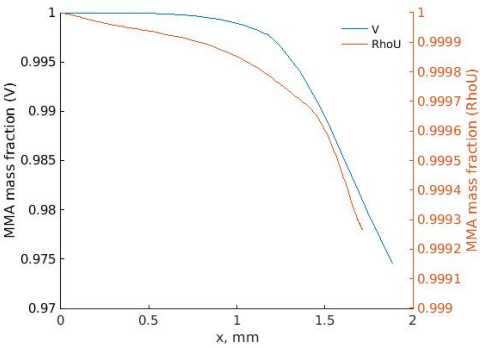
(a) ϕ_f in Foam Layer



(b) U_c in Foam Layer



(c) Temperature in Foam Layer

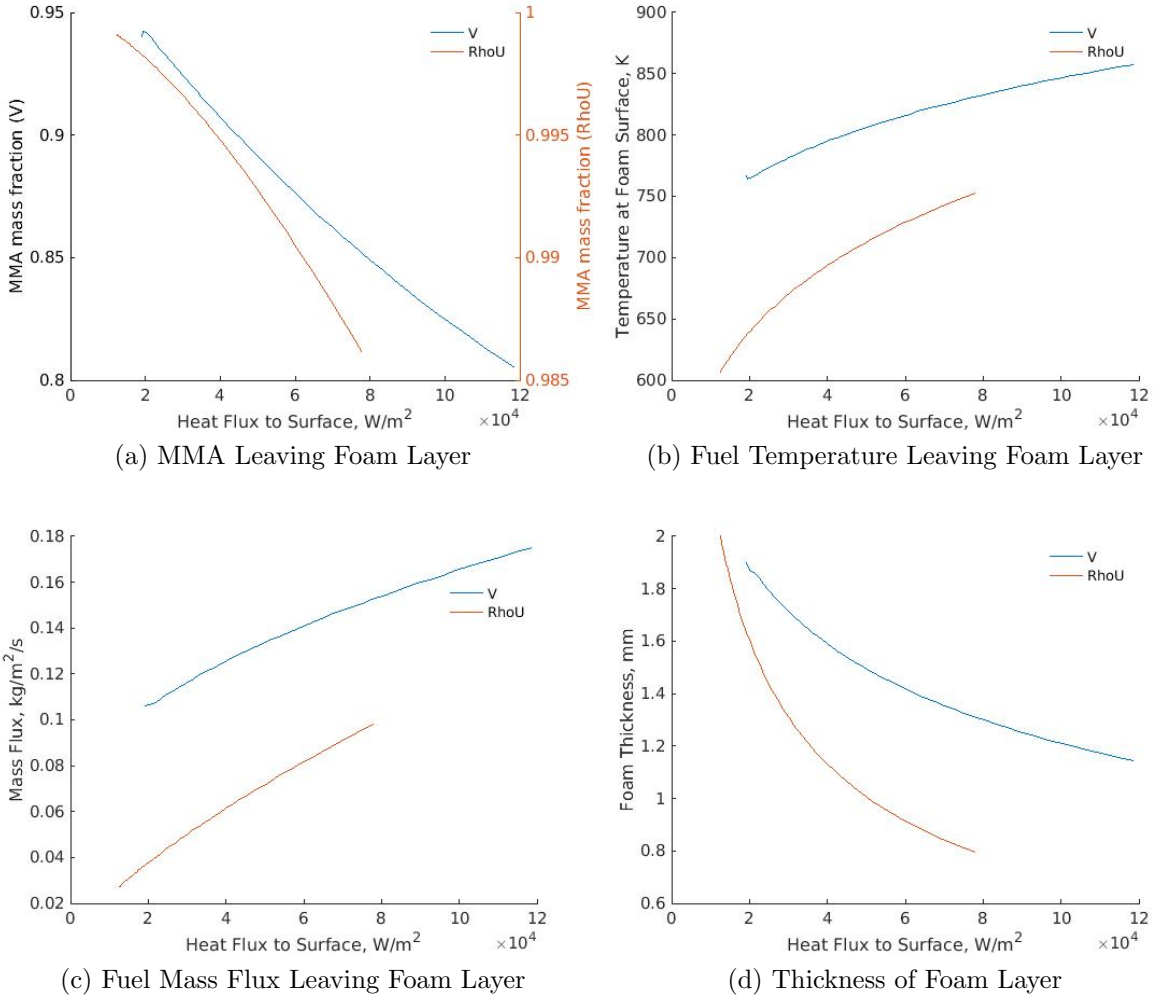


(d) MMA in Foam Layer

Figure 3.3: Comparison of two models inside a foam layer with heat flux of 17.38 kW of heat flux applied to surface

The foam region and counterflow flame regions were solved independently. A fixed point iteration method was used to find the foam depth and surface temperature as well as species concentrations and velocities at the gas interface when provided with a given heat flux to the foam surface. This provided a table of values with surface heat fluxes and corresponding fuel inlet conditions for the counterflow simulation which greatly increased run times in comparison to a fully integrated case. The curves being fitted are the backbone of the integration of the foam model into the LES computations, as described

in Section 4 below, and are shown in figure 3.4. The trends previously discussed in 3.3(d) still hold at other values of heat flux, or q_{gas} in this case. That is, the MMA mass fraction output is much lower, the temperature is higher, and the thickness is greater for the "V" model at the exit when compared to the "RhoU" model.



(a) MMA Leaving Foam Layer

(b) Fuel Temperature Leaving Foam Layer

(c) Fuel Mass Flux Leaving Foam Layer

(d) Thickness of Foam Layer

Figure 3.4: Fuel inlet conditions as a function of mass flux

3.3.1 Effect of Foam parameters on Regression Rate

Because the values of n can vary greatly in MMA due to multiple factors [126], and since the exact value is not well understood for the operating conditions observed in this work, it was assumed to be a constant value throughout the foam. The sticking coefficient s is another parameter that was set as a constant within the foam layer. A range of reasonable values were explored for n and s in the counterflow simulations.

Sticking coefficients generally range from 0.1 to 0.5. The true value of the sticking coefficient, like the true momentum transfer within the foam layer, likely lies between these two values. Nucleation density, n, is commonly studied in polymers due to the unique material properties that can be obtained at high void fractions, ϕ_f. Unfortunately, because large void fractions are ideal for these studies and the nucleation density tends to increase with pressure, most research focuses on producing nanocellular bubbles at high pressure and CO_2 air composition [127]. Strong correlation between the pressure and bubble density was found by [128]; however, the pressure data only extended to pressures ranging from $5.17 - 34.48$ MPa which far exceeds the atmospheric 0.101 MPa produced by the current experiment. Nucleation density increases with pressure, and a 6 MPa pressure was shown to correlate to a cell density of roughly 10^6 cells/cm^3, so it can be assumed the nucleation density in the counterflow experiment discussed herein would not exceed this value. An attempt was made using a power law function to estimate the nucleation density at 0.101 MPa, but this predicted a bubble density on the order of 10^{-4} cells/cm^3 which was clearly not the case in this experiment [10] due to the observation of multiple bubbles inside a foam layer smaller than a cubic centimeter at any given time. Thus, due to the vastly different foaming conditions in the present experiment in comparison to past studies, the nucleation density was estimated using an optical camera to analyze high-speed frames and determine the number of visible bubbles in the foam layer. The high-resolution image analysis leads to a conservative approximation of 2×10^3 cells/cm^3, but due to the location of the diffusion flame and resolution of the camera, a large uncertainty was assumed ranging from $10^3 - 10^5$ cells/cm^3 and sensitivity analysis was preformed.

The effect of the variation in regression rate versus the bubble density and the sticking coefficient is shown in Figure 3.5 using the baseline conditions and a volumetric flow rate of air $\dot{Q}$ equal to 2 liters per minute [10]. Note, the diameter of the air feeding tube is 9.41 mm, so the relation between the area-averaged velocity and $\dot{Q}$, expressed in liter per minutes, is $\bar{V} = 0.2397 \times \dot{Q}$ m/s. Laminar plug flow (or top hat velocity profile) conditions are then applied to evaluate the center-line velocity, which is used in the

similarity analysis of the flame-foam system.

Important observations about these plots are that the presence of the foam increases the regression rates, that the sticking coefficient has a stronger effect on the regression rate than the bubble density, and that the high momentum transfer model "V" supports generally higher regression rates than the low transfer counterpart, because of the increase in fuel residence time in the thermal wave.

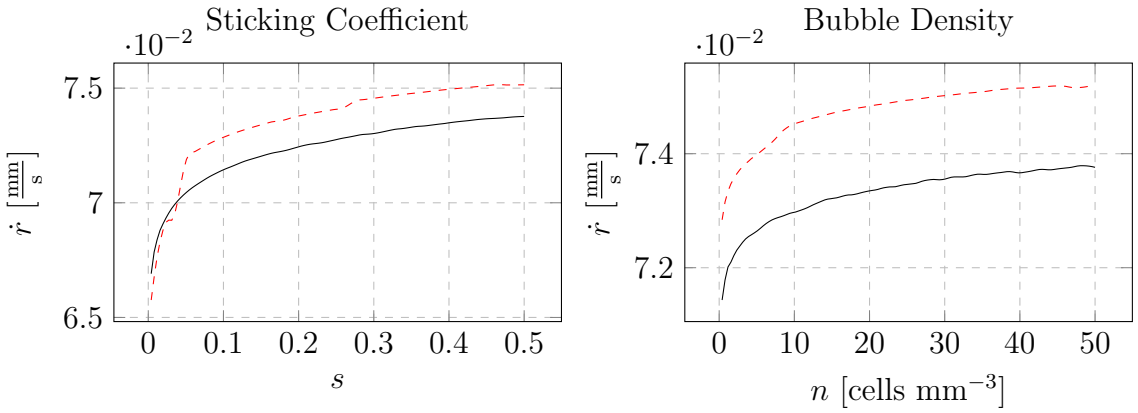


Figure 3.5: Effect of foam parameters on the burn rate in nominal counter flow conditions. The left plots has $n = 50\text{mm}^{-3}$, the right plot has $s = 0.5$; legend: — "RhoU"; - - - "V".

3.3.2 Comparison of Regression Rate and Flame Stand off versus Experiments

The foam parameters introduced in the previous section were fixed to $s = 1/2$ and $n = 50$ cells mm^{-3}, and the "V" model was used in all computations reported in the following sections. The difference between the two models are small, yet the large momentum transfer model outperforms the low momentum counterpart in all the comparisons investigated; thus it is selected as baseline.

The original and modified mechanism are compared with each other and experiments [10] in Figure 3.6. The flame standoff distance is evaluated in the computations as the location of the maximum chemical heat release. The modified mechanism does a good job in reproducing both experimental datasets.

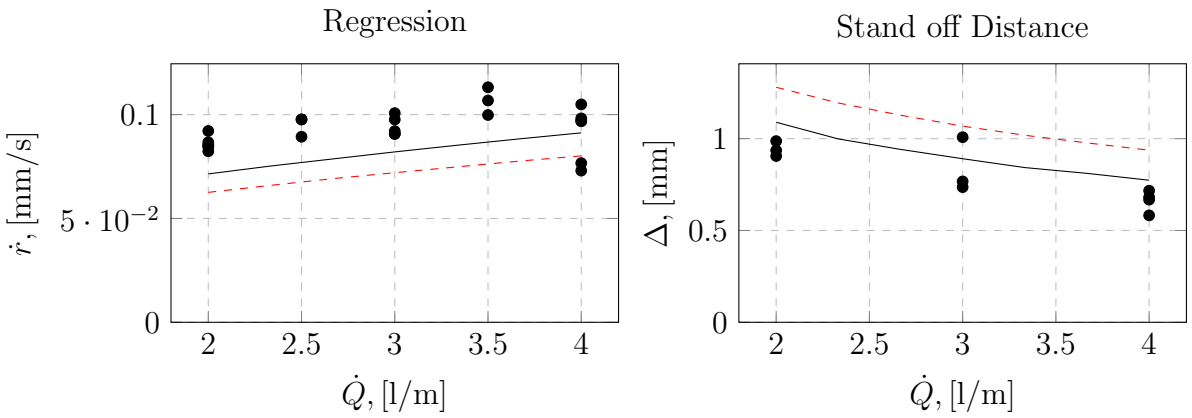


Figure 3.6: Validation of mechanism comparing the regression rate and flame standoff distance versus experiments. Legend: — Modified; --- Original, (●) Measurements. [10]

This multi-phase modeling effort led to the description of the PMMA regression rate based on the heat flux to the surface. Conservation of both the convective and diffusive fluxes at the burning interface and the assumption that species diffusion is not important in the foam layer [63] lead to expressing the regression rate, the mass and energy flux at the interface in terms of the conductive heat flux $q \equiv -\lambda \partial T/\partial n$ evaluated at the boundaries of the simulation domain (the normal $\vec{n}$ points outside the fluid domain). The wall regression model is clearly non-linear due to the variation of the surface temperature with the regression rate. The relationship between heat flux, regression rate, and surface temperature at the foam-gas interface is plotted in Figure 3.7.

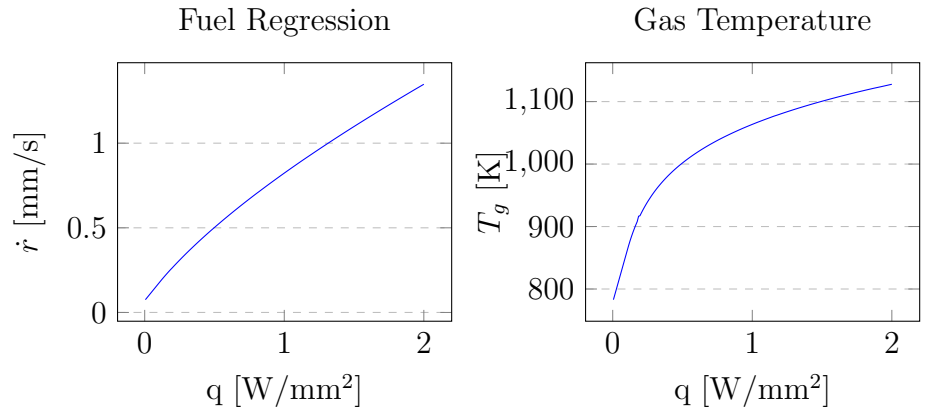


Figure 3.7: Foam layer solid decomposition model.

Chapter 4

Discontinuous Galerkin Solver

A novel Discontinuous Galerkin Navier Stokes solver has been implemented to handle complex regressing geometries with coupled heat conduction. The solver is built on top of the SU2 framework [129].

The main drawback of flamelet and flamelet-progress variable models in high-order discontinuous Galerkin methods is that nonphysical pressure oscillations [130] can lead to elevated temperatures because temperature-induced dissociation is not included in flamelet mixing models. This is particularly important in ramjets where the injector/nozzle throats are near/at choked conditions , so the shear layer over the recirculation region is in the compressible regime. Spurious pressure oscillations can become large enough to alter the acoustic field in the ramjet. Thus, we develop below a formulation that explicitly includes the heat release and recasts it in a weak-form to discretize it over the discontinuous Galerkin finite element bases. Furthermore, we introduce a caloric equation of state with properties that depend on the flamelet tabulated temperature rather than the local thermodynamic one to linearize the equation of state.

Momentum and mass continuity are identical to the non-reactive case, which can be found (for example) in the work of Pierce and Moin [9]. The energy equation is discretized starting from a conservative formulation in terms of the sensible energy and enthalpy written under the assumption of thermally perfect gases [131],

$$e_{sk} \equiv \sum_{k=1}^{n_s} Y_k \int_0^T c_{v,k}\left(\tau\right) d\tau + \frac{1}{2}\,\mathrm{vec}_{\mathrm{n_t,N}}\, u \cdot \mathrm{vec}_{\mathrm{n_t,N}}\, u = e_s + e_k. \tag{4.1}$$

The thermal equation state for the mixture is written in terms of the mass fractions Y and the molar masses W using the ideal gas and Dalton laws

$$p = \rho RT \sum_{k=1}^{n_s} \frac{Y_k}{W_k}, \tag{4.2}$$

where $R = 8.3145$ J/mole $-$ K is the universal gas constant. The specific gas constant, $R_g \equiv R \sum_{k=1}^{n_s} \frac{Y_k}{W_k}$, is also introduced for future developments.

LES averaging of the energy equation yields

$$\frac{\partial \bar{\rho} e_{sk}}{\partial t} + \boldsymbol{\nabla} \cdot \left((\bar{\rho} e_{sk} + \bar{p}) \operatorname{vec}_{\mathrm{n_t,N}} u - \left(\bar{\lambda} + \lambda_t \right) \boldsymbol{\nabla} T + \bar{\rho} \sum_{k=1}^{n_s} Y_k V_k h_{s,k} \right) - \boldsymbol{\nabla} \cdot (\bar{\sigma} \cdot \operatorname{vec}_{\mathrm{n_t,N}} u) - \bar{\rho} \dot{\omega}_T = 0, \tag{4.3}$$

where the dissipative stress tensor has components $\bar{\sigma}_{ij} = 2\bar{\mu} S_{ij} + \tau_{ij}$, where $\overline{\overline{\boldsymbol{S}}} = 1/2 \left(\boldsymbol{\nabla} u + \boldsymbol{\nabla} u^T \right) - 1/3 \boldsymbol{\nabla} \cdot \operatorname{vec}_{\mathrm{n_t,N}} u \overline{\overline{\boldsymbol{I}}}$. The subgrid scale tensor is evaluated using an eddy viscosity approach

$$\overline{\overline{\boldsymbol{\tau}}} = 2\mu_t \overline{\overline{\boldsymbol{S}}} - 1/3 \bar{\rho} q_t^2 \overline{\overline{\boldsymbol{I}}}. \tag{4.4}$$

The parameters of the eddy viscosity model (μ_t and q_t) are evaluated using either Smagorinsky's or Wall Adapting Local Eddy-viscosity (WALE) approaches. All variables are Favre-averaged except for those marked with a bar overhead, to which Reynolds averaging is applied [132]. The heat release term in eq (4.3) is the product of the net volumetric production rates $\dot{\omega}_k$ and the heats of formation,

$$\dot{\omega}_T \equiv - \sum_{k=1}^{n_s} \dot{\omega}_k \Delta H_{fk}^0. \tag{4.5}$$

All variables dependent on the chemical state are evaluated using mixture rules where the chemical state is parameterized by scalars transported by the flow $\Psi_i,\ i = 1, \ldots, N_s$. They are the (Bilger) mixture fraction $\Psi_1 = Z$ [133], the progress variable $\Psi_2 = Y_{\mathrm{CO_2}}$, and the scalar dissipation $\Psi_3 = Z''$. More details on the choice of the progress variable Ψ_2 are provided below in Section 5. The variance is approximated by the LES scaling law $\bar{\rho} Z'' \approx C_V \bar{\rho} \boldsymbol{\nabla} Z \cdot \boldsymbol{\nabla} Z$, with $C_V = 0.5$ [134].

The differential equations for the evolution of the scalars are

$$\frac{\partial \bar{\rho}\Psi_i}{\partial t} + \boldsymbol{\nabla} \cdot (\bar{\rho}\, \mathrm{vec}_{\mathrm{n_t,N}}\, u\Psi_i) - \boldsymbol{\nabla} \cdot ((\bar{\rho} D_{\Psi_i} + D_t)\, \boldsymbol{\nabla}\Psi_i) - \bar{\rho}\dot{\omega}_i = 0, \tag{4.6}$$

where the turbulent mass diffusivity coefficients are approximated with a constant Schmidt number $\bar{\rho}D_t = \mu_t/Sc_t$, $Sc_t = 1$.

In the flamelet-progress variable approach, there are two sources of heating of the gas phase, which are expressed here as $\dot{\omega}_T = \dot{\omega}_P + \dot{\omega}_Z$. The first contribution is due to the progress and it is given here in terms of the net mass production rate of CO_2 ($\dot{\omega}_{CO_2}$) in the mixture,

$$\dot{\omega}_P = -\frac{RT_0}{\rho}\dot{\omega}_{CO_2} \sum_{k=1}^{n_s} \left(\frac{h_k}{RT_0} - 1 \right) \frac{\partial Y_k}{\partial \Psi_2} / \frac{\partial Y_{CO_2}}{\partial \Psi_2}. \tag{4.7}$$

The second contribution, the heat release due to a change in mixture fraction, is recast in terms of the second derivative of the scalars. Then, using integration by parts, we obtain the following source term for the volumetric residual of the DG weak form

$$\dot{\omega}_Z = -\sum_{i=1}^{N_s} (D_t + D_{\Psi_i}) \left\{ \sum_{k=1}^{n_s} RT_0 \left(\frac{h_k}{RT_0} - 1 \right) \frac{\partial^2 Y_k}{\partial {\Psi_i}^2} \right\} \nabla\Psi_i \cdot \nabla\Psi_i, \tag{4.8}$$

where Ψ_i are the scalars that parameterize the chemistry manifold and D are the diffusivities. The temperature dependency is added to this heat release term by imposing, at first-order, that it has the same sign as the difference between the flamelet temperature and the local thermodynamic temperature $T_{\mathrm{flamelet}} - T$. At higher-order, the dependency on the temperature can be tabulated in a secondary two-dimensional table spanned by the mixture fraction and the temperature deviation $T_{\mathrm{flamelet}} - T$.

A second issue with reactive high-order DG methods is that the convergence of the enthalpy to temperature polynomial inversion is typically slow when the temperature exceeds the bounds of validity of the mixture averaged polynomials. We have implemented a variable γ approach that allows researchers to perform flamelet computations in approximately the same computational time as the cold flow, leading to the possibility of analyzing acoustics in full-scale geometries. We define the specific heat ratio based on

the flamelet solution as,

$$\gamma\left(\Psi\right)=1+\frac{1}{R_g\left(\Psi\right)}\frac{e_{\text{flamelet}}\left(\Psi,T_{\text{flamelet}}\right)-e_0\left(\Psi\right)}{T_{\text{flamelet}}\left(\Psi\right)-T_0}; \tag{4.9}$$

Thus, we impose that the specific heats are functions of the composition and the flamelet temperature. This approach supports a linear variation of the sensible energy with the thermodynamic temperature,

$$e_s\approx\frac{T-T_0}{T_{\text{flamelet}}-T_0}\sum_{k=1}^{n_s}Y_k\int_{T_0}^{T_{\text{flamelet}}}c_{v,k}\left(\tau\right)d\tau=\left(\gamma-1\right)\left(\frac{p}{\rho}-R_gT_0\right). \tag{4.10}$$

We find that this approach yields fewer oscillations and is as accurate as one in which the specific heats are functions of the thermodynamic temperature.

Several test cases have been performed to validate the presented DG-flamelet approach. Simulations were performed using both the Smagorinsky and WALE sub-grid scale models. Both two-dimensional and three-dimensional cavity geometries were analyzed.

All equations were converted to the weak integral form before democratizing them on the FEM mesh. The scalar conservation equation, for example, eq (4.6) is written below

$$\begin{aligned}\int_\Omega w\left\{\frac{\partial\overline{\rho}\Psi_i}{\partial t}-\overline{\dot{\omega}}_b\right\}\,d\Omega+\int_\Gamma w\left[\overline{\rho}\vec{u}\Psi_i\right]\cdot\vec{n}\,d\Gamma-\int_\Omega\nabla w\cdot\left[\overline{\rho}\vec{u}\Psi_i\right]\,d\Omega\\-\int_\Gamma w\left[\left(\overline{\rho}D+\frac{\mu_t}{Sc_t}\right)\nabla\Psi_i\right]\cdot\vec{n}\,d\Gamma+\int_\Omega\nabla w\cdot\left[\left(\overline{\rho}D+\frac{\mu_t}{Sc_t}\right)\nabla\Psi_i\right]\,d\Omega=0,\end{aligned} \tag{4.11}$$

where Ω is the volume of a domain (element), Γ is its surface, w is a weighting function b is a general scalar, $\dot{\omega}_b$ is its source rate, D is the diffusivity of the scalar,μ_t is the eddy viscosity, and Sc_t is the turbulent Schmidt number. All terms in this equation are present for a progress variable since it is a non-conserved variable. However, as a conserved variable, mixture fraction has a source rate of zero.

Numerical model parameters, such as the viscosity μ and the thermal conductivity λ, are evaluated using mixture rules, so they are functions of the scalar variables. The mixture average transport, Wilke's formula [135], has been implemented. The thermal

conductivity is evaluated using the following average that considers combination of parallel and serial heat transfers through layers of gas particles [136]

$$\bar{\lambda} = \frac{1}{2}\left(\sum_{k=1}^{n_s} X_k \lambda_k + \frac{1}{\sum_k X_k/\lambda_k}\right). \tag{4.12}$$

Chapter 5

Flamelet Generated Manifolds

The flamelet model is integrated into the discontinuous Galerkin method by adding the additional progress variable and mixture fraction terms using a tabulation approach based on third-order B-spline base very similar to that used in the well known Sierra code [137]. Because it is not practical to solve a complete set of equations involving all species and reactions at every point within the domain, a single progress variable, C, is used to track the progress of the flame. In order to obtain a full range of flame values, the counterflow flame was simulated from adiabatic temperature to the extinction point by varying the distance, L, between the fuel and oxidizer inlets. As this distance was increased, the flame approached the adiabatic temperature, and the flame became extinguished due to strain when the inlets became too close together. C in accompaniment with the mixture fraction can be used as independent variables to describe all thermochemical properties, ψ, inside the steady, laminar diffusion flame such that $\psi = \psi(Z, C)$. Many values can be chosen as the progress variable with the main requirement being a monotonic function over all states of the flame from adiabatic to extinction points. As one can see in Figure 5.1, this work chooses the CO_2 mass fraction, Y_{CO_2}, at flame location because it satisfies the above condition.

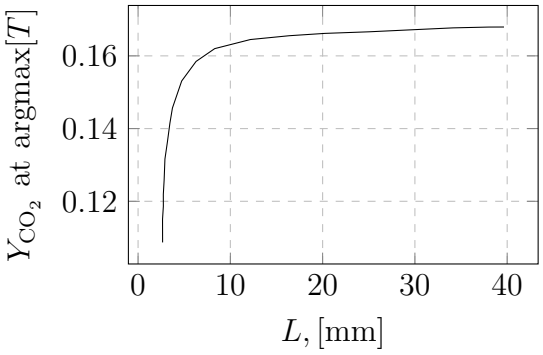


Figure 5.1: CO_2 mass fraction at maximum temperature vs distance between inlets, L.

In order to obtain a mapping of the unsteady, extinct values of the 1D flame, the open source code SpitFire [138] was used to evaluate the flamelet values from the extinction point all the way to a totally extinct solution using an unsteady time integration method. This is an approximate method of reproducing the unsteady S-curve branch of a flamelet solution that still accounts for a residence time of reacting species and ignition delay time. This incorporation of SpitFire to map the unsteady portion of the flame used the same chemical mechanism as previously used in Cantera as well as the flame state directly before extinction. This ensured a continuous function for the progress variable. The extinguished values accounted for approximately 60% of the total progress variable domain.

Once the progress variable was chosen and the tables extended to include extinction values, the temperature, progress variable dissipation, and remainder of the species could be mapped as a function of the mixture fraction, Z, and progress variable, C. C was scaled from $0-1$ using $C = \frac{C-min(C}{max(C)-min(C)}$ such that the independent variables of the library both spanned $0-1$.

In order to account for sub-grid fluctuations within the ramjet simulation, a probability distribution function was used inside the LES code. This was extrapolated from the flamelet libraries using SpitFire's library compilation functions. Clipped Gaussian and beta PDFs were explored; however, the distinction between the two was shown to be negligible inside the full ramjet simulations. Because Z and C are independent of one another, the PDF becomes $P(Z,C) = P(Z)P(C)$ which allows one to introduce the mean mixture fraction, $\bar{Z}$, and the mixture fraction variance, $\bar{Z}''^2$, such that the aver-

aged thermochemical properties, $\bar{\psi}$, are a function of $\bar{\psi}(\bar{Z}, C, \bar{Z}''^2)$. An example of a Clipped Gaussian distribution is shown in Figure 5.2 for the readers benefit, where the CO_2 generation was displayed as a function of the three independent variables. One can see from the figure that the majority of CO_2 production, and thus the rate of progress for the progress variable, occurs in the active flame region when the variance is low. The tracking of the progress variable and the equations detailing its diffusion are detailed in Chapter 4. Defining the progress variable as a summation of multiple species allows for a more broad and adaptable description of the flame states, and researchers are currently working on finding an appropriate composition and weighting for this progress variable definition [139].

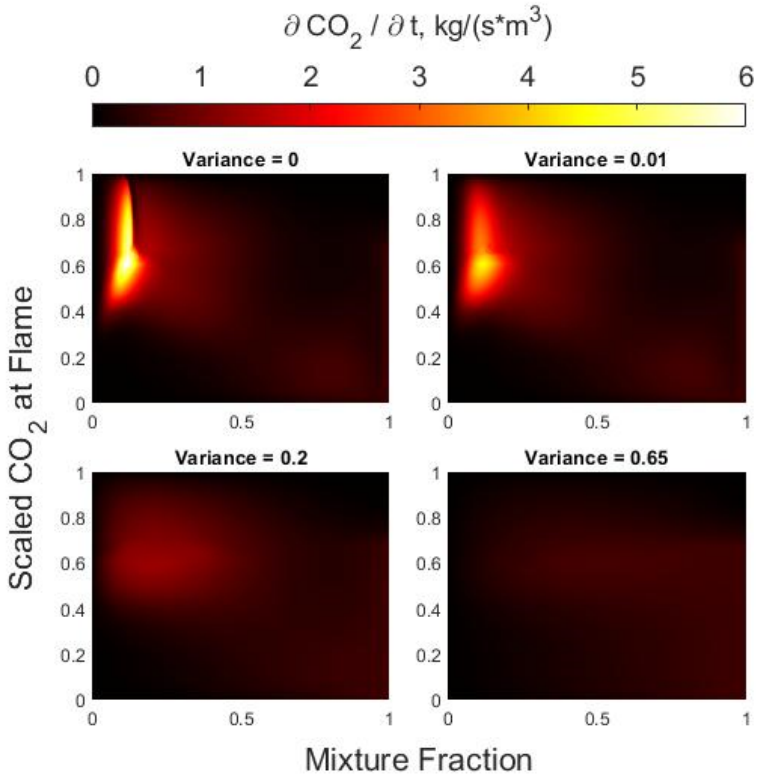


Figure 5.2: Turbulent library storage of CO2 net production

Researchers such as Nguyen et al. [140] suggest adding pressure as an additional independent variable; however, because the library is already 3 dimensions and adding additional independent variables exponentially increases the cost of searching through the library, a different, novel approach was taken. The probability density function

(PDF) underlying the Favre-averaged equations is defined per unit density, and the steady counterflow flame features an approximately linear variation of the mass rate of CO_2 production with the density. In order to improve upon this approximation, dependent variables were added to represent the CO_2 production under different pressure conditions. This permits creation of a polynomial as a function of pressure such that the libraries can be weighted and linearly interpolated without the cost of an additional dimension. This weighting takes the form of

$$(\tilde{\dot{\omega}}_{\mathrm{CO}_2})_P = \sum_{lib}^{NumLib} (Poly(P) * \tilde{\dot{\omega}}_{\mathrm{CO}_2}(\tilde{Z}, \tilde{C^*}, \tilde{Z''^2}))_{P_{lib}} \tag{5.1}$$

where $Poly(P)$ is a polynomial that is a function of pressure, lib denotes a library taken at a specific pressure, and the summation is done over all pressure dependent libraries.

5.1 Low Temperature Manifold

In order to aid in the search of the library, it is also beneficial for the library to be monotonic across all mixture fraction values. If this is not the case, higher-order search algorithms must be used to track both the location and slope of each point within the flamelet solution, which slows down the performance of the FGM model. Alternatively, a cost-function minimization approach can be adopted to define the progress as a linear combination of species [141], which leads to a difficulty in defining the diffusion coefficient in its convection-diffusion-reaction equation. Due to the characterization of the CO_2 manifold, the CO_2 mass fractions in individual flamelet solutions were found to follow a triangular pattern with $\max(Y_{\mathrm{CO}_2})$ occurring at the stoichiometric flame location as seen in Figure 5.3. The only non-monotonic location of the flame was found to be in the active flame, fuel-rich region (lines 8-10 with a mixture fraction greater than 0.6 in Figure 5.3). This non-monotonic nature was found to be a result of foam layer products and diffusion of species near the foam layer. Because of the importance of the fuel-rich region to the sustainability of combustion in the scramjet, a novel approach to the determination of the flamelet given the filtered LES solution was introduced.

An efficient search strategy for Discontinuous Galerkin's discretizations is based on the coefficient of determination of the manifold, which is rooted in the assumption that all nodes within an element belong to the same flamelet. The flamelet is identified by the progress value at the stoichiometric point P^*, where progress is defined as the mass fraction of tracked species $C = Y_{\mathrm{CO}_2}$ normalized by the magnitude of its range in the manifold. For all nodes within an element ($i \in \mathrm{Ele}$) the errors are evaluated as

$$e_i = \widetilde{C}_i(x, y, z, t) - \int_0^1 C_{fl}\left(Z, P^*\right) \widetilde{P}\left(Z; \widetilde{Z}_i, \widetilde{Z_i''^2}\right) dZ \ ,$$

the deviation from the mean is

$$v_i = \widetilde{C}_i - \sum_{j \in Ele} \widetilde{C}_j$$

and the progress is evaluated by maximizing the R^2 value:

$$P^* = \mathrm{argmax} \quad \left(1 - \frac{\sum_{j \in Ele} e_i^2}{\sum_{j \in \mathrm{Ele}} v_i^2}\right).$$

This simple approach is fast and accurate in a DG code because all nodes are not shared across elements thus there is no ambiguity in the definition of the elemental value of the progress. Moreover there is no sharing of nodal information across processors in a multi-processor implementation. A temperature profile across the three dimensions ($\bar{Z}, C, \bar{Z}''^2$) for the low temperature FGM can be found in Appendix A.

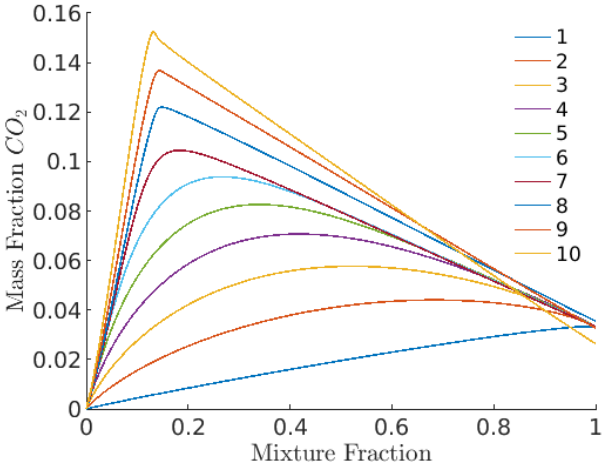


Figure 5.3: CO_2 mass fraction vs mixture fraction at multiple flame states with 1 being fully extinct and 10 being adiabatic

5.2 High Temperature Manifold

Due to the high stagnation temperatures required for flameholding in SFSJs, a high temperature manifold was also created with the air temperature approximately equal to the stagnation temperature in corresponding experimental trials [142, 143]. The high temperature manifold was created using the same methods as its low temperature counterpart which included all thermochemical properties being mapped to the mean mixture fraction $\bar{Z}$, mean variance of the mixture fraction $\bar{Z}''^2$, and the scaled flamelet progress P. The steady portion of the library was modeled by adjusting the dissipation in order to artificially strain the flame. The unsteady portion of the library used a time integration method to integrate the last steady flamelet solution to a purely mixing, non-reacting solution.

The air temperature in this manifold was 1200K which resulted in new obstacles to overcome such as more production of CO in the steady portion of the FGM domain. Due to the higher mass fraction of CO, the mass fraction of CO_2 was decreased in the steady portion of the library and that caused this region to become strongly non-monotonic. Fortunately, the library could still be searched in this region using the same method as detailed in Section 5.1 as a function of the progress variable, P, as seen in Figure 5.4.

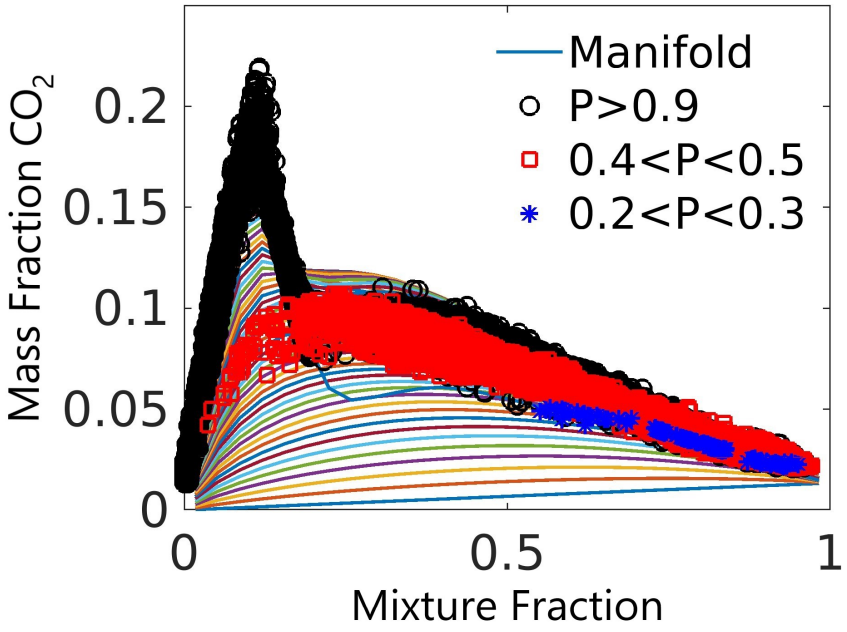


Figure 5.4: Flame states as a function of progress variable and mixture fraction with interpolation points

Figure 5.5 shows the production rate of CO_2 inside the high temperature manifold. The location of the maximum CO_2 production rate is in the fuel rich, unsteady portion of the library as opposed to near the stoichiometric location as one might expect. This is likely due to the amount of CO present in the steady portion of the library recombining with O_2 and becoming CO_2 in the unsteady portion of the library. This thus causes the production rate of CO_2 to appear large in this computational region.

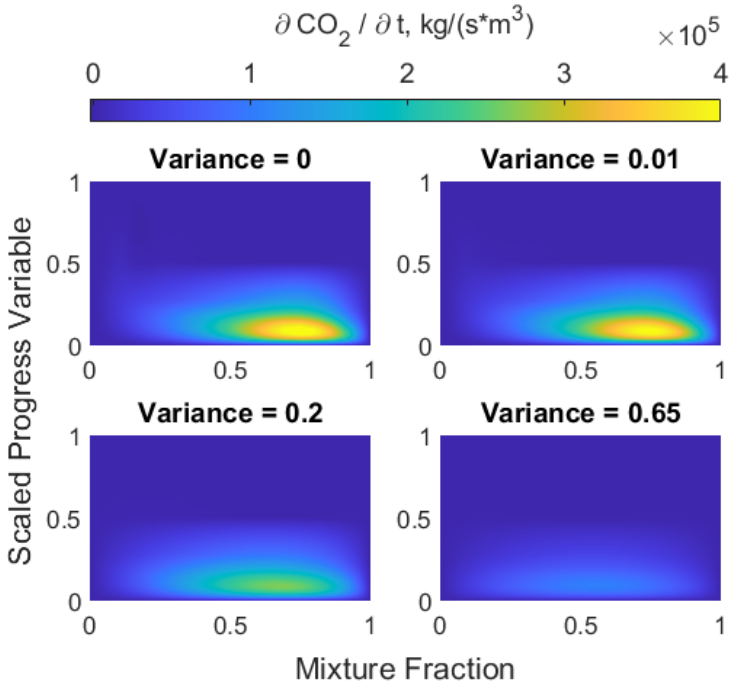


Figure 5.5: Turbulent library storage of CO_2 production rate with high (1200K) oxidizer temperature using extinction to model unstable burning branch

5.2.1 Ignition Manifold

Due to the nature of this high temperature manifold, it is also possible to model the unsteady portion of the library in a different manner - using ignition instead of extinction. The incoming air is now hot enough to cause autoignition when the dissipation is not too great. It was determined that an investigation into the effects of extinction vs ignition based libraries would be beneficial and give further insights into the applicability of FGMs.

The mapping and compilation of this ignition library was similar to that of the extinction library in that it used the same independent variables. A non-reacting mixture is unable to undergo autoignition if a large amount of dissipation is applied whereas a steady flame is able to withstand more dissipation without going extinct. For this reason the steady portion of the library was also the same, but slightly smaller in the ignition base FGM. In order to obtain the unsteady portion of the manifold, a maximum dissipation was found that would still allow autoignition. The unsteady branch of the FGM was filled by performing a time integration using this maximum allowable dissipation. The steady portion of the domain would then begin with this dissipation and slowly decrease

it until an adiabatic solution was reached.

Figure 5.6 shows the CO_2 production rate in this ignition based library. The location of the maximum CO_2 production now appears near the stoichiometric location and P$\approx$ 0.5. The maximum production rate is now much smaller than its extinction counterpart and does not seem to support much production in the fuel rich, unsteady region of the FGM.

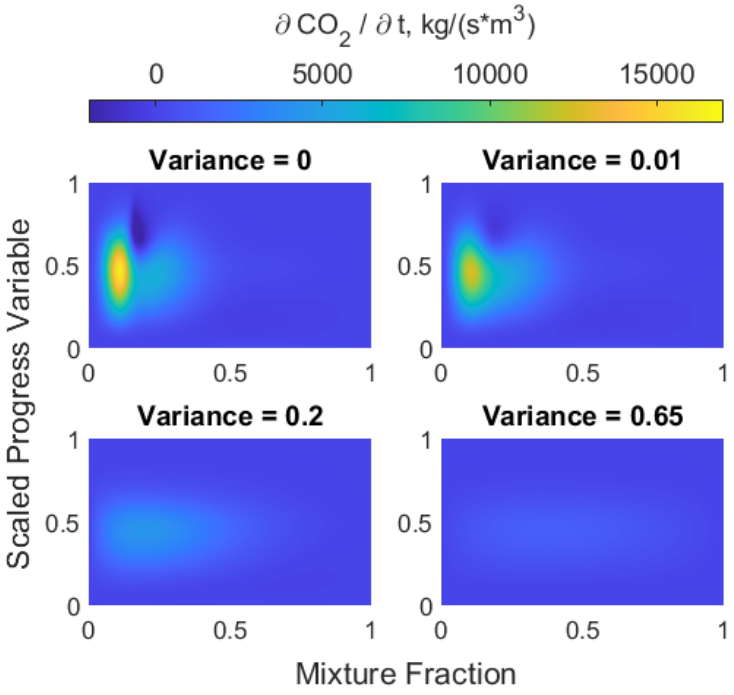


Figure 5.6: Turbulent library storage of CO_2 production rate with high (1200K) oxidizer temperature using ignition to model unstable burning branch

5.3 Summary

In conclusion, three flamelet generated manifolds were created to model combustion phenomenon under various conditions. Two oxidizer temperatures were modeled in order to match the stagnation temperatures of experimental groups [142, 143]. In the lower temperature library, the unsteady portion of the flamelet S-curve was modeled using extinction and a time integration approach. The high temperature conditions gave rise to two manifolds. One used extinction and the other used ignition to model the unsteady portion of the FGMs. This was done in the high temperature manifold due to autoignition being easier to achieve under these oxidizer conditions. All FGMs stored all averaged thermochemical properties, $\bar{\psi}$, as a function of $\bar{\psi}(\bar{Z}, C, \bar{Z}''^2)$ and used a novel

polynomial curve fit to introduce compressibility effects into the FGMs without increasing the manifold dimensions and thus the computational cost.

Due to the nature of a thermally decomposing melt layer, none of the libraries were monotonic throughout. While monotonicity is only required at the stoichiometric location in order to properly define the FGMs, looking up values from the FGMs is much easier if its entirety is monotonic. In order to overcome this obstacle, a cost minimization function was used to determine with flamelet progress branch a given element should lie on. This in combination with the pressure contribution via polynomial curve fitting and creation of both extinction and ignition based manifolds help provide new insights and methods to the FGM research community.

Chapter 6

Comparisons of Finite Rate Chemistry and Flamelet Generated Manifold Solutions

In order to create future improvements on libraries such as the ones presented in this work, more comprehensive tests must be performed to investigate when the library fails to model the flamelet physics. In order to do this, one needs a more rigorous testing criteria and data analysis method than those provided by full combustor experimental comparison. To better understand properties like reaction rates and diffusion of species, finite rate chemistry (FRC) simulations were performed using PeleC [144, 145]. These FRC simulations used the same chemical mechanism employed by the flamelet generated manifold and investigated several simplified geometries in order obtain comparison from multiple types of mixing and combustion.

Because of the strong coupling between fuel injection rate and chemical heat release from the flame, the fuel injection was decoupled and set as a constant value for these studies. This reduced the number of factors involved in the comparison and helped to focus on just the FGM's modeling capabilities. The goal of this is to identify regions of the manifold that do not properly model the physics and improve these portions to provide more reliable flamelet-progress variable models. Two cases were considered: combustion inside a deep cavity and combustion within a boundary layer over a flat plate.

6.1 Deep Cavity Case

One geometry utilized a deep cavity with a similar aspect ratio to that of the undeformed Fuel Grain 14 scramjet geometry studied in [143]. This geometry with labeled boundary conditions can been seen in Figure 6.1. The inlet on the left of the domain injected air ($Y_{O_2} = 0.23, Y_{N_2} = 0.77$) at a constant temperature, pressure, and Mach number of 900K, 3atm, and 2, respectively. The outlet on the right utilized a first-order extrapolation to impose a supersonic outlet. Fuel ($C_4O_2H_6$) was injected in line with the air inlet at a temperature of 700K and injection rate of 84 $kg/(m^2 * s)$. Walls were modeled with no slip and at a constant temperature of 1000K. The free-stream boundary forced flow to travel in-line with the inlet with the same properties (pressure, temperature, Mach number, etc.) as the incoming air. The entire domain height and length were 1.35 and 3.6 centimeters, respectively.

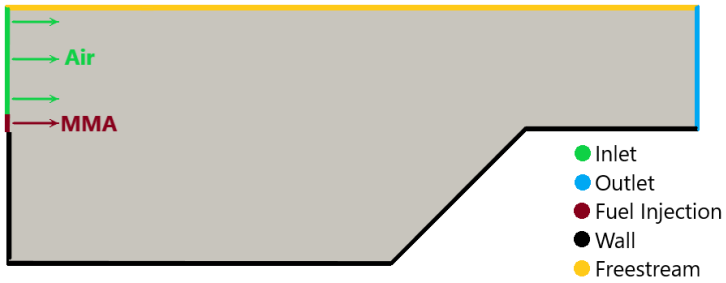
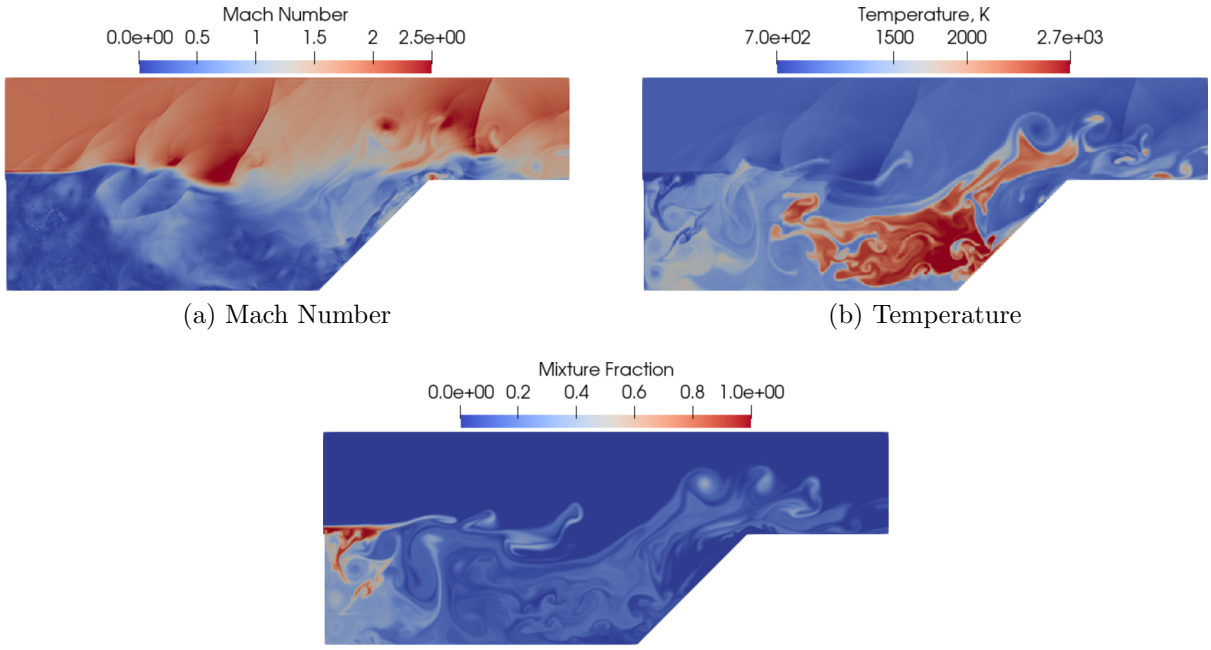


Figure 6.1: Deep cavity FRC geometry

In this configuration, the mixture experienced autoignition toward the rear of the cavity as predicted by the finite rate model. Shortly after this occurred, the finite rate chemistry solution was interpolated into the flamelet-progress variable approach independent variables. The mixture fraction was found by applying Bilger's mixture fraction, and the flame progress was determined using this mixture fraction, the mass fraction of CO_2, and the tabulated CO_2 mass fraction inside a given FGM. The finite rate chemistry code did not possess sub-grid scale mixing models and thus the variance of the mixture fraction was taken as zero. The state of the Mach number, temperature, and mixture fraction at which point this interpolation was made can be seen in Figure 6.2. One can see the Mach 2 incoming air and the low Mach number cavity flow supporting the mixing

of fuel and air. The mixture fraction within the cavity is relatively dispersed and tends to exist between $0.1 < Z < 0.6$ with the more fuel rich regions existing near the front of the cavity. As previously mentioned, autoignition occurred in the back half of the cavity with the flame reaching approximately 2700 K.



(a) Mach Number

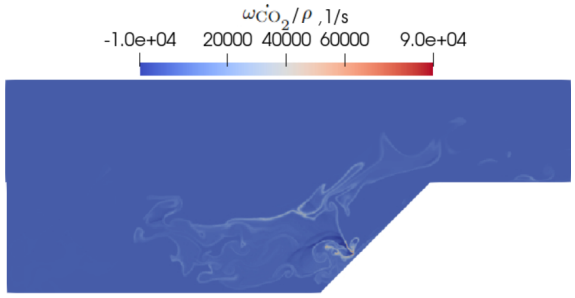
(b) Temperature

(c) Mixture Fraction

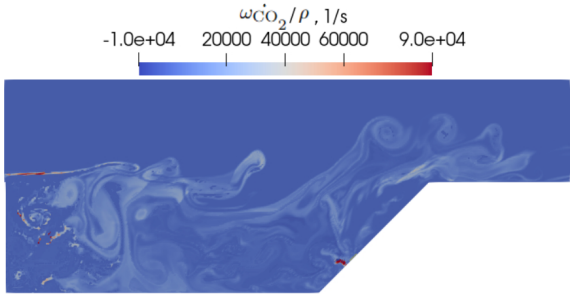
Figure 6.2: Instantaneous FRC solution shortly after autoignition for geometry with deep cavity

6.1.1 Visual Comparison of FRC and FGM Simulations

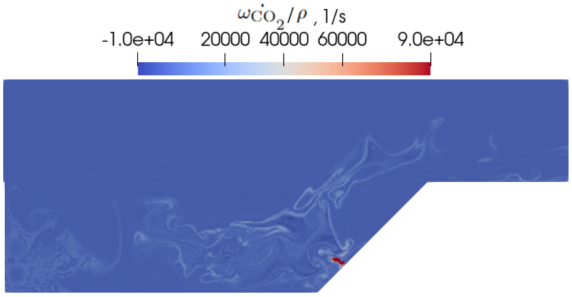
After the FRC solution had been interpolated into the FGM's independent variables, the simulations were run simultaneously and without communication. Two FGMs were investigated - the 1200K extinction manifold and the 1200K ignition manifold detailed in Chapter 5. Figure 6.3 displays the CO_2 production per unit mass, $\frac{\dot{\omega}_{CO_2}}{\rho}$ using FRC, the extinction FGM, and the ignition FGM at the point of initialization. As one can see, the extinction FGM in Figure 6.3b seems to produce CO_2 throughout the cavity far more evenly than the FRC and ignition FGM solutions in Figures 6.3a and 6.3c. While the flame front is more obvious in these latter figures, the extinction FGM models a more dispersed progress rate of the flame in regions that should not be igniting including the supersonic shear flow where fuel and air first meet.



(a) Finite rate chemistry solution



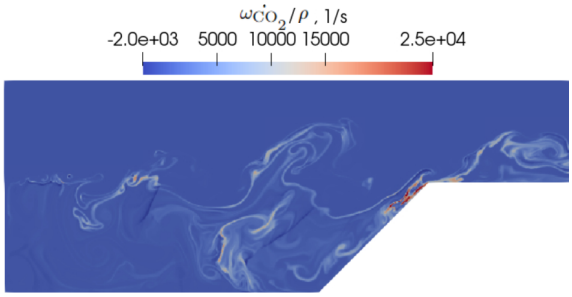
(b) Extinction FGM solution



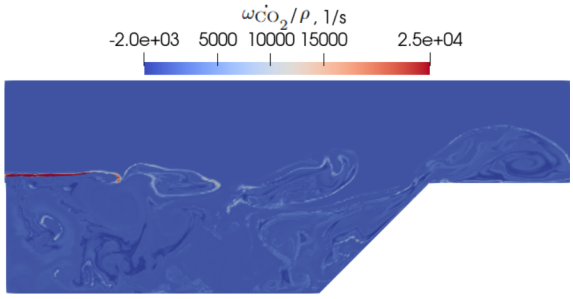
(c) Ignition FGM solution

Figure 6.3: Comparison of instantaneous production of CO_2 between two FGMs and finite rate chemistry in deep cavity

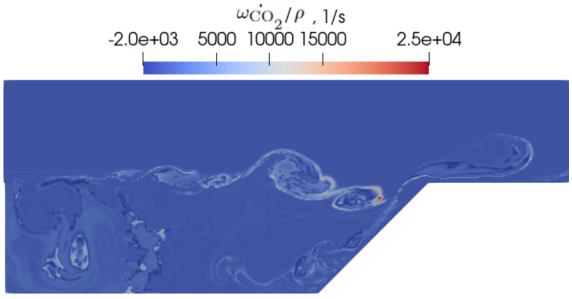
The CO_2 production can once again be seen in Figure 6.4 after each simulation has independently progressed for 2.5e-4 seconds. One can see that the flame front has become much more obvious in the extinction FGM in Figure 6.4b; however, it still models far too much CO_2 production in the initial fuel and air shear layer over the beginning of the cavity. The ignition FGM in Figure 6.4c does slightly better and seems to appropriately model ignition delay as the fuel mixes in the second half of the cavity. The magnitude of CO_2 production in both libraries matches those of FRC in all regions except the extinction FGM when the fuel is initially being injected and mixing in the shear layer.



(a) Finite rate chemistry solution



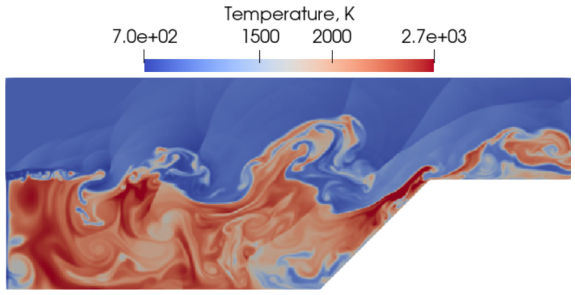
(b) Extinction FGM solution



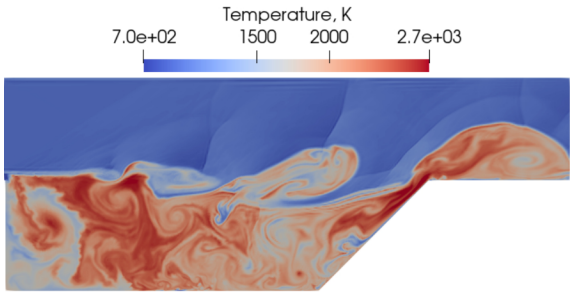
(c) Ignition FGM solution

Figure 6.4: Comparison of instantaneous production of CO_2 between two FGMs and finite rate chemistry in deep cavity after 2.5e-4 seconds of independent running

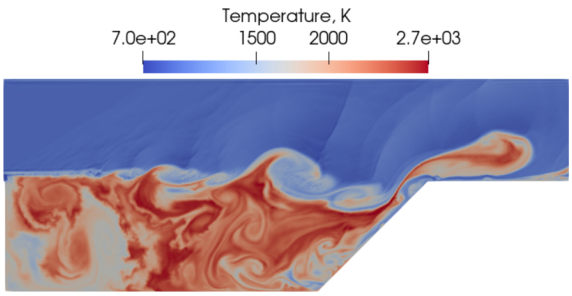
Temperature profiles at this time for each simulation can also be seen in Figure 6.5. Despite initial differences in CO_2 production and the decomposition in the supersonic shear layer, both FGM temperature solutions are very similar to one another. Their maximum temperatures and profiles and closely resemble the FRC solution with the only exception occurring in the front of the cavity. The discrepancy in this region of the cavity could be due to several causes, but the most likely involve species transport. As previously mentioned, sub-grid scale mixing models were employed in the flamelet-progress variable simulations, but these were not present in the finite rate chemistry analysis. Diffusion in the flamelet-progress variable approach only deals with a single variable as opposed to the multi-species diffusion that occurs in the FRC analysis. This difference in mixing rates leads to the discrepancy seen in Figure 6.5, but does not last long as the high temperature flames reach the front of the cavity using the FGM models later in time.



(a) Finite rate chemistry solution



(b) Extinction FGM solution



(c) Ignition FGM solution

Figure 6.5: Comparison of instantaneous temperature between two FGMs and finite rate chemistry in deep cavity after 2.5e-4 seconds of independent running

Additional figures comparing the CO_2 mass fraction and heat release in FRC and flamelet-progress variable models can be found in Appendix A in Figures A.2 and A.3. Both of these demonstrate the FGMs' abilities to properly model the magnitude of scalars, but their location can be erroneous in this unsteady flow due to varying transport properties in the FRC and PV approach. This is especially evident in the CO_2 mass fraction figure where Y_{CO_2} is much more dispersed than in the FRC solution.

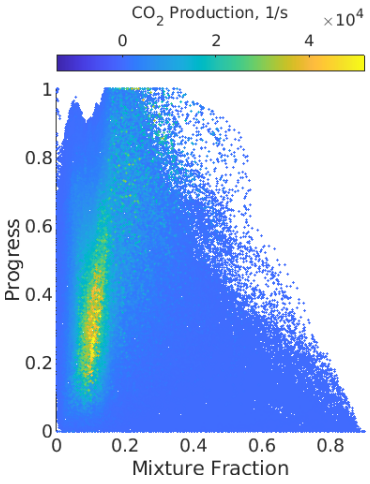
6.1.2 Graphical Comparison

In order to gain a better understanding of how the different FGMs behave in comparison to a FRC solution, graphical analysis is used in Figure 6.6. The production of CO_2 is what drives the FGM flame progress, thus the accurate modeling of this dependent variable is paramount. The FRC solution for CO_2 production can be seen in Figure 6.6a. If one was to continuously interpolate the FRC solution onto the FGMs' CO_2 production for the extinction and ignition FGM, one would produce Figures 6.6b and 6.6d. Figures 6.6c and 6.6e show the CO_2 production when the flamelet-progress variable approach is run without information of the FRC solution, and thus both their CO_2 production and

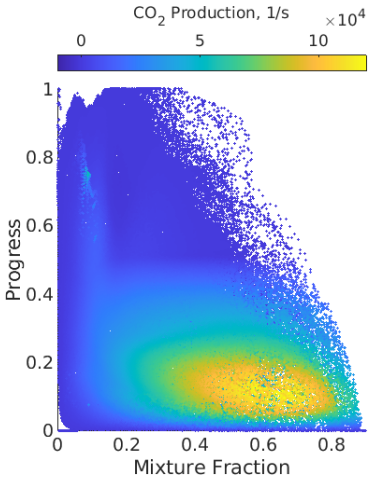
location of data points can vary from the FRC data.

In the extinction FGM solution shown in Figures 6.6b and 6.6c, it becomes obvious why a large amount of CO_2 was being produced in the supersonic shear region over the front half of the cavity. In comparison to the FRC data, there is far too much CO_2 production in the unsteady, fuel rich portion of the library. As the extinction library progresses the states of the flame, the point distribution shifts dramatically from the FRC shape. Fortunately, this shift in shape helps correct itself as there are no longer as many points in the region with too great CO_2 production. This is why the initialization of the extinction FGM looks much worse in 6.3b than later in time in Figure 6.4b where the only major issue exists in the supersonic shear layer region. The few scattered remaining points in Figure 6.6c in the fuel rich, unsteady portion of the manifold originate from this shear region of the simulation.

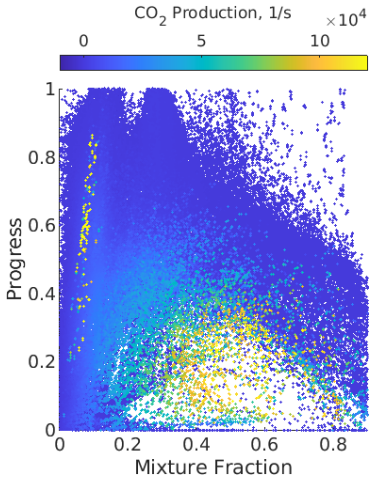
The ignition library results in Figures 6.6d and 6.6e show much better agreement with FRC results. The maximum production of CO_2 exists in approximately the same location as the FRC plot in Figure 6.6a, and even when left to run independently (6.6e), the ignition FGM produces a point distribution within the domain that is relatively the same as its FRC counterpart.



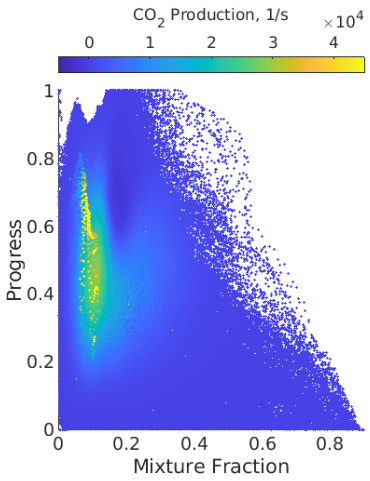
(a) Finite rate chemistry solution



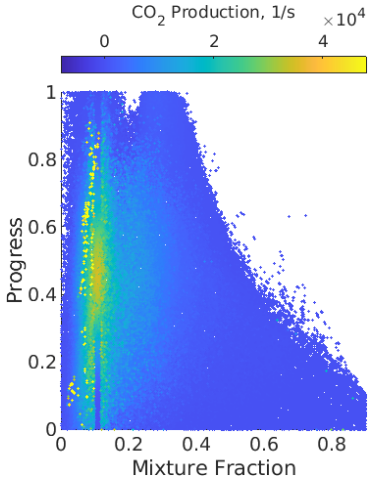
(b) Interpolation of FRC solution onto extinction FGM



(c) Extinction FGM solution



(d) Interpolation of FRC solution onto ignition FGM



(e) Ignition FGM solution

Figure 6.6: Comparison of CO_2 production as a function of mixture fraction and flame progress

6.2 Unstable Boundary Layer Flame Case

In order to observe the convective burning of MMA, a flat plate with fuel injection was also simulated. Due to the reduced mixing and recirculation in this domain, better observations can be made in regard to the ignition delay of MMA and combustion in high-shear flows. While this flow is far less stable than the previous cavity case discussed in Section 6.1, a better understanding of blow off is hoped to be gained which will aid in the creation of libraries that can accurately predict this phenomenon. The domain under investigation can be seen in Figure 6.7 where the height and length of the domain are 1.5 and 16 centimeters, respectively. The inlet boundary condition on the left of the domain imposed a self similar boundary profile with a Reynold's number of 2000 and the species composition was composed of pure air ($Y_{O_2} = 0.23, Y_{N_2} = 0.77$). The freestream temperature, pressure, and Mach number were 1000K, 3 atm, and 2, respectively. The outlet on the right used a first order extrapolation in order to maintain a supersonic exit plane. Fuel ($C_4O_2H_6$) was injected along the first 3 cm of the bottom surface of the domain at 700K and 84 $kg/(m^2 * s)$. Walls were modeled with no-slip and at 1000K. The freestream boundary condition imposed the same values as that of the far field inlet conditions.

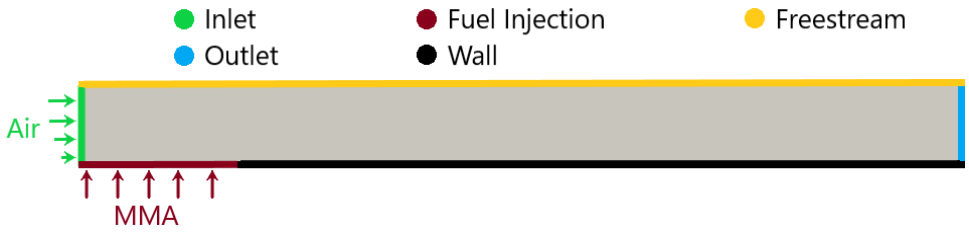
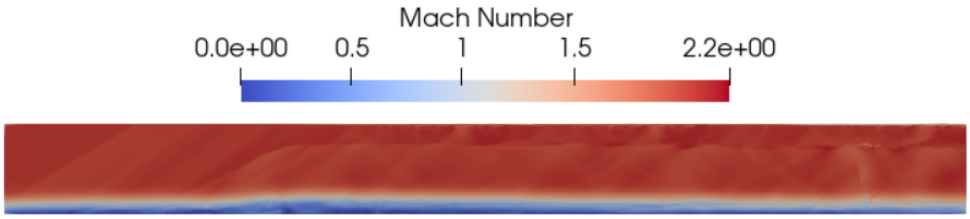


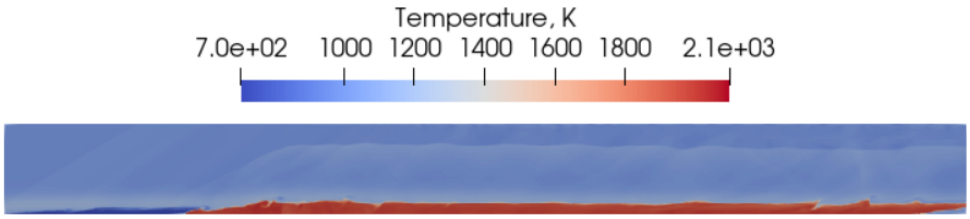
Figure 6.7: Flat plate with boundary layer geometry

Despite the imposed boundary layer profile at the inlet and high temperatures of the freestream, the dissipation was too great in this simulation to cause autoignition. Because of this, once the flow had run to a semi-steady state, a high temperature (2000K) region was added to the fuel in the region of $3 < x < 15$ and $y < 0.2$ centimeters. The flow field after this high temperature region was added can be seen in Figure 6.8. The Mach 2 incoming air and boundary layer profile can easily been seen with the fuel and air mixing

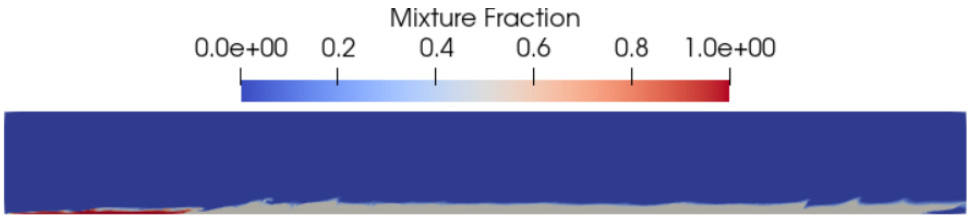
near the middle depth of the boundary layer. The mixture fraction and flame progress variables were found using the same process as described in Section 6.1. The flamelet-progress variable approach was once again implemented using both the extinction and the ignition FGMs and used these initial interpolated values as a starting point.



(a) Mach Number



(b) Temperature



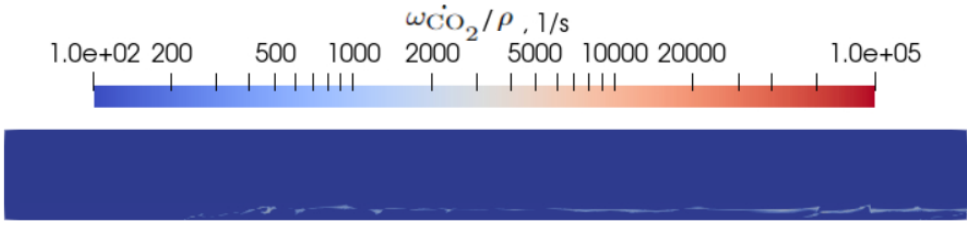
(c) Mixture Fraction

Figure 6.8: Instantaneous FRC solution shortly after autoignition for geometry with boundary layer blowoff

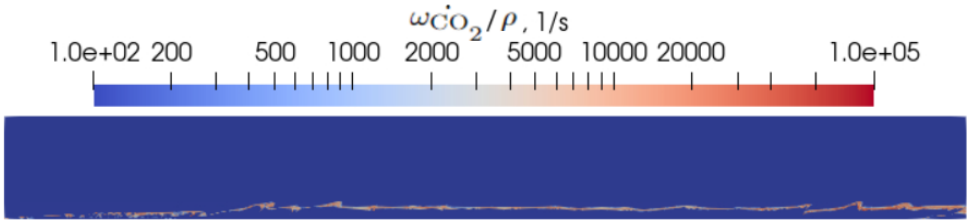
6.2.1 Visual Comparison

Once again, after the FRC solution had been interpolated to the FGMs' independent variable, all three combustion models were run simultaneously and independently of one another. The initial production of CO_2 normalized by the density, $\frac{\dot{\omega}_{CO_2}}{\rho}$, can be seen in Figure 6.9. One can clearly see the flame front using all three models; however, the ignition FGM in Figure 6.9c does much better than the extinction FGM in Figure 6.9b at modeling the magnitude and ignition delay of the flame. While the ignition FGM only has CO_2 production near the high temperature region similar to that shown in the FRC solution, the extinction FGM also shows CO_2 production further upstream near the initial

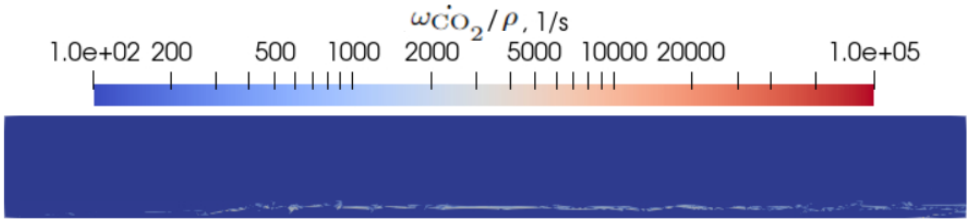
fuel injection region. This, in addition to the over prediction of CO_2 production in the extinction FGM, makes the ignition FGM appear much more favorable when modeling these early time steps.



(a) Finite rate chemistry solution



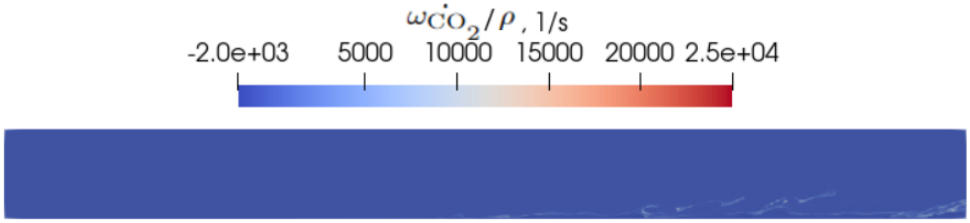
(b) Extinction FGM solution



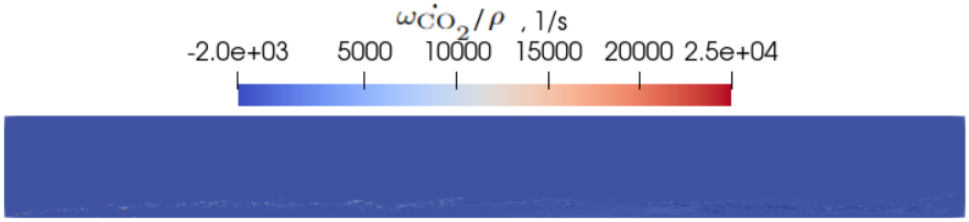
(c) Ignition FGM solution

Figure 6.9: Comparison of instantaneous production of CO_2 between two FGMs and finite rate chemistry in boundary layer blowoff

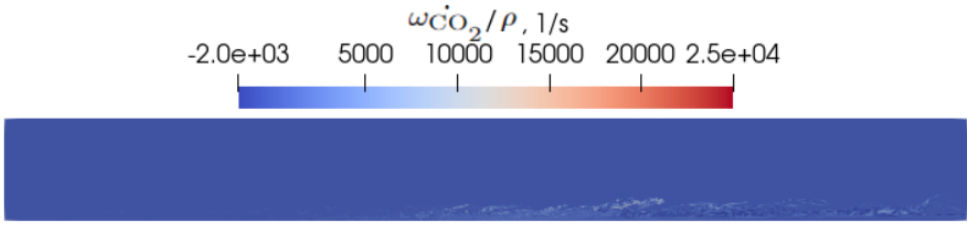
After running independently of one another for 2.5e-4 seconds, the CO_2 production from each model are once again compared in Figure 6.10. One can see in the FRC and ignition manifold solutions that the flame front has been pushed downstream. Unfortunately, the extinction FGM does not show this and instead allows the flame to anchor and begin ignition at nearly the beginning of the domain. This clearly demonstrate far too much flame progress in regions that should not be progressing. The ignition FGM shows CO_2 production slightly further upstream than it should, but the difference in the amount of mixing between FRC and flamelet-progress variable approaches makes it unclear if this discrepancy is due to transport or reaction properties.



(a) Finite rate chemistry solution



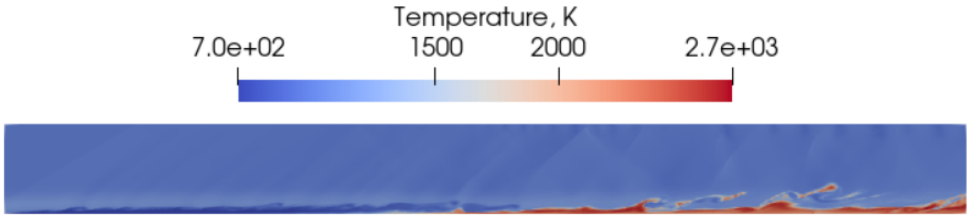
(b) Extinction FGM solution



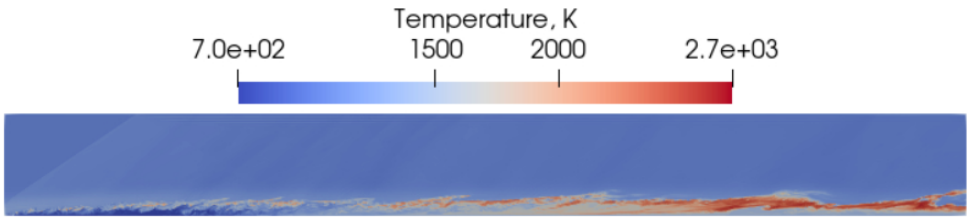
(c) Ignition FGM solution

Figure 6.10: Comparison of instantaneous production of CO_2 between two FGMs and finite rate chemistry in boundary layer blowoff after 2.5e-4 seconds of independent running

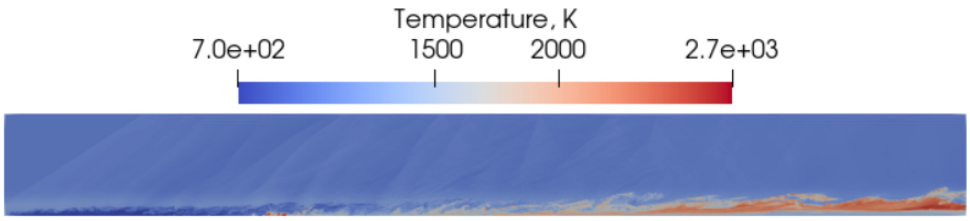
The temperature profiles 2.5e-4 seconds after forced ignition can be viewed in Figure 6.11. The consequences of over-prediction of CO_2 production in the extinction library can easily be seen in Figure 6.11b. The decomposition of fuel in the early portion of the domain leads to a flame anchoring in the upstream mixing region. This is not the case in the FRC and ignition FGM solutions shown in 6.11a and 6.11c, respectively. Both of these solutions show the flame being pushed to the back of the domain. The only major difference between these two figures is the uniformity of the high temperature region. This is likely due to transport properties of the fluid as more turbulent mixing structures can be seen in the FGM solution when compared to the FRC temperature profile. Despite this difference in uniformity, the location of the flame downstream appears approximately the same in the ignition FGM and FRC solutions.



(a) Finite rate chemistry solution



(b) Extinction FGM solution



(c) Ignition FGM solution

Figure 6.11: Comparison of instantaneous temperature between two FGMs and finite rate chemistry in boundary layer blowoff after 2.5e-4 seconds of independent running

Additional figures comparing the CO_2 mass fraction and heat release in FRC and flamelet-progress variable models can be found in Appendix A in Figures A.5 and A.4. Both of these demonstrate the FGMs' abilities to properly model the magnitude of scalars, but their location can be erroneous in this unsteady flow due to varying transport properties in the FRC and PV approach. This is especially evident in the CO_2 mass fraction figure where Y_{CO_2} is much more dispersed than in the FRC solution.

6.2.2 Graphical Comparison

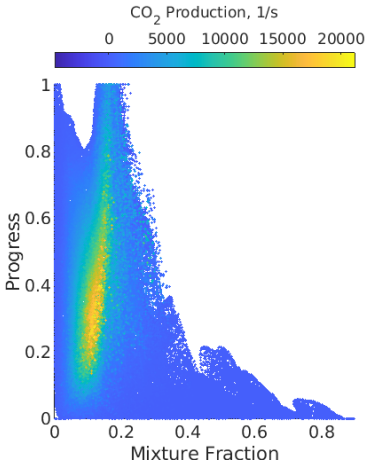
In order to graphically compare how the FGMs perform in comparison to the FRC solution, all solutions were once again mapped to the FGM's independent variables. Once mapped to these variables, each element within the domain can be plotted with respect to its corresponding flame progress and mean mixture fraction. Figure 6.12 shows such a plotting where the coloring is determined by the production rate of CO_2 normalized by the density. Because the flame progress changes based on this production rate, errors

in CO_2 production can influence the final point distribution of these figures. This is evident in Figures 6.12c and 6.12e where the FGMs had run independently for long enough to influence the point distribution. Figures 6.12b and 6.12d take the FRC solution for mixture fraction and flame progress and plot the interpolated FGM production of CO_2 on these points similarly to how Figure 6.9 was created, but this time the interpolation was done at a later solution in time.

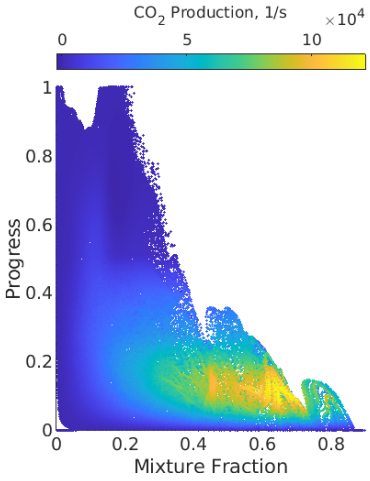
Figures 6.12b and 6.12c show the interpolated extinction FGM solution and the extinction FGM solution after running on its own for 2.5e-4 seconds. When comparing these to the FRC solution in Figure 6.12a, it is clear to see the over-prediction of CO_2 production in the extinction FGM model. As this model ran independently, it created a large region in the FGM without points. Any elements that exist in this region of $0.1 < Z < 0.7$ and progress< 0.3 quickly leave the region due to the CO_2 production therein. As one can see in Figure 6.12c this greatly affects the point distribution within the plotted domain, but it also prevents elements from continuously producing an excess of CO_2. In the long term, this shift in points likely aids in the flamelet modeling and reduces reactivity in the extinction FGM which is certainly necessary with the CO_2 production is so high therein.

Figures 6.12d and 6.12e display the interpolated ignition FGM solution and the ignition FGM solution after running on its own for 2.5e-4 seconds. Fortunately, these do not suffer from the same errors as their extinction FGM counterparts. The primary location for CO_2 production is near the stoichiometric location at $Z \approx 0.12$ and spread throughout the flame progress domain. The only difference seems to be that the FRC CO_2 production shifts toward $Z \approx 0.2$ as the flame progress increases whereas the FGM CO_2 production remains relatively centered about $Z \approx 0.12$. The final point distribution in Figure 6.12e also looks much better than its extinction manifold counterpart. While it it not an exact replica of the FRC point distribution, it does a good job at capturing the general shape. In fact, the only major difference is a stretching of points along the mixture fraction axis which is likely a byproduct of either the aforementioned mixing model or diffusion modeling differences between the FRC and flamelet-progress variable

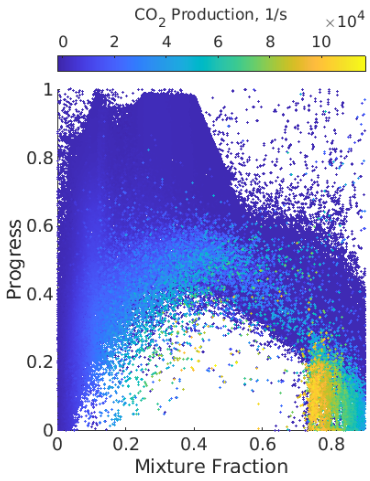
simulations.



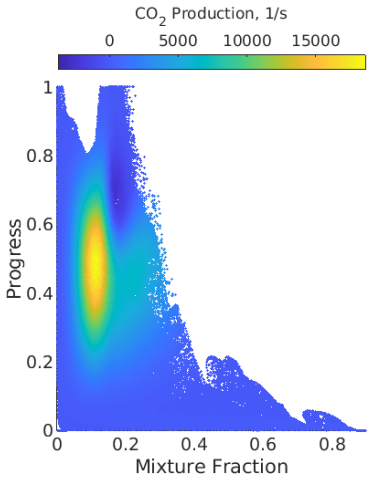
(a) Finite rate chemistry solution



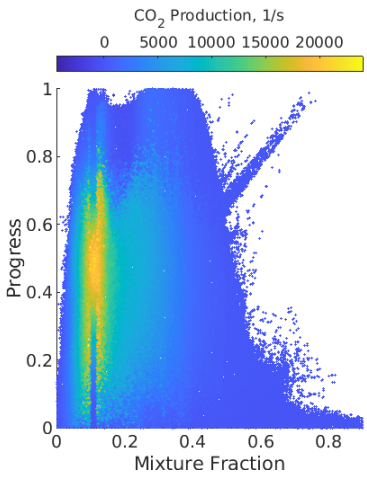
(b) Interpolation of FRC solution onto extinction FGM



(c) Extinction FGM solution



(d) Interpolation of FRC solution onto ignition FGM



(e) Ignition FGM solution

Figure 6.12: Comparison of CO_2 production as a function of mixture fraction and flame progress

6.3 Conclusions

In conclusion, an extinction and ignition FGM were compared against finite rate chemistry data using instantaneous solutions of CO_2 production and temperature as well as element distribution within the FGM domain for two different flow cases. During the ignition phenomenon - both artificial and autoignition - the ignition FGM out-performed the extinction manifold due to the extinction FGM producing far too much CO_2 in the unsteady portion of the library. After running independently for some time, both the extinction and ignition manifolds produced similar results in the deep cavity burning geometry. While species transport properties seem to be different from the FRC solution, both the FGM solutions model CO_2 production and temperature distribution well within the cavity. Unfortunately, this is not the case in the unstable boundary layer simulations. While the ignition library does a good job at modeling the progress rate of the flame, the extinction library fails to properly model ignition delay time in the upstream cold regions of the domain. Beyond this, the only notable differences occur from the different mixing rates of species. Because of this, it is determined that both extinction and ignition libraries do well at modeling quasi-steady flames within cavities, but the ignition library possesses significant advantages when simulating either strained flames or ignition phenomenon.

Chapter 7

(sc)Ramjet Simulations

The team at Virginia Tech copmrised faculty and graduate students, some with main emphasis on experiments and others focusing on simulations. Validations of the fluid domain with the FGM model integration were first made using a ramjet geometry and experimental work where simulations were able to properly predict fuel regression rates and acoustic coupling with the appropriate modes within the combustor. These results are fully documented in [11, 12]. Similar studies were then conducted for a scramjet setup. Several fuel grain geometries have been investigated including box grain geometries where top, bottom, and side walls were comprised of solid fuel [142] and optically accessible wide geometries which possessed a higher aspect ratio and quartz side walls to allow for better experimental observation [143].

7.1 Experimental Procedures and Geometry

7.1.1 Ramjet Setup

The ramjet geometry [11, 12] with all relevant axi-symmetric dimensions can be seen in Figure 7.1. High pressure air at 0.47 MPa and 548K stagnation pressure and temperature was fed into the inlet chamber, through an isolator, and into a ramjet combustion cavity where it mixed with gaseous MMA and combusted. The air/fuel mixture then traveled downstream to a mixing chamber where the mixture was given more time to fully react before exiting via a throat and nozzle configuration. Two cavity lengths, L_{cavity}, were

numerically evaluated. These lengths were 152 mm and 51 mm. The cavity diameter, d_{cavity}, and port diameter, d_p, remained constant as 44mm and 38mm, respectively.

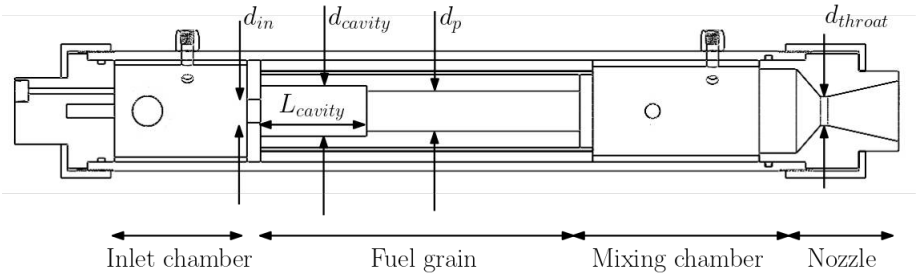


Figure 7.1: Experimental diagram of ramjet combustor sections and relevant dimensions [11, 12]

7.1.2 Scramjet Setup

The general scramjet combustor geometry under investigation can be seen in Figure 7.2 where the experimental group [142, 143] utilized an upstream Mach 2 nozzle and preheated air. The heated air feeds into a combustion chamber, through a diffuser, and out an expanding section. Seven pressure ports were used along the top surface of the fuel grain in order to obtain pressure data along the center line of this surface. Three scramjet configurations were investigated with their primary dimensions reported in Table 7.1 where the depth is the dimension into the page of Figure 7.2. Of the three cases shown, Fuel Grain 11 (FG11) varies significantly from Fuel Grains 14 and 17 (FG14 and FG25) due to the air inlet conditions and fuel wall configuration.

FG11 utilized a box geometry where all walls downstream of the converging/diverging inlet were composed of PMMA solid fuel including the side walls into and out of the page which were flat and did not change with respect to the stream-wise direction. FG11 tests also did not heat the air to the same degree in the upstream pressure chamber. Thus, the stagnation temperature of the incoming air into the combustor was 873K. Because this temperature was below the auto-ignition temperature of MMA, ignition had to be aided using small strips of solid propellant that were applied to the top and bottom regions of the cavity using an adhesive that was expected to be consumed in the early stages of combustion.

In contrast, FG14 and FG25 only used solid fuel on the top and bottom surfaces of

the combustor, and the side walls were replaced with quartz windows in order to allow for optical access. Via the use of an upstream propane torch, the stagnation temperature of the incoming air reached 1223K. Whether a given geometry used a box fuel grain and the stagnation temperature of the incoming can also be seen in Table 7.1.

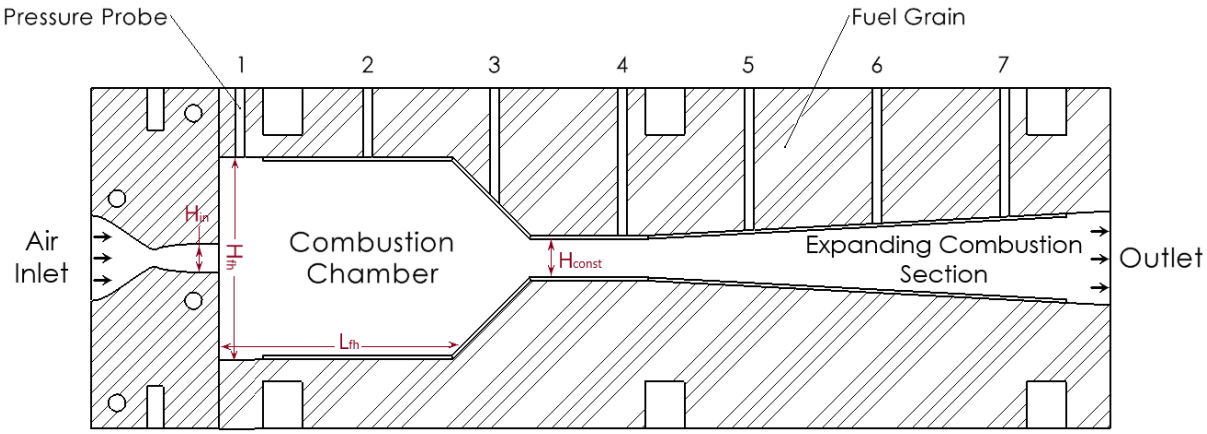


Figure 7.2: Scramjet test section schematic with labeled probe locations

Table 7.1: Experimental Combustor Specifications

	FG11	FG14	FG25
Depth, mm	25.4	50.8	50.8
H_{fh}, mm	60	50	50
L_{fh}, mm	70	70	55
H_{in}, mm	8.8	4.4	4.4
H_{const}, mm	13.5	6.6	6.6
Box Geometry	Yes	No	No
Inlet Air Temperature, K	873K	1223K	1223K

7.2 Non-Reacting Scramjet Case

In order to validate the DG solver in non-reacting flow and better understand the recirculation zones within the scramjet cavities, a cold flow analysis with both RANS and LES was performed with total air temperature equal to 300 K to investigate how the modes supported by the cavity change with the geometry and affect transport in the cavity.

Before discussing the modes, the mean conditions were considered and compared to the experimental measurements. The focus of this analysis was on the contribution of the subgrid model, a comparison of grids of different orders to ascertain proper resolution, the

analysis of rough walls boundary conditions, and the analysis of the effect of the exhaust plume on the flow field inside the diffuser. The main geometries under investigation for the unheated, non-reacting scenario are FG14 and FG25 with special emphasis given to FG14; however, validation of the non-reacting pressures in FG11 were also performed and shown in Figure 7.3. One can see the best agreement with experimental results is produced using the implicit LES method with Smagorinsky and RANS models performing more poorly inside the cavity region of the combustor. This pattern was observed in different geometries as well and is assumed to be a product of the complex turbulent interactions between the supersonic shear layer and cavity flow not being properly reproduced in RANS due to the averaging that occurs and an incorrect breakdown of the turbulent scales as modeled by the SGS Smagorinski model.

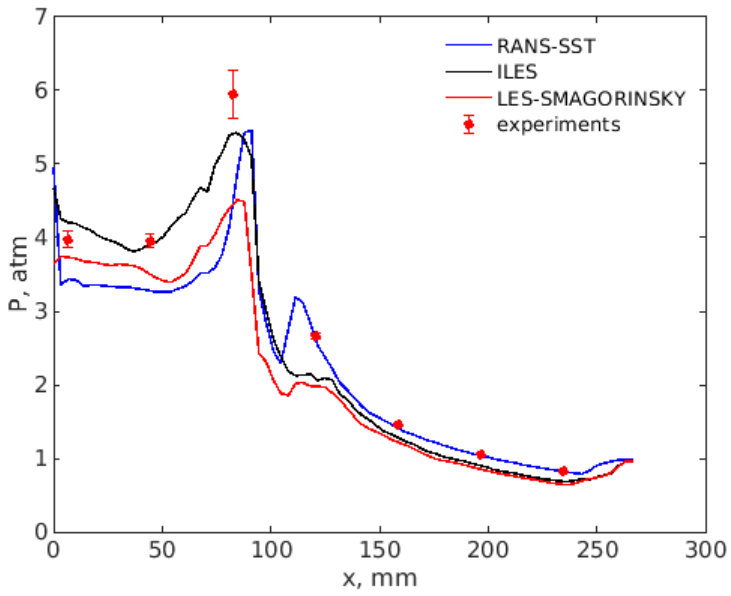


Figure 7.3: FG11 pressure comparison in cold, non-reacting flow

7.2.1 Contribution of the Subgrid Model

Three subgrid models are analyzed using the FG14 test case and the second-order polynomials mesh and solution reconstruction, using 27-nodes hexahedral meshes (typically such a solution is called a third-order CFD solution in computational fluid dynamics). They are plotted in figure 7.4 alongside the RANS prediction. This comparison shows that the RANS steady solution is not accurate to determine the effect of coherent pres-

sure waves in the scramjet cavity, while all LES models perform significantly better. The comparison of the subgrid stress models shows that static Smagorinsky is not as accurate as the "dynamic" models WALE and VREMAN. The two models are very similar, with the WALE model providing slightly more accurate estimates in the chamber. The comparison in the diffuser section of the scramjet is poor for all models and the rationale behind this trend will be explored in more details in the next sections.

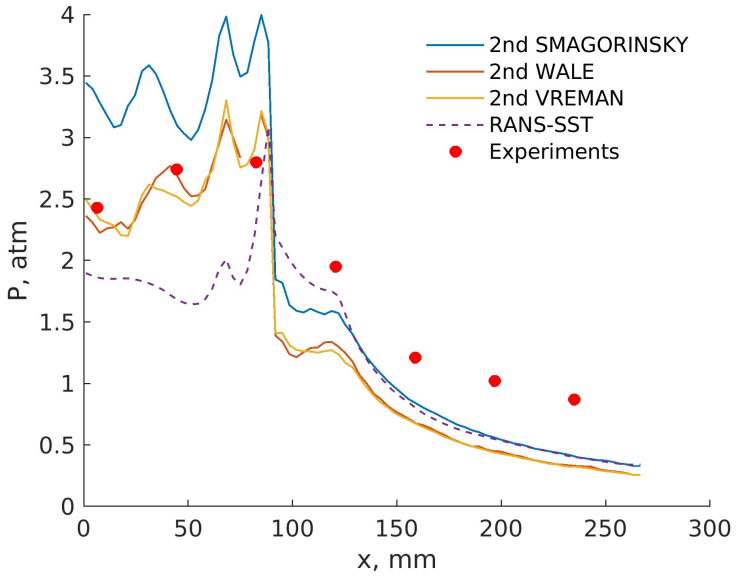
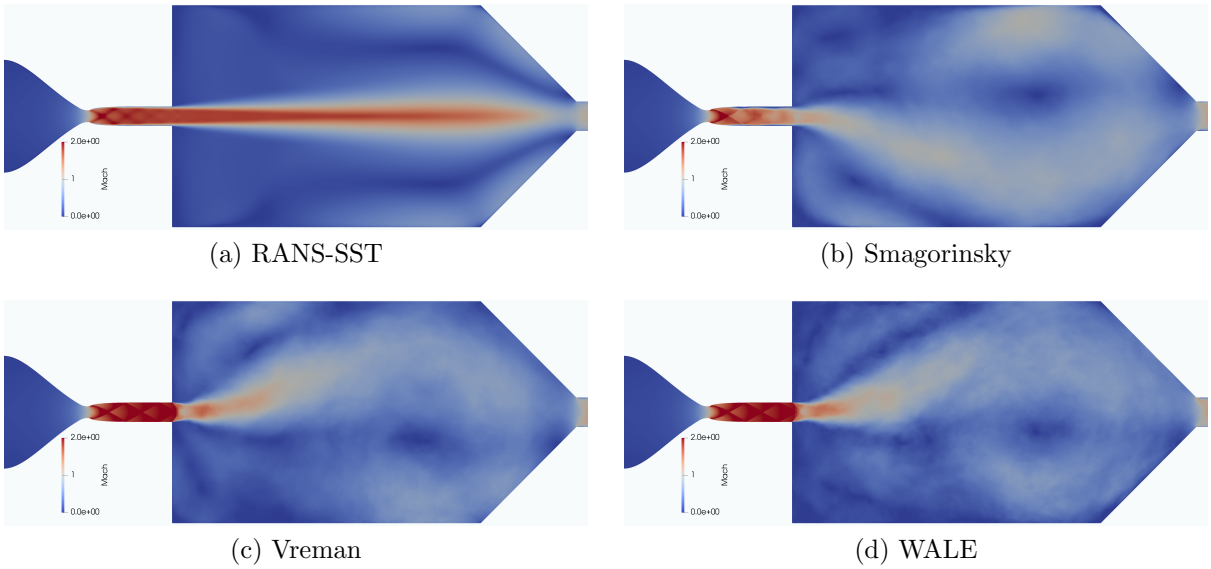


Figure 7.4: Effect of Subgrid Model on cold flow predictions in FG14

The reason why the Smagorinsky solution behaves poorly in the chamber is due to predicted separation in the straight walls of the nozzle. A comparison of of the mean flows supported by the four models is shown in figure 7.5. The simulations show that Smagorinsky supports a large recirculation area in the adverse pressure gradient region of the nozzle flow, i.e., after the expansion section. The large recirculation region leads to the formation of a secondary recirculation flow near the nozzle exit, which contributes to the increase of the pressure. Aside from the nozzle flow, all the LES models predict a non-symmetric mean flow. This outcome is in agreement with the experimental data, e.g., see Figure 7.6. The RANS solution is conversely symmetric which suggest that the lack of symmetry is related to the much larger chamber pressure in the LES simulations and the experiments. Therefore, we conclude that the unsteady coherent fluctuations of the LES and experiment contribute significantly to the increase in chamber pressure for

the cold flow.



(a) RANS-SST (b) Smagorinsky

(c) Vreman (d) WALE

Figure 7.5: Mean Mach number profiles of optically accessible scramjet test cases FG14



Figure 7.6: Experimental shadowgraph of FG14 flow bias in cold, non-reactive flow

7.2.2 Effect of Polynomial Order of Solution

The wall pressure distribution for first, second, and third-order polynomial meshes and solution DG basis are shown in Figure 7.7 using the Vreman model. These results show that the predictions using second and third-order polynomial bases (27 versus 64 nodes per each hexahedral mesh element) agree well with each other, while the first order meshes are not accurate enough and lead to overestimating the combustion chamber pressure. The third-order mesh is only marginally better in the diffuser section of the engine in matching the experiments. These computations indicate that under-resolution is not the root cause of the underprediction of the pressure.

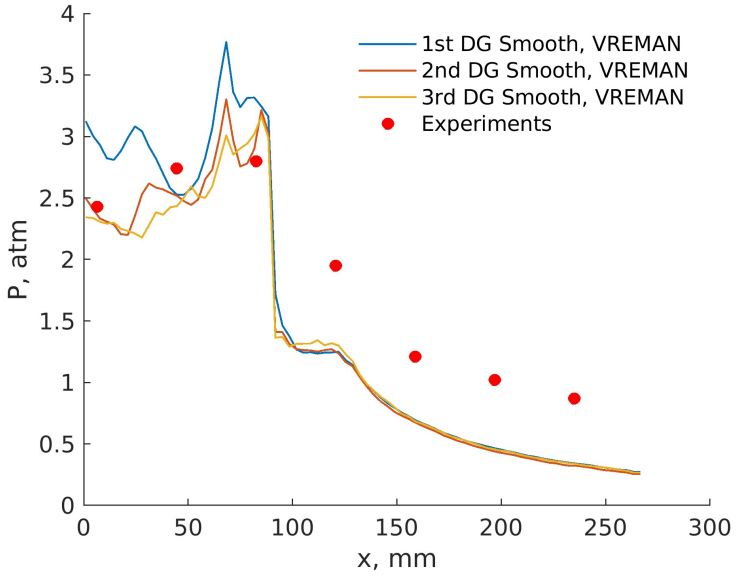


Figure 7.7: Effect of polynomial order on cold flow predictions in FG14

The three polynomial order grids have identical elements. The value of y^+ at the upper boundary of the first element off the walls has been adjusted to be smaller than 3.0 for all meshes. Yet, the third-order mesh has four nodes between the wall and the first element boundary, thus the boundary layer is better resolved. In order to test whether the boundary layer resolution is contributing to the poor results of the first-order grid, the same set of computations described by Figure 7.7 has been repeated with logarithmic wall functions of height $h = 10^{-4}$ and 2×10^{-5} meters. These computations showed that the boundary layer discretization is not responsible for the poor performance of the first order mesh, but it is due to the approximation of the complex eddies in the cavity.

7.2.3 Contribution of Rough Walls

Because the geometry was 3-D printed, microscope scans of the walls showed that the average wall roughness was approximately equal to 0.3 mm with a average value of $k^+ \approx 50$. This regime of rough walls characterizes flows that are neither hydro-dynamically smooth nor rough [146], therefore the bumps have been modeled from first principles by adding a sinusoidal variation of the wall height in the diffuser section. An image of the wall pressure distribution showing the roughness elements is included in Figure 7.8.

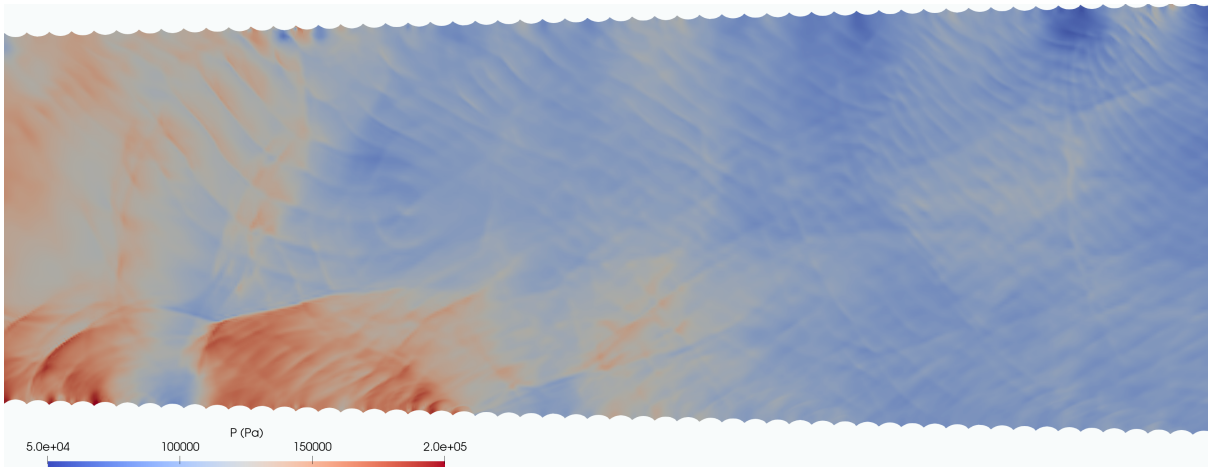


Figure 7.8: Instantaneous pressure field of FG14 with rough walls in the expandion section

The results of the analysis of the roughness conditions are shown in Figure 7.9 for both the rough and smooth walls with third-order meshes and Vreman SGS. The comparison of the two cases suggests that rough wall boundary conditions are only important in the constant area section of the diffuser where an adverse pressure gradient is supported by the rough walls, which brings the LES predictions closer to the experiments. In the expanding section the favorable pressure gradient decreases the importance of the wall interactions, and the disagreement between calculations and experiments cannot be explained by wall effects.

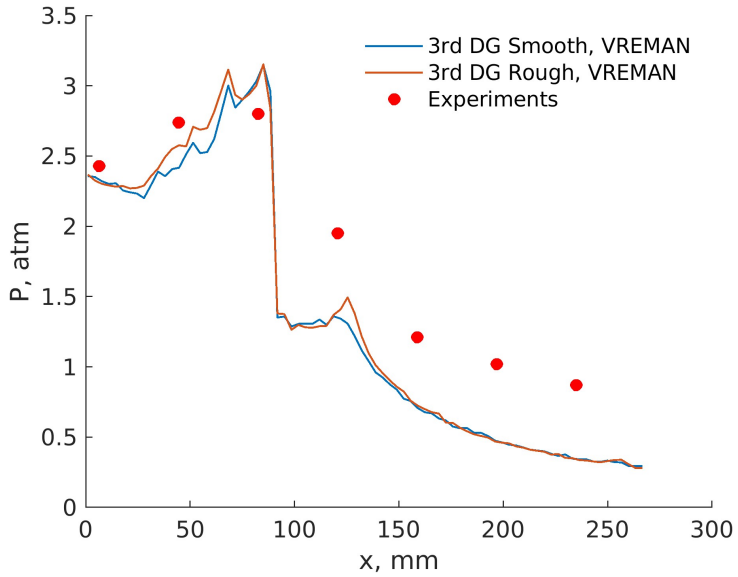


Figure 7.9: Effect of wall roughness on cold flow predictions in FG14

7.2.4 Contribution of the Exhaust Plume

The effect of the exhaust plume from the test setup is significant, because the ratio of exit pressure to back pressure is small, when supersonic exit boundary conditions are assumed. The plume boundary condition is simulated using a mixed inlet-outlet boundary condition at an elliptical bubble of length 0.14 m and height 0.04 m. The exit pressure has been maintained at 1 atm for this simulation and the total temperature needed for the mixed inflow condition is at 300 K. The simulations discussed in this section used the second-order DG bases and rough walls boundary conditions. A comparison of the pressure distribution with and without the plume is shown in figure 7.10. The agreement with the experiment is significantly better leading to the conclusion that not-perfectly expanded conditions are the cause of the disagreement between predictions and experiments in the previous sections. The cavity conditions are weakly affected by the plume because the time-averaged core flow is supersonic in the diffuser. Therefore, the burning simulations were conducted without the plume.

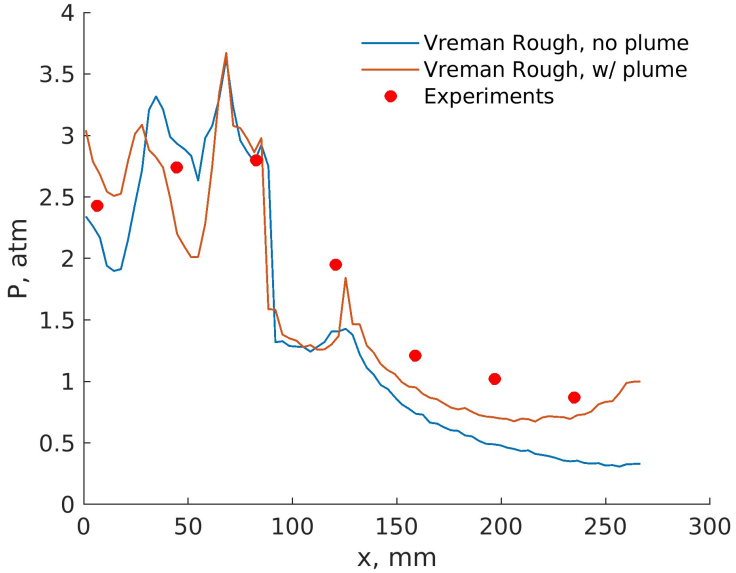


Figure 7.10: Comparison of the effect of plume exit conditions on the pressure in the FG14 combustion chamber.

7.2.5 Different Cavities

A comparison of the predicted and measured wall pressure for the shorter cavity FG25 is shown in Figure 7.11 without the presence of plume or rough wall effects in the domain.

The main observation is that the shorter cavity supports higher pressure because of the larger importance of pressure fluctuations, and that consequently the effect of the plume is less. Therefore, the agreement in the diffusing section is improved when compared to the FG14 case. The under-predicted pressure in the expanding section is once again due to the over expansion of the flow through the nozzle as can be seen by the pressure at the outlet.

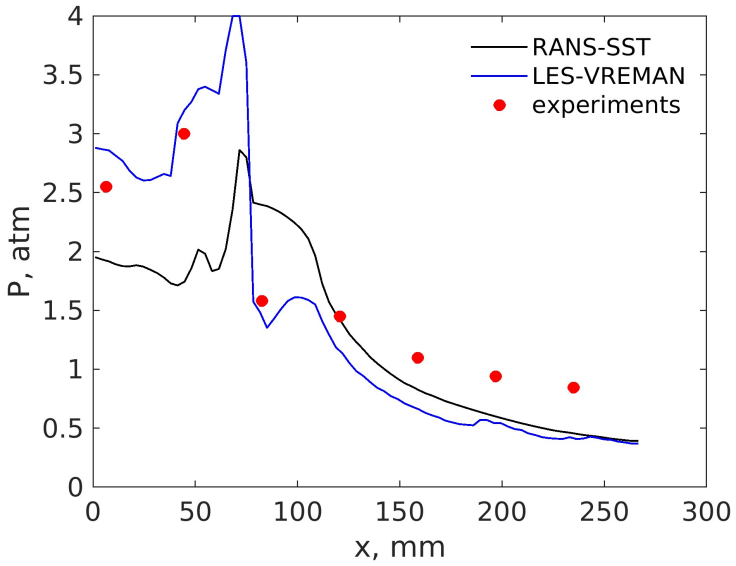
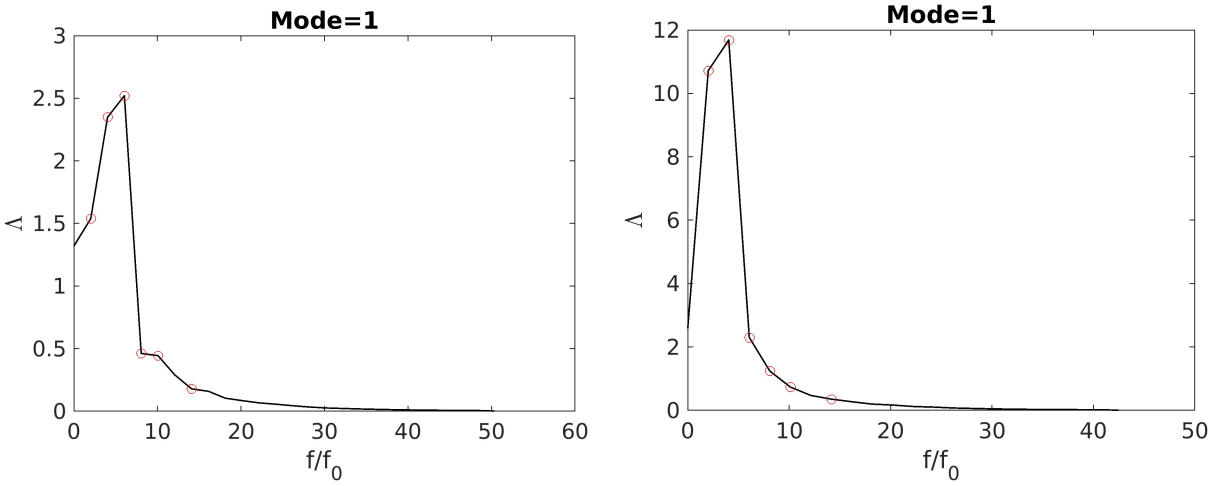


Figure 7.11: Comparison of measured and computed wall pressures for the shorter cavity, FG25.

7.2.6 Spectral Proper Orthogonal Decomposition (SPOD) of Cold Flow Modes

The comparison between LES averages, RANS, and experiments presented in the previous section showed that pressure waves in the cavity non-linearly contribute to the mean and are responsible for the bias noticed in the experiments. Shorter cavities support a larger chamber pressure. The difference between the SPOD modes supported by both cavities (FG14 and FG25) is examined first by analyzing the spectral energy density of the most coherent modes as function of the frequency. The reference frequency in the present context is obtained based on the acoustic speed in the cavity, $f_0 = 1/2a_0/L_c$, where a_0 is the speed of sound at the inflow air total temperature and L_c is the length of the cavity. The spectral energy density measured in bar $\cdot$ m^3 of the most coherent SPOD mode at

different frequencies is shown in Figure 7.12.

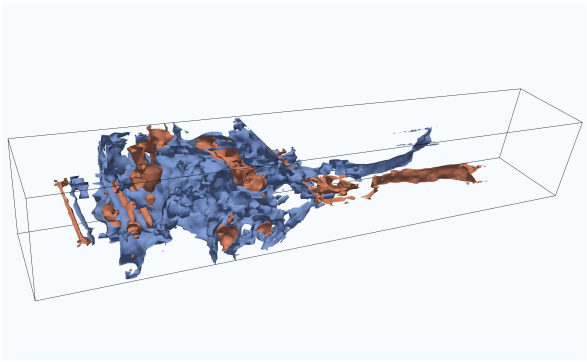


(a) FG14 (b) FG25

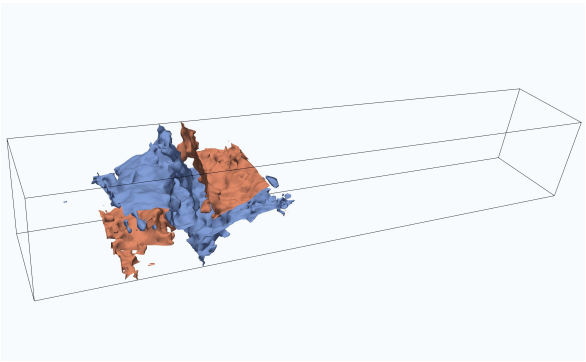
Figure 7.12: SPOD modes spectral energy density in bar $\cdot$ m^3

The most amplified modes are quite larger than those based on the acoustic frequency, with an acoustic Strouhal number approximately equal to 6. The shorter geometry supports a much stronger fluctuation energy and more energetic modes, leading to the conclusion that the cavity size contributes to the wave formation.

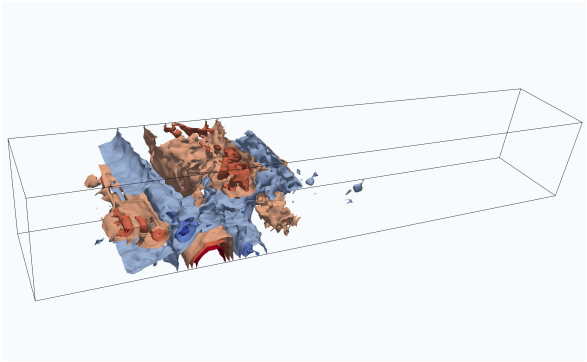
The dimensionless mode distributions for both cases at three frequencies are shown in Figure 7.13. Dominant modes are antisymmetric and biased as the mean flow previously discussed in Figure 7.5. High-frequency modes are confined to the cavity, while low frequency counterparts extend in the diffuser section. The FG14 cavity flow is biased towards the bottom and maximum pressure fluctuations occur near the bottom surface just before of the 45° inclined wall of the cavity and at the shear layer. On the contrary, in the smaller cavity the largest pressure fluctuations are on the inclined wall. The flow is not biased and pressure fluctuations resonate between the top and bottom inclined surfaces that close the cavity space.



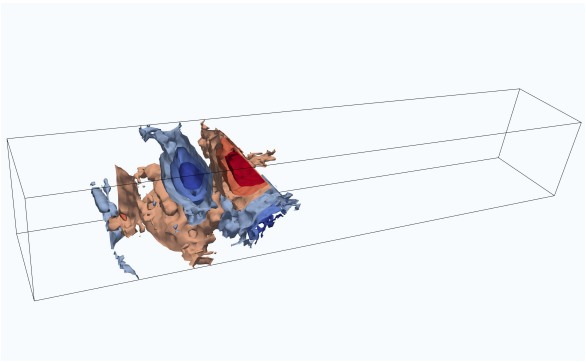
(a) FG14, $f = 2f_0$



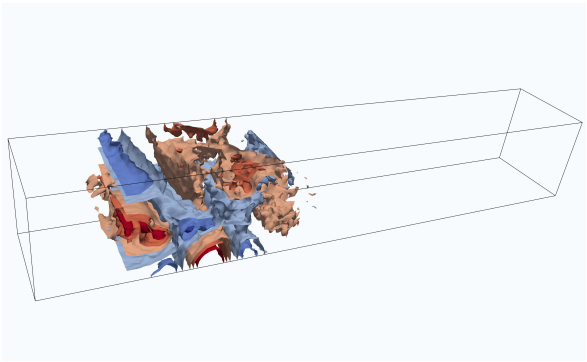
(b) FG25, $f = 2f_0$



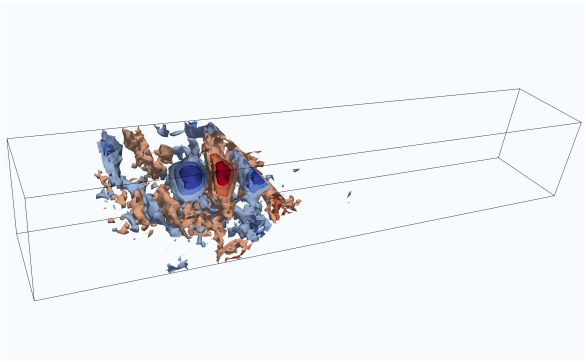
(c) FG14, $f = 4f_0$



(d) FG25, $f = 4f_0$



(e) FG14, $f = 6f_0$



(f) FG25, $f = 6f_0$

Figure 7.13: SPOD modes dimensionless eigenfunctions at the first three frequencies marked by open circles in figure 7.12.

7.3 Low Temperature Manifold Simulations

7.3.1 Reacting Ramjet Case

A comparison of the predicted cavity regression rates against the experiments suggests that the present model compares well with the experiments for the shallow cavities analyzed by Gallegos et al. [147]. Such a comparison has been discussed previously by Pace

et al [148] and Gallegos et al[12], and it is not shown here for brevity sake. The grid and boundary conditions for the ramjet simulation are summarized in Figure 7.14. Total conditions of $P_t = 0.47$ MPa and $T_t = 548$K were imposed at the inlet, and the exit was specified as an exhaust with atmospheric back-pressure. The flow is choked in burning conditions so the value of the back pressure is unimportant, and the outflow boundary is marked as supersonic outflow.

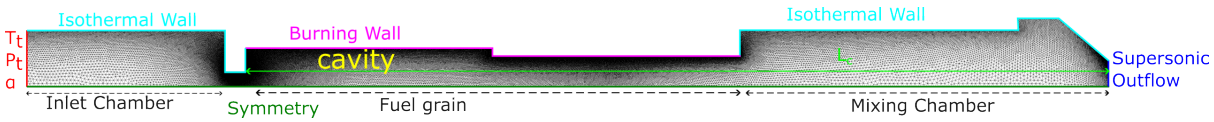


Figure 7.14: Schematic of the boundary conditions for the Ramjet simulations

As an initial validation method, mean chamber pressure (in the downstream mixing chamber) was compared at the experimental pressure transducer location. The mean chamber pressure sharply increases with combustion reducing significantly the injector Mach number and lowering the shear layer convective Mach number. These phenomena affect the fluid dynamics and acoustics in the mixing chamber. The numerical and experimental comparison is shown in Figure 7.15 where one can see numerical pressures tend to under predict experimental data by roughly 10%.

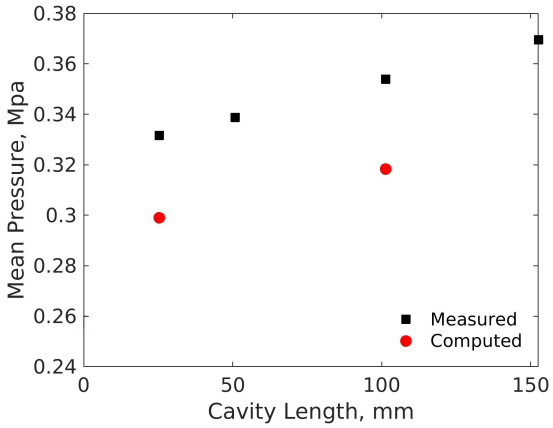


Figure 7.15: LES mean ramjet mixing chamber pressure compared to the experiments

The regression rates are evaluated on the undeformed configuration by averaging the LES results over a period of time of 0.02 s. Hence, the walls are not significantly regressed and a fixed-geometry computational analysis is carried out. Computed LES regression rates are compared to the experimental measurements in Figure 7.16 for the two shallow

cavities. Significant unsteadiness occurs in the cavity, and the coherent scales generated by the hydrodynamic instability are responsible for the majority of the heat flux to the fuel in the cavity. Convergence of the solution was analyzed by repeating the computations for the 152 mm shallow cavity over meshes with three element densities. Finer grid simulations lead to consistently reduced deviations from the experiments. The agreement between the model and the experiments is good for both cases under investigation. The largest disagreement is at low values of x/L, where the computed heat flux increases much more rapidly than the measured analog. This is due to the inaccuracy of the Smagorinsky turbulence model in the transitional region.

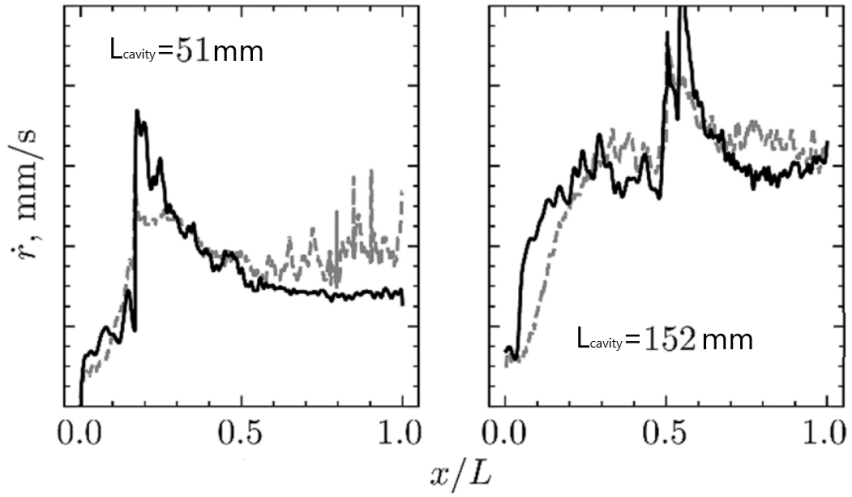


Figure 7.16: Comparison of ramjet LES regression rates (solid lines) versus the experiments (dashed lines)

The spatially integrated values of the heat flux to the fuel wall are 12.2 and 26.0 kW for the 51-mm-cavity and 152-mm-cavity cases, respectively. Therefore, the present calculations identify a substantial increase in the heat feedback for longer cavities. When combined with the experimental observation of a marginal increase in the combustion efficiency [12], this result points out that the cavity's major effect is to modify the heat transfer and not the chemical reactions. This feature will be analyzed in more detail in the following section. Notice that the calculated heat flux at all points uses the local normal to the surface. Similarly, the computed regression rate and normal velocity injection are both defined based on the local normal. In the experiments, the regression rate is evaluated in the radial direction only; but, because the regressed surface is flat

away from corners, this source of error was determined to be small as compared to other uncertainties, e.g., the temporal variation of the shape.

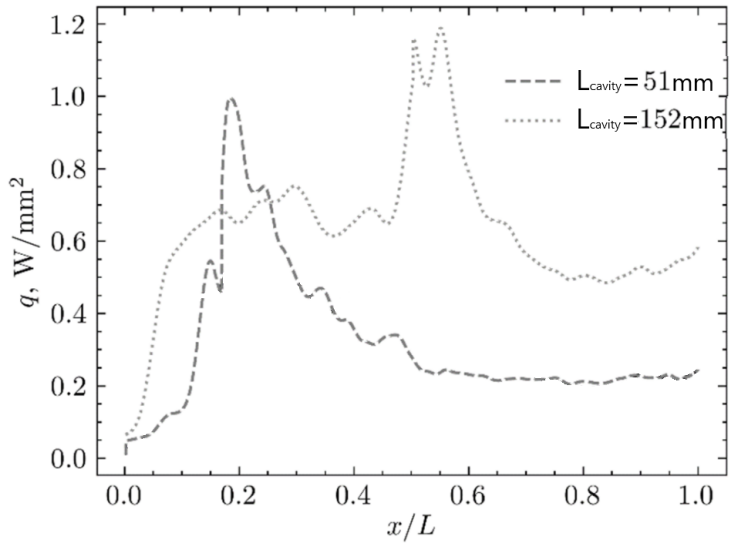


Figure 7.17: Comparison of ramjet LES heat fluxes (feedback to the fuel) for shallow geometries

The mixture fraction and temperature are shown in Figures 7.18 and 7.19, showing the presence of a substantial hydrodynamic instability and a recirculation region with fuel accumulation in the upstream part of the cavity. Eddies with unmixed fluid are convected toward the fuel surface in the shear layer where they react, producing a significant and localized increase in the heat transfer. The presence of recirculating flow in the cavity increases the complexity of the flow field. The contributions of the cavity hydrodynamics on the mean temperature field are significant and shown in Figure 7.19. The longer cavity case features a much faster increase of the temperature in the cavity due to the extension of the hot gas recirculation beyond the reattachment point. In this case, the edge conditions of the boundary layer on the fuel walls outside of the cavity are determined by the hot gas that has recirculated in the cavity, which explains the much larger regression and heat flux for $x/L > 1/2$ described in Figures 7.18 7.19.

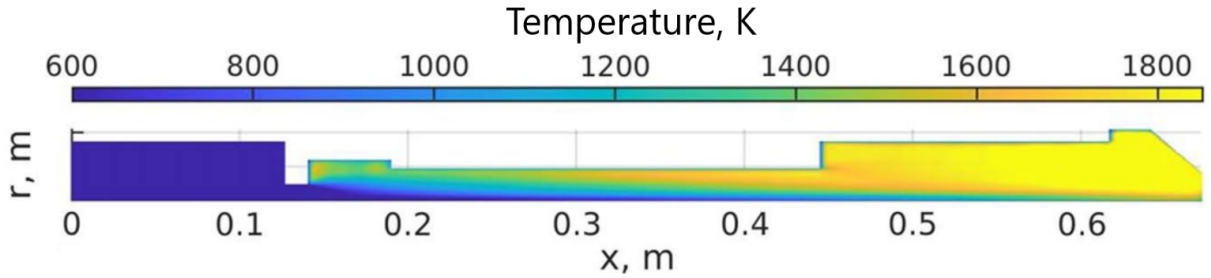


(a) 51 mm cavity

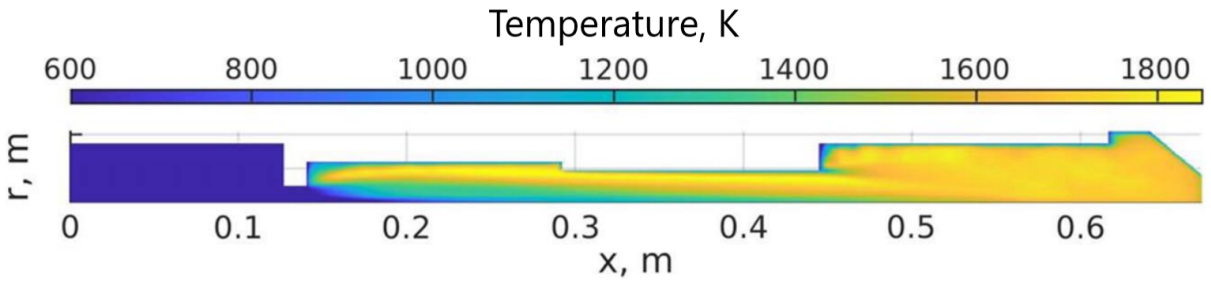


(b) 152 mm cavity

Figure 7.18: Mixture fraction in the LES ramjets at an instant in time during the statistically stationary evolution



(a) 51 mm cavity



(b) 152 mm cavity

Figure 7.19: Calculated time-averaged temperature fields in the ramjet

7.3.2 Reacting Scramjet Case

The 3D meshed geometry can be seen in Figure 7.20 where four different boundary conditions were implemented. The inlet used the stagnation values of $P_t = 11.9$MPa and $T_t = 600$K. The "wall" boundaries implemented a no-slip, adiabatic boundary. As one can see, a majority of the boundary elements are fuel wall boundaries which imposed a fuel inlet with injection rates as a function of the surface heat flux as seen in Figure 3.7. The outlet was a Riemann supersonic pressure outlet due to the assumption of fully supersonic flow at this location.

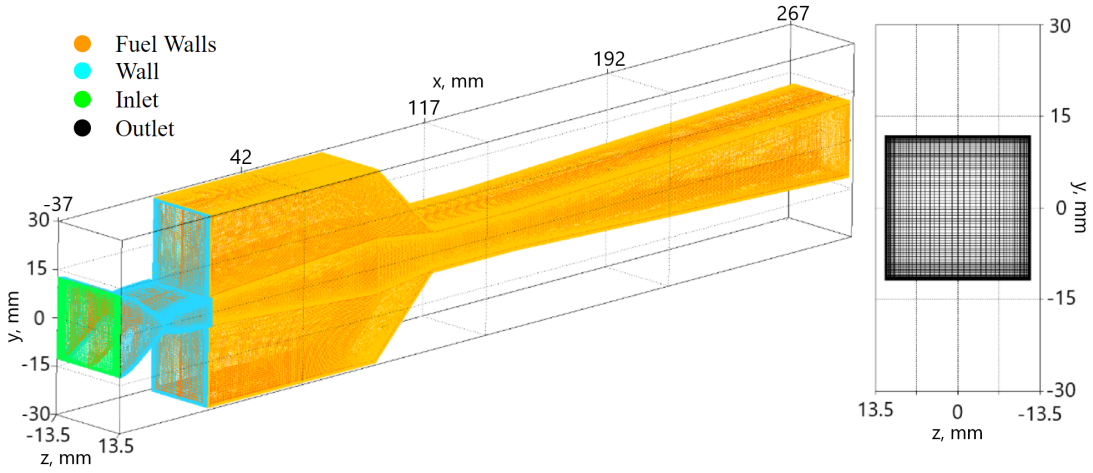


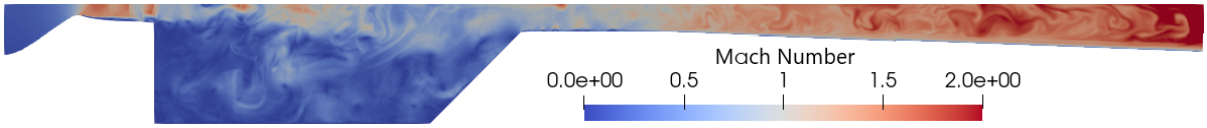
Figure 7.20: 3D mesh of FG11 with boundary labels

In order to confirm a grid-independent solution, three grids were simulated using 50, 160, 600 thousand elements in two dimensions and will be referred to as coarse, medium, and fine grids, respectively. These were each run to a quasi-steady state in order to obtain comparison. The three-dimensional grid has the same structure as the two-dimensional medium mesh but it also discretizes the boundary layers on the side walls with a total number of first-order finite elements equal to 3,200,400. The total number of degrees of (scalar) freedom of the three-dimensional FEM mesh is 25,602,480.

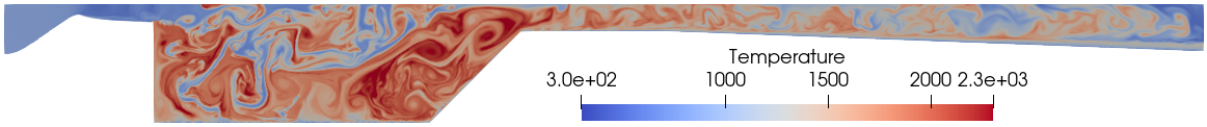
7.3.2.1 Numerical Solution Fields

The analysis of the burning scramjet experiment focuses on the initial part of the experimental measurements [142] when the solid fuel geometry can be assumed undeformed. A visualization of the instantaneous fields from the discontinuous Galerkin simulations including Mach number, temperature, carbon dioxide concentration (mass density), and mixture fraction are shown in Figure 7.21. The figure shows results along the center plane for the bottom half of the geometry ($z = 0, y < 0$). The instantaneous temperature and mixture fraction fields do a good job of displaying the highly turbulent flames and mixing that occur within the cavity. The instantaneous mixture fraction makes it very easy to identify the swirling eddies within the cavity and how this aids in increasing the rate of combustion as pyrolyzed fuel is stretched and twisted to more thoroughly mix with the oxidizer. The CO_2 concentration is indicative of the flame progress due to its representa-

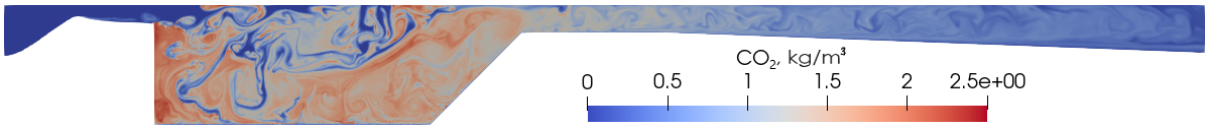
tion of the progress variable. It predictably shows a majority of the flame progress occurs inside the flame holding cavity with much fewer reactions taking place in the expanding section.



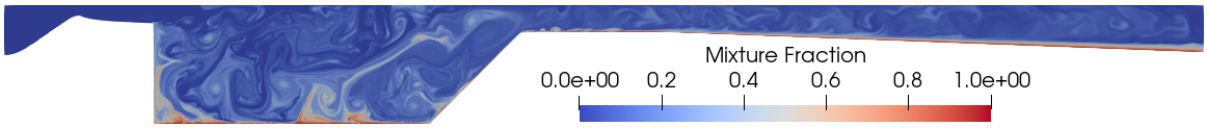
(a) Mach number



(b) Temperature



(c) CO_2 concentration

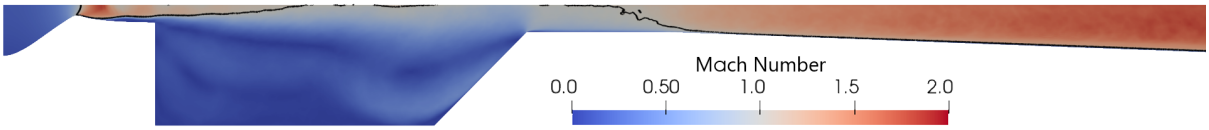


(d) Z

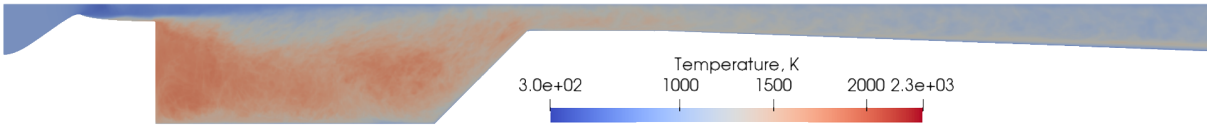
Figure 7.21: Instantaneous snapshots of the FG11 solution fields

The corresponding time-averaged quantities are shown in Figure 7.22. The first plot includes the contour of the sonic line which displays a supersonic flow above the first half of the cavity followed by thermal choking and a transonic region above the second half. At the expanding section, the flow once again becomes supersonic. The mean temperature remains the highest near the rear-facing wall of the cavity and in the middle-depth region of the rest of the cavity due to the long species' residence times and mixture fractions associated with these locations. The highest CO_2 concentrations are shown to be near the rear-facing cavity wall. This is unsurprising due to the time it takes species to recirculate and reach this location. The mixture fraction's color contour indicates that large amounts of fuel is transported from the ramp and depths of the solid boundaries towards the cavity center and rear facing wall by the recirculation region where it is able to supply heat flux thus pyrolyzing more fuel to sustain this process. The large gradient in the mixture fraction normal to the walls in the expanding section indicates the inability of fuel to

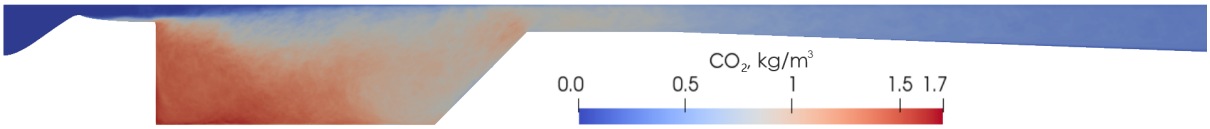
enter the free stream due to high flow velocities relative to the diffusive mixing. The lack of mixing in this region leads to a decrease in thermal coupling and thus a lower regression rate in the expanding section. This trend is explored in more detail later in this section.



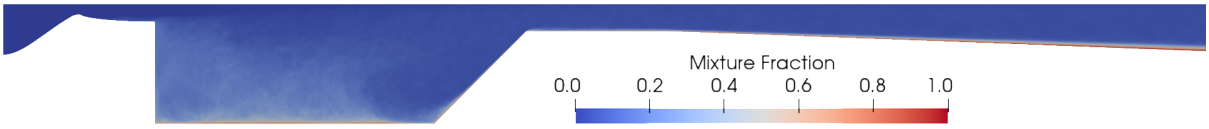
(a) Mach number



(b) Temperature



(c) CO_2 concentration



(d) Z

Figure 7.22: Mean distribution of FG11 fluid field solutions

Figure 7.23 shows the burn rate along the solid fuel walls. One can see it is greatest near the constricted area at the back of the cavity due to the high pressure and flow impingement in this region. Another region of high regression rate is near the mean flow path through the center of the cavity. The high velocities associated with this region create thin boundary layers that bring flames much closer to the fuel surface and thus increase the heat flux in this region. In a non-fixed mesh, one would thus expect the majority of the fuel wall regression to occur near the inclined surface at the back of the cavity and in the center of the y-axis on the side walls. The result of this regression would be an increased area near the thermally choked portion of the flow which - if regression patterns did not change drastically - would eventually result in a flow that is supersonic throughout the combustor.

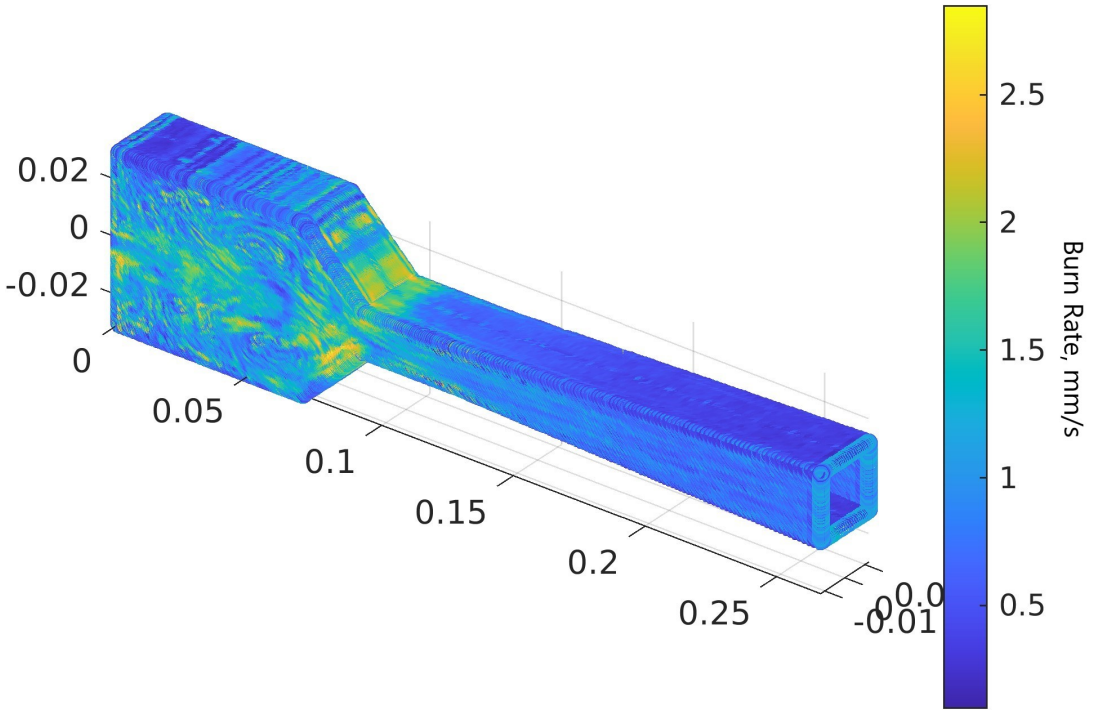
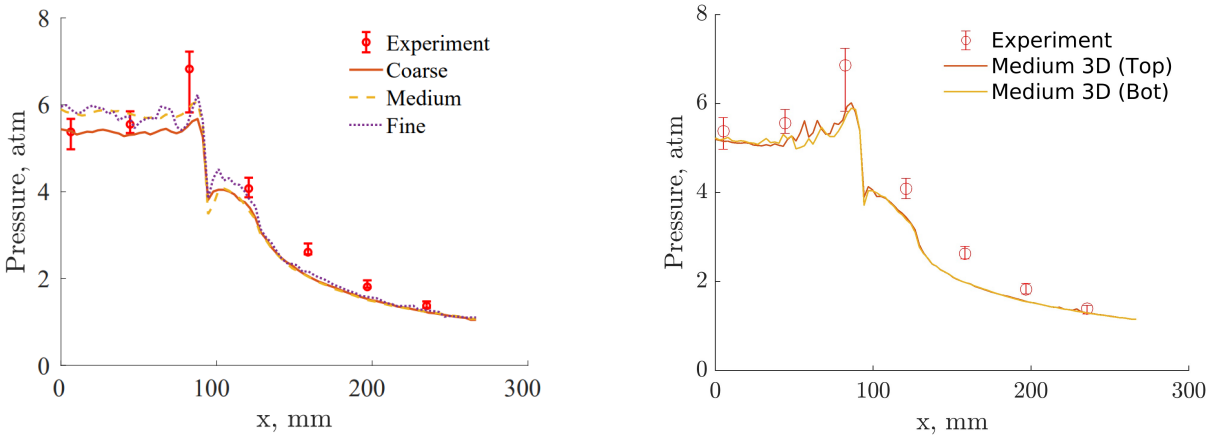


Figure 7.23: Burn rate of FG11 solid fuel walls, mm/s

7.3.2.2 Validation

Because this experimental geometry was not optically accessible due to the boxed fuel grain geometry, validation was performed using the pressure probe data and fuel regression rates. Experimental pressure data was taken at seven discrete locations along the top surface using wall pressure probes. This allowed for time-dependent data, so researchers could observe the rapid changes that occurred near ignition due to the consumption of the starter propellant. In order to make a numerical comparison with minimal interference from the high-energy igniter propellant, pressure data from time $0.5 < t < 1.0$ seconds was used. This data can be seen in Figure 7.24a where the circle is the mean value and the error bars represent the high and low pressures in the sampled time range. One can also see in this figure that the medium and fine mesh solutions are nearly identical throughout the domain, and the coarse mesh only varies from the other two inside the deep cavity portion. The three-dimensional pressure variation shown in Figure 7.24b is very close to the two-dimensional analog, yet it features a slightly larger value of the peak pressure, due to the significant contribution of coherent three-dimensional pressure fluctuations to the mean.

Numerical results differ slightly form experimental recordings at the end of the cavity ramp before the diffuser and near the middle of the expanding section. These could be due to a rapidly changing geometry near the diffuser that would thus change the area of this constricted section. Simulations show this is initially a choke point, and thus an increase in its area would decrease the throat to expanding section area and cause an increase in the expanding section's pressure. As the diffuser opens up, the subsonic flow near the ramp would travel at a proportionately slower speed and thus lead to an increase in pressure at probe location 3 near $x = 80$mm. As the diffuser continued to increase in area, the cross sectional area would eventually become large enough to support supersonic combustion throughout and the pressure would begin to decrease at this probe location [142].

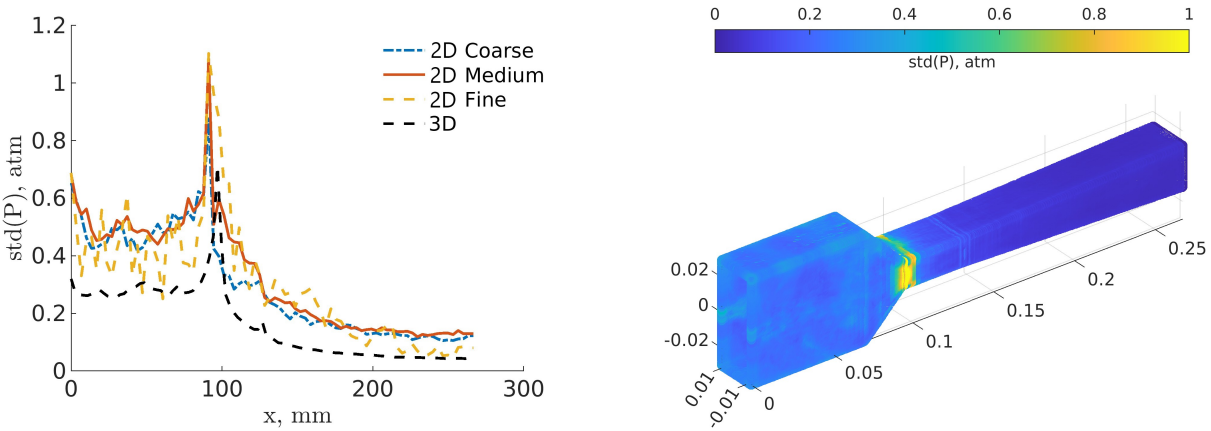


(a) Two dimensional simulations

(b) Three dimensional simulations

Figure 7.24: Wall pressure at 7 probe locations in FG11 reacting case

While three-dimensional coherent scales have a weak effect on the mean pressure LES results, they have a more substantial effect on the pressure fluctuations. A comparison of two-dimensional and three-dimensional LES is shown in figure 7.25a, where the standard deviation is evaluated using the one-dimensional recordings shown in figure 7.24b. It is important to notice that in the three-dimensional case, the strongest pressure fluctuations at the ramp are located at the side wall, and are sustained by lateral modes of the cavity shear layer. The reduction of the pressure fluctuations has important consequences on the combustion fields as analyzed in what follows.



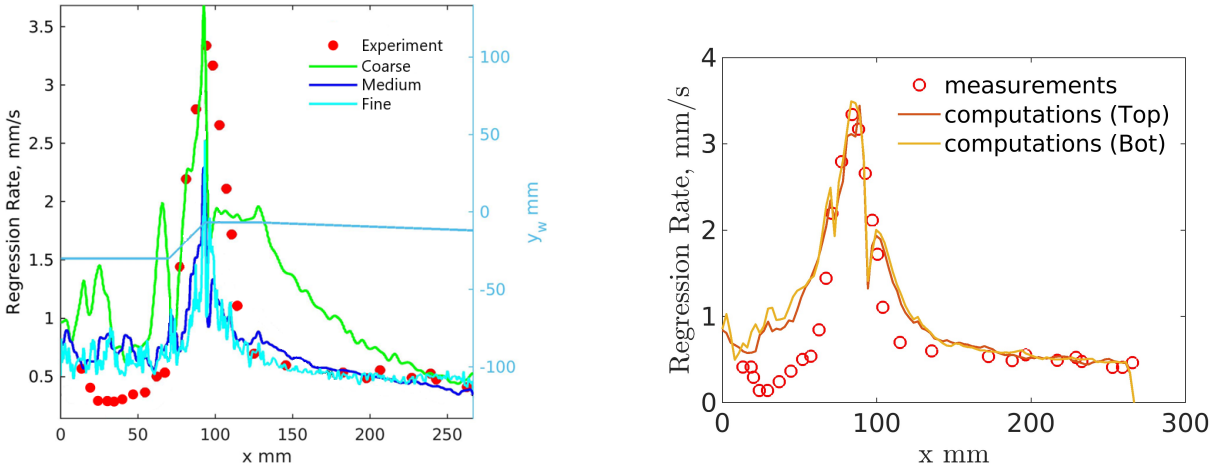
(a) Center-line (b) 3D Distribution

Figure 7.25: Standard deviation of wall pressure in FG11 reacting case

Averaged regression rates were also found experimentally by cutting the fuel grains after combustion, finding the total regression, and averaging this over the time of combustion [142]. To minimize the effects of the igniter propellant while also accounting for experimental geometry changes throughout combustion, two experimental runs were performed with combustion times of three and six seconds due to the assumption that the igniter propellant strips were completely consumed within the first three seconds of combustion. This assumption was made due to there being no notable regression of the fuel in the region obscured by the igniter propellant before three seconds. The regression rates of both of these trials were recorded and averaged in order to obtain an averaged regression rate of the fuel walls. Measurements of the post-combustion fuel grains were taken along the centerline, so computational regression rates were also taken along this plane.

The two-dimensional comparisons can be seen in Figure 7.26a where multiple grid solutions were plotted next to experimental results. One can see both the medium and fine refined grids produce very similar results, and the largest difference between the coarse and more refined grids occurs in the diffuser. One can see the computational regression rates match experiments well in the expanding section but rather poorly on the ramp. The low regression rates in the expanding section are likely a product of several factors including lower pressures and the previously noted lack of active combustion in this region. As seen in 7.22, very little fuel is able to diffuse into the mean flow

in the expanding section which results in less combustion, a lower temperature, and a decrease in the fuel injection/regression rate. Any flames that travel from further upstream quickly dump heat into the fuel walls to pyrolyze the surface, but due to low mixing and residence times, this pyrolyzed fuel is never able to fully react and create the heat feedback required to increase regression in the expanding section. One will note that inside the cavity, there exists a significant discrepancy that could be due to several factors including improper recreation of species diffusion or effects of the previously mentioned igniter propellant. The three-dimensional rates shown in Figure 7.26b feature a much-improved agreement versus the experiment especially near the ramp. The rationale is the lower unsteadiness of the three-dimensional computations supported by both the span-wise scattering of pressure waves hitting the ramp and the energy transfer to the span-wise modes of instability of the Mach 2 shear layer. This conclusion is based on an extensive investigation of pressure wave-fuel interactions in solid-fuel ramjets analyzed by the computations of Pace et. al. [11] and the experiments of Gallegos et al. [12]. Both studies indicate that the addition of small secondary cavities, contained within the reattachment region of the primary recirculation zone, can reduce the pressure waves induced by the thermo-acoustic coupling and significantly improve the flame-holding. The solid-fuel scramjet evaluated in the present studies behaves similarly, but the pressure waves are supported by energy transfers in the supersonic shear layer. Moreover, the burn rate maximum in figure 7.26b is wider than in figure 7.26a, due to more pronounced oscillations of the shear-layer impingement point on the ramp in the three-dimensional analysis.



(a) Two dimensional simulations

(b) Three dimensional simulations

Figure 7.26: Regression rate on four different FG11 grids

The pressure modes supported by the cavity can be evaluated using spectral proper orthogonal decomposition (SPOD) [149]. The spectral energy density of the fluctuations is plotted in figure 7.27 using 375 snapshots with a separation time of three microseconds. The results discussed below did not change when the number of snapshots was halved, thus the spectral analysis converged. The fundamental frequency $f_0 = a_0/(2L_c) = 3,973$ Hz is based on the average speed of sound in the cavity a_0 and the cavity length L_c. The analysis indicates that the maximum energy corresponds to a frequency $f/f_0 \approx 0.25$, which is close to the ratio of span to cavity length for this combustion chamber $W/L_c = 0.2653$.

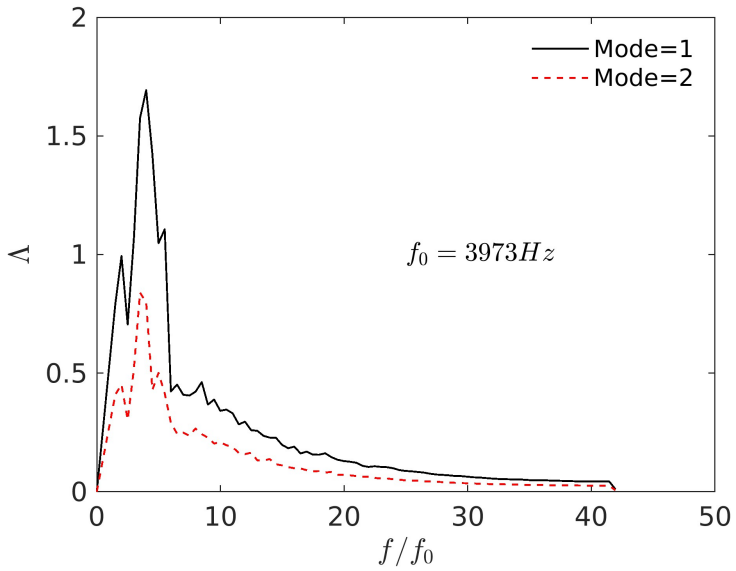
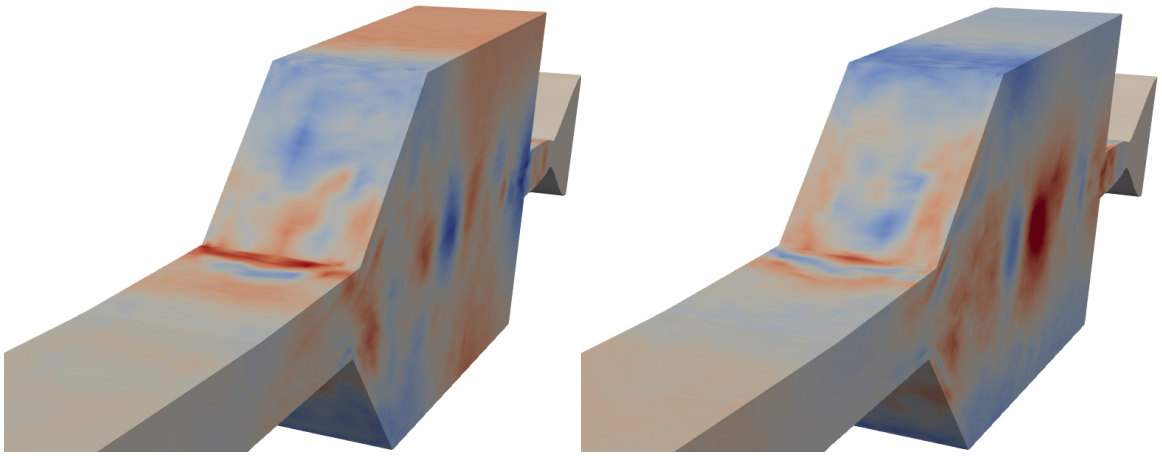


Figure 7.27: Spectral energy frequency of pressure fluctuation in FG11 solid fuel scramjet (atm/(cm^{3}Hz)).

The spatial energy distribution (spatial scales) corresponding to the maximally amplified frequency mode is shown in figure 7.28.



(a) Real (b) Imaginary

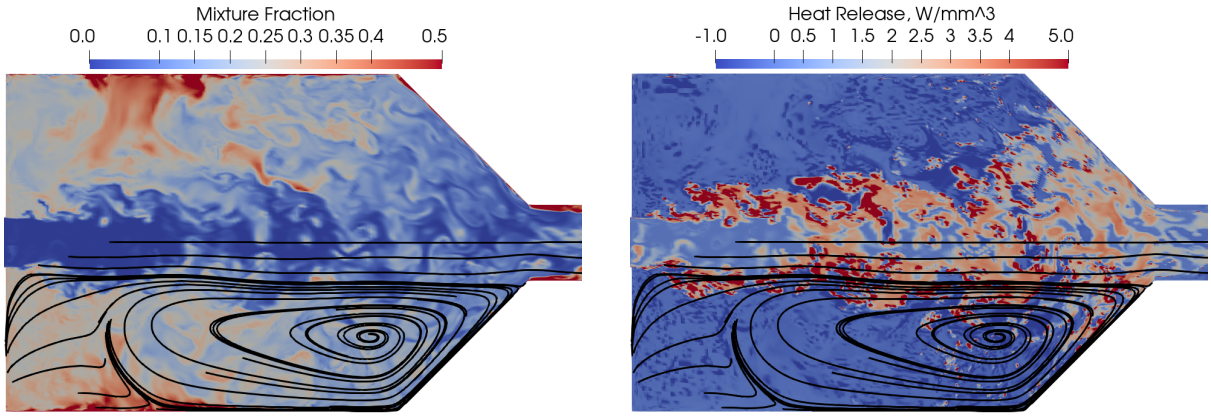
Figure 7.28: Real and imaginary parts of the most amplified FG11 SPOD mode

The pressure perturbation distribution indicates that a two-dimensional (i.e., zero spanwise wave number) pressure mode is created by the shear layer, scatters on the downstream ramp, and reflects back towards the chamber leading to a self-excited oscillation. The span length acts as the wavemaker by selecting the spatial wave numbers of the shear layer that are amplified by the coupled process. The SPOD analysis helps explaining the standard deviation of the pressure distribution shown in figure 7.25b and

the difference between two-dimensional and three-dimensional regression rates detailed in figure 7.26b. A more in-depth analysis of the self-excited instability will be published in a forthcoming work.

7.3.2.3 Discussion

The mixture fraction and heat release fields at a representative time in the operation of the solid fuel scramjet are shown in figure 7.29a and figure 7.29b, respectively, and reveal the main mechanism supporting combustion in the scramjet.



(a) Mixture Fraction (b) Heat Release Rate

Figure 7.29: FG11 instantaneous mixture fraction and heat release rate in W/mm^3

The large cavity structure provides the main flame anchoring mechanism of this flow. The largest pyrolysis rate occurs on the ramp as indicated in figure 7.23 near the reattachment point of the main shear layer shown by the mean-flow streamlines traced in figure 7.29b. The strong favorable pressure gradient keeps the boundary layer thin, thus the heat transfer and regression rate are substantial. Yet, the fuel does not burn there, because of the high strain rate and low air-to-fuel ratio. The flow patterns indicate large amounts of fuel are pulled from the ramp and brought down into the cavity (see, figure 7.29a). Near the middle of the cavity, some fuel returns to mix with the shear layer where it sustains the region with the largest heat release. These observations are in agreement with recent measurements of chemiluminescence and density gradients in an optically accessible solid-fuel scramjet cavity with similar nozzle conditions as the one under investigation [142]. Thus, the solid fuel scramjet sustains a combustion field fun-

damentally different from the solid fuel ramjet because of the shorter residence time of the fuel in the cavity.

The fuel that does not return to the shear layer continues to travel toward the front of the cavity and collect more fuel along the surface as it does so. The low Mach numbers coupled with the turbulent eddies and high pressures in this region allow the reactants to fully decompose into their products. One can see in Figure 7.22, the region near the rear-facing wall of the cavity supports flames that are nearly fully reacted. These flames that have fully or almost fully reacted interact with the supersonic shear layer and thus transport heat downstream and cause thermal choking. This high-temperature gas mixture then travels downstream where it dumps large amounts of heat into the ramp and diffuser so the cavity recirculation and pyrolysis process can continue.

Once in the expanding section, the mean flow begins moving much more quickly. This causes very thin boundary layers and short residence times for reactants. High-temperature products that have traveled from upstream near the cavity transfer heat into the fuel surface to provide pyrolyzation; however, because of low residence times and poor mixing in the expanding section, this new gaseous fuel is unable to react and provide further heat feedback into the surface. Because this section lacks the strong coupling seen in the cavity and ramp section, the heat transferred to the fuel in the expanding section is largely wasted and would likely decrease fuel efficiency in a real scramjet unless additional mixing stages were incorporated. Another cause for the lower regression rates in this section is the supersonic expansion. Even though some reactions are still occurring and the total temperature is increasing slightly, the increase in speed creates a corresponding decrease in static temperature which drives fuel regression.

7.3.3 B-Spline Surface Movement

While the previous results have used fixed geometries, in reality, the fuel surface will regress as it burns. Fuel grain 11 was not optically accessible, so researchers were unable to track the changing geometry during combustion. In order to gain insight into how the flow field changes with the evolving surface, a numerical method was implemented to

regress the pyrolyzing surface via a B-spline surface representation.

Large gradients in pressure, temperature, etc. are anticipated during combustion, and these peaks and valleys can cause corresponding peaks and valleys to occur on the fuel surface. As the surface mesh is adaptively updated, these abnormalities can cause distortion of mesh elements via stretching and pinching. If elements become too stretched, the region is less well resolved, and this will lead to improper simulation of fluids near these elements. When elements become pinched, the simulation time stepping can become very small due to the explicit numerical scheme used. If left unchecked, both of these element distortions could eventually cause element overlap and the production of negative Jacobians that would crash the simulation.

In order to overcome these challenges, the surface elements were moved using a second order B-spline basis. B-splines are a collection of piecewise polynomial functions, $B_{i,b}(x)$, where b is the degree of the individual polynomials such that the order equal to $b+1$; thus, for a second order B-spline $b = 1$. The values of x_i are where the polynomials meet and are known as the "knots" or "control points" of the function and range $i = 0, 1, 2, ..., m$. The individual polynomials must follow the equation:

$$B_{i,b}(x) = \begin{cases} \text{non-zero function} & x_i \leq x < x_{i+p+1} \\ 0 & \text{otherwise} \end{cases} \tag{7.1}$$

where the scaling factor, $B_{i,b}(x)$, is fixed under the condition:

$$\sum_{i=0}^{m-p-1} B_{i,b}(x) = 1. \tag{7.2}$$

This constraint applies to all knots between b and m. The Cox–de Boor recursion formula [150] is then used to create the B-splines. For a second order construction, this takes the form:

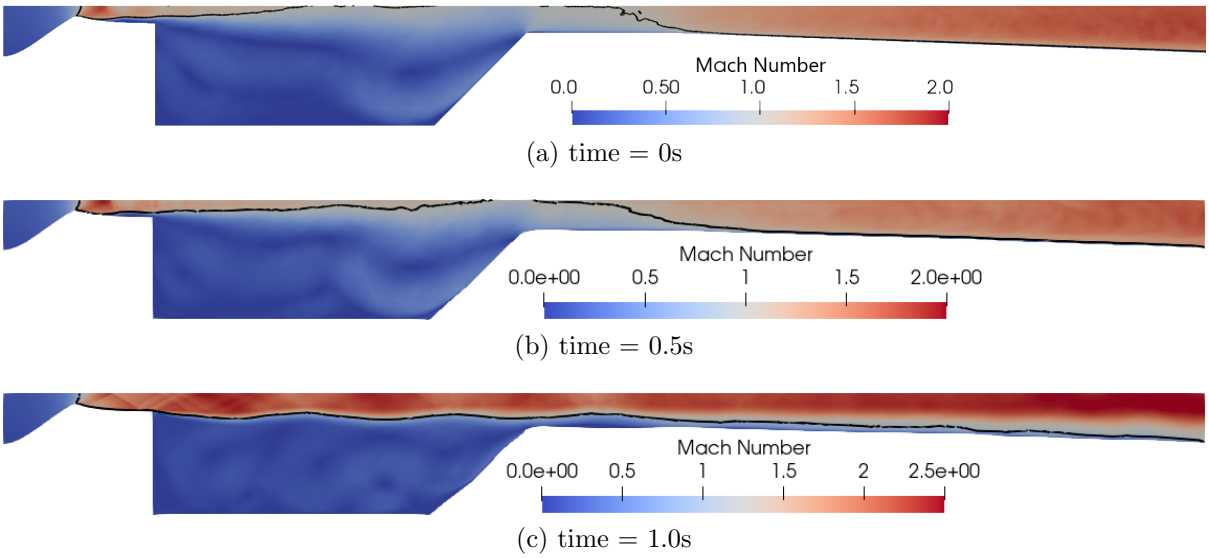
$$B_{i,1}(x) := \frac{x - x_i}{x_{i+1} - x_i} B_{i,0}(x) + \frac{x_{i+2} - x}{x_{i+2} - x_{i+1}} B_{i+1,0}(x) \tag{7.3}$$

where

$$B_{i,0}(x) = \begin{cases} 1 & x_i \leq x < x_{i+1} \\ 0 & \text{otherwise} \end{cases} \tag{7.4}$$

In order to properly move the surface elements, their movement is initially prescribed normal to the surface at a rate based on the heat flux as described in Section 3.3.2. Their movement is then applied to the control points using a reverse B-spline basis method. Once these control points have been moved, they act as knots which impose the shape of the new surface on the surface elements. Using this method, the surface is only smoothed based on element movement, so the algorithm does not attempt to unnaturally smooth preexisting features in the geometry such as the sharp corner at the end of the deep cavities. This method also allows the user to tune the details of a surface that can evolve. For example, using a greater number of control points would allow the surface to create more fine features whereas using few control points only captures the general movement of the surface and disregards smaller peaks and valleys that might otherwise try to form.

This B-spline method was applied to 2D simulations of fuel grain 11 in order to observe how the flow changes with time and altered geometry. In order to obtain a time averaged result at specific points in time, the geometry was regressed using the previously mentioned methods, but then fixed at 0.5 and 1 seconds. The simulations were then run to a quasi-steady state with these fixed geometries in order to produce the "time averaged" solutions for 0, 0.5, and 1 second of regression shown in Figure 7.30. This figure displays Mach numbers at 0, 0.5, and 1 second after ignition. It is clear to see as the surface regresses, the constricted area section opens up and no longer chokes the flow. The once highly unstable core flow over the cavity transitions from transonic to fully supersonic with visible expansion waves over the beginning portion of the cavity after one second of combustion and surface regression.



(a) time = 0s

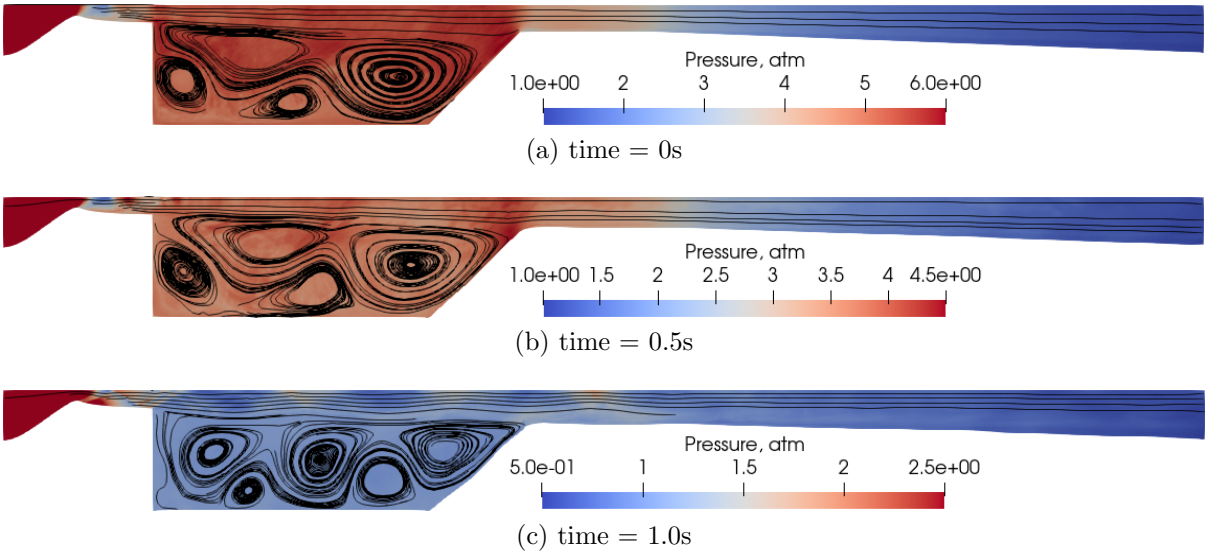
(b) time = 0.5s

(c) time = 1.0s

Figure 7.30: Mach number visualization at different times during combustion with black contour line representing the sonic condition

Figure 7.31 once again displays time averaged solutions at 0, 0.5, and 1 second after ignition with the coloring representing the static pressure inside the combustor and the black contours showing flow streamlines. One can see from Figure 7.31 the cavity pressure decreases as the constricted area section opens up, but this change is by far most significant in 7.31c once the core flow has transitioned to fully supersonic. This sudden drop in pressure is due to a shift in the flow impingement location on the rear ramp section of the cavity. In the initial geometry and geometry after 0.5 seconds of deformation, a stagnation region occurs near the end of this ramp section as seen from the streamlines in Figures 7.31a and 7.31b. This impingement caused a large, strong recirculation region to form near the back of the cavity. This turbulent structure aided in the breakdown of the supersonic shear layer and prevented the flow from transitioning to fully super sonic in the two initial geometries. After one second of combustion, the flow was no longer impinging on the ramp, and the recirculation regions within the cavity broke down into smaller, weaker turbulent structures. These eddies continued to support mixing, and their smaller size produced a more uniform mixture fraction distribution within the cavity which led to a more uniform temperature as well. Unfortunately, due to the stability of the supersonic core flow, the high temperature gas was no longer able to penetrate near the centerline of the expanding section. This lead to exiting gas having

a high temperature only near the fuel surface. This effect can be seen when viewing the Mach number in Figure 7.30c. Temperature and mixture fraction profiles of the 0.5 and 1 second post ignition geometries can be found in Appendix A, Figures A.6 and A.7.



(a) time = 0s

(b) time = 0.5s

(c) time = 1.0s

Figure 7.31: Static pressure visualization at different times during combustion with black contour lines representing streamlines

7.4 High Temperature Manifold Simulations

Similarly to the FRC comparison in a deep cavity geometry in Section 6.1, the ignition and extinction solutions showed similar results when implemented into the SFSJ simulations. Thus, the high temperature extinction manifold was implemented in the scramjet geometry and all results shown are from the extinction manifold. Meshes were generated using GMSH [151]. The 2D computational domains under investigation can be seen in Figure 7.32 now with the exhaust plume modeling discussed in Section 7.2. The experimental group from which these geometries are drawn used a preheating stage that caused the PMMA walls to undergo deformation prior to ignition [143]. While the incoming air was hot enough to causes surface deformation, it was not enough to spark ignition. After preheating, an upstream torch was used to heat the air to the 1200K hot library temperature and cause ignition. In this work, three meshes were investigated that represent the undeformed geometry prior to the preheating stage, the geometry at ignition, and the geometry after 2.67 seconds of combustion. The deformed geometries were obtained experimentally via tracking of the surface through the optically accessible SFSJ windows. One can see the initial geometry in figure 7.32a has a very constricting constant area section, but this has opened up significantly by the time of ignition in figure 7.32b and continues to increase in area to create the geometry seen in figure 7.32c. All geometries were frozen throughout the course of combustion, so no adaptive mesh algorithm was used. Boundary conditions in all meshes are the same. The upstream converging/diverging nozzle as well as the backward facing step at the front of the cavity are treated as adiabatic walls. All walls downstream of the initial backward facing step become fuel inlets that inject fuel as a function of heat flux, and the curved sections on the right side of the domain act as a pressure outlets in order to allow for a better understanding of the combustion and flow properties at the exit plane.



(a) Preheating Mesh



(b) Ignition Mesh



(c) 2.67s Post-ignition Mesh

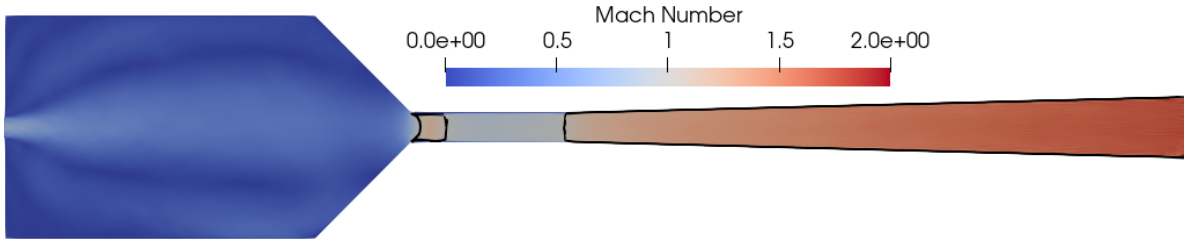
Figure 7.32: 2D structured meshes

7.4.1 Numerical Solution Fields

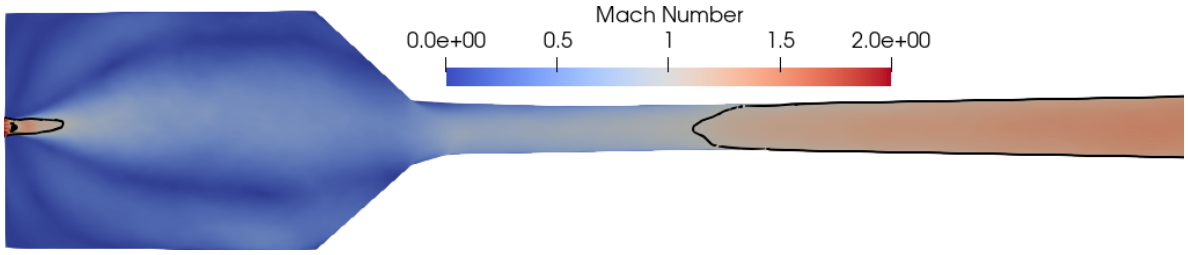
The mean averaged results of the meshes look qualitatively similar, but there are several differences that change the flameholding properties of the cavities. Figures 7.33, 7.35, and 7.34 show the time averaged Mach number, pressure, and temperature in the flow fields of interest.

The Mach number visualizations in Figure 7.33 use a black contour line to display the sonic condition. The restricted throat area in the pre-heating geometry seems to cause the flow to become subsonic prior to entering the combustor unlike the deformed counterparts which show thermal choking after the mean flow enters the cavity. The ignition and post-ignition geometries show the flow remains subsonic and transonic through the majority of the cavity section until reaching the constricted area section after the ramp. At this location, something slightly different occurs when comparing the preheating mesh and the deformed geometries. In the pre-heating simulations, a decease in the flow area followed by sharp turn leads to an adverse pressure gradient near the wall. This flow separation creates a choke point as the flow expands to turn around the corner. Because this is a constant area section and fuel is still being injected, the flow becomes forced out of the supersonic regime shortly after its brief transition. In contrast, the deformed geometries

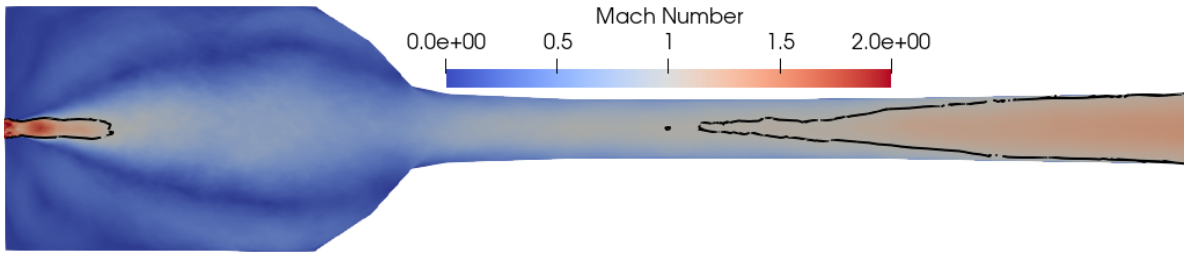
in Figures 7.33b and 7.33c create a slightly more gradual turn for the flow to follow. This, in conjunction with the geometry still converging after the initial turn, does not allow the flow to experience the same expansion as in Figure 7.33a after the flow separates near the walls. Thus, the deformed geometries remain transonic throughout the constricted area section. All three geometries show sonic transition one final time once the flow enters the diverging section, but it is important to note this transition occurs further downstream in the deformed geometries due to the opening of the constricted area section and change in choke location of the flow.



(a) Preheating geometry



(b) Ignition geometry



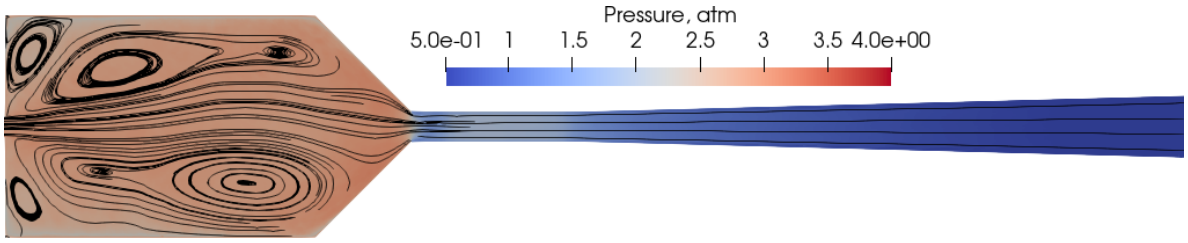
(c) 2.67s post-ignition geometry

Figure 7.33: Mean Mach number at three stages of FG14's deformation with black contour line representing the sonic condition

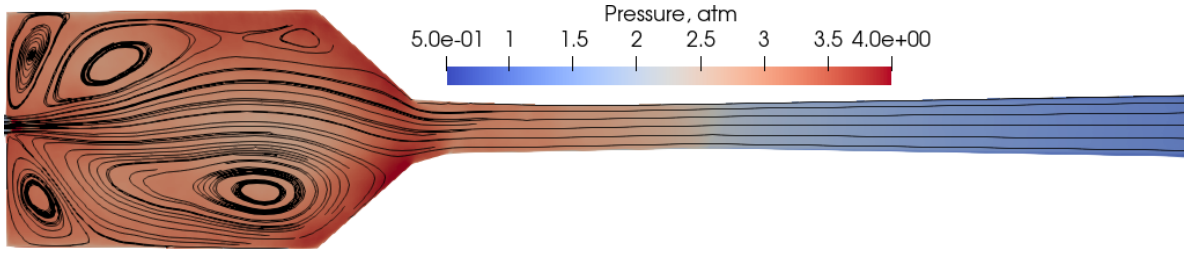
Pressure and streamlines are given in Figure 7.34 where non-symmetric recirculation regions are supported by the flow in all three cases. While this non-symmetry is not nearly as large as that seen in the unheated flow cases (7.5), it is still likely supported by the same physics, but weakened due to the higher pressure throughout the cavity. One subtle, but important distinction between streamlines in the three geometries is the size of the

recirculation regions near the rear facing wall of the cavity. As the supersonic core flow stretches further through the cavity section with time, the re-connection point between the cavity and core flow streamlines shifts downstream. This causes the recirculation zones near the front of the cavity to increase in size and provide a more optimal region for entrainment of fuels and flameholding. These regions are relatively small in Figure 7.34a, but quickly grow in Figures 7.34b and 7.34c.

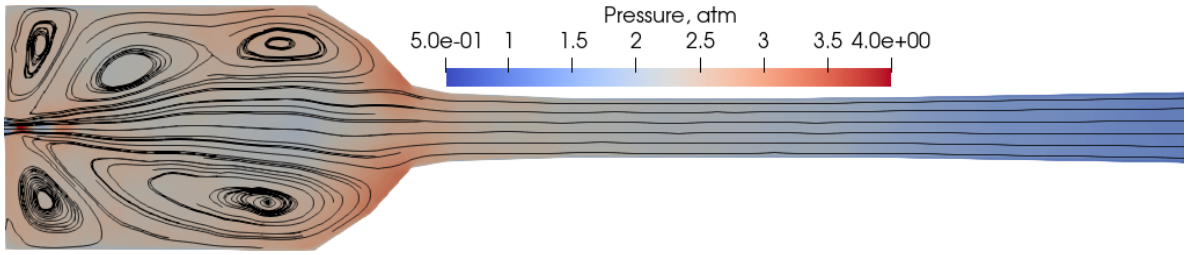
Another interesting aspect of Figure 7.34 is the change in cavity pressure from the preheating to ignition to post-ignition geometries. One will note the pressure increases from the preheating geometry to the ignition geometry but then decreases from the ignition geometry to the the 2.67s post-ignition geometry. The answer to this first increase in pressure can be found in Figures 7.33a and 7.33b. Due to strong choking in the constricted area section, the pressure within the preheating geometry rose enough to cause a shock upstream in the converging/diverging nozzle that was intended to transition the flow to supersonic. While this shock increased the pressure in the core flow, the total pressure losses reduced the recovery pressure inside the deep cavity recirculation regions. The ignition geometry did not experience this shock, and thus the recovery pressure within the cavities was higher. Later, the 2.67 seconds post-ignition geometry experiences a drop in pressure due to the continued opening of the constricted area section. As this area becomes larger, more flow is able to pass through. Due to the conservation of mass, a large cavity pressure was required to push fluid through this section in the ignition geometry, but the increased area in the post-ignition geometry's constricted area section allows for lower cavity pressures later during combustion.



(a) Preheating geometry



(b) Ignition geometry

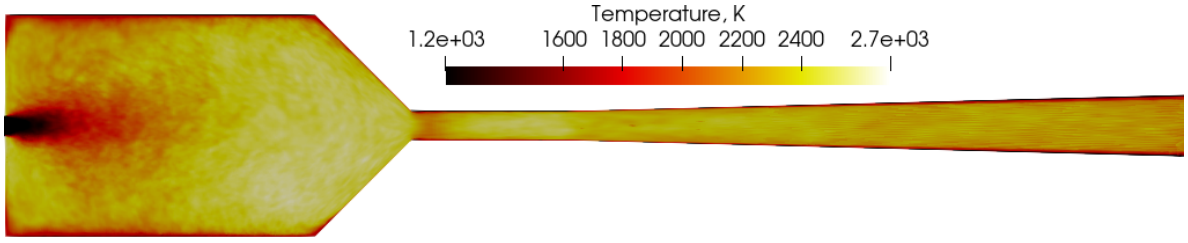


(c) 2.67s post-ignition geometry

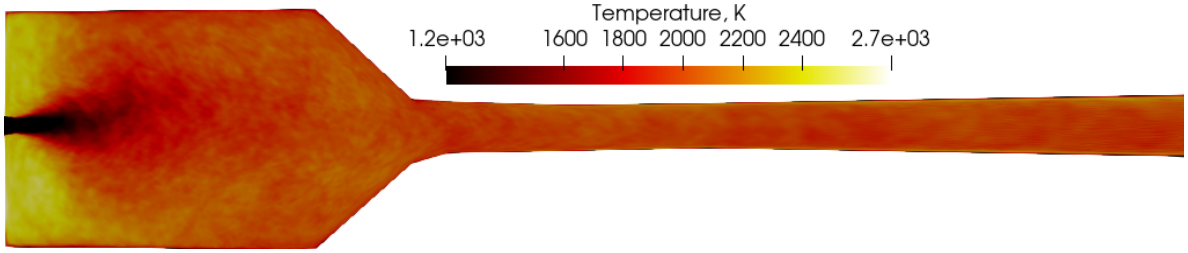
Figure 7.34: Mean pressure at three stages of FG14's deformation with black lines representing streamlines

Figure 7.35 shows very different temperature profiles in the preheating and deformed geometries. In Figure 7.35a, the slower flow allows the reactants more time to combust and thus the deep cavities are not as important for flameholding. In this preheating geometry, fuel seems to have time to react when traveling from the front to the back of the core flow through the cavity, and the maximum temperature thus sits near the end of the rear ramp section of the cavity. In contrast, the deformed geometries indicate a maximum temperature that sits near the back facing wall of the cavity. This is likely due to the residence time of species being the greatest near the back facing wall, thus giving chemical processes time to run their course and produce the temperatures seen. The physics that create these ideal flameholding structures stem from the increased size of the recirculation zones in this region. As the constricted area section opens, the major recirculation regions in the downstream region of the cavity slightly reduce in strength.

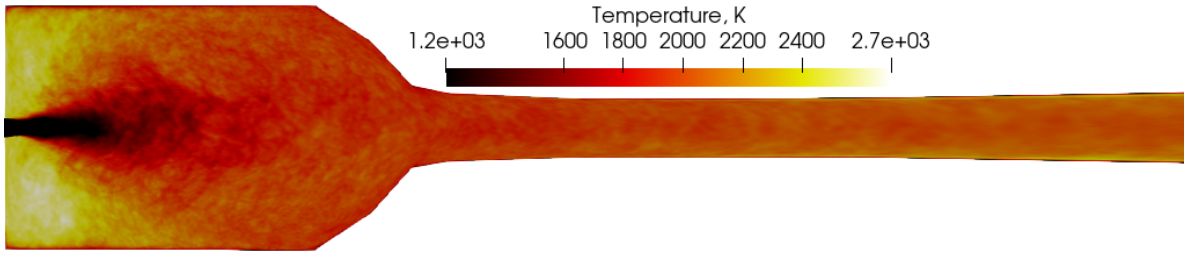
This decrease allows the smaller recirculation region in the font of the cavity to increase in size and provide a better foothold for reactants to decompose into their products. The location of these high temperature flameholding zones is also observed in experimental trials.



(a) Pre-ignition geometry



(b) Ignition geometry



(c) 2.67s post-ignition geometry

Figure 7.35: Mean temperature at three stages of FG14's deformation

7.4.2 Validation

While the flow streamlines might appear qualitatively similar, small changes in the flow profile can affect the regression rates and pressure profiles. Obviously, proper pressure modeling is important in capturing characteristics, but it also affects the combustion rate of the fuel. This combustion rate will increase the heat flux to the surface and thus increase the fuel regression and injection rate. This creates a strong coupling effect, so being able to predict how the geometry is deforming is imperative to long term characterization of combustion efficiency.

As one can see in Figure 7.36, the ignition geometry does an excellent job at reproducing the surface pressures. Because the area in the constricted area section has increased, the expanding section no longer undergoes as steep an incline, and thus the pressure does not decrease to the same degree as seen in the preheating geometry. The higher speed core flow through the ignition geometry's cavity also produces stronger impingement on the rear ramp of the cavity and thus a spike in pressure at this location as the flow is stagnated. A final feature worthy of mention is the obvious shift in slope around x=160mm in the ignition geometry. Because of the significant changes in the constricted area section's profile, this has now become the most constrictive area, and that causes choking and supersonic transition. Previously, the flow expansion occurred near x=120mm, but this has now been shifted further downstream due to a changing geometry.

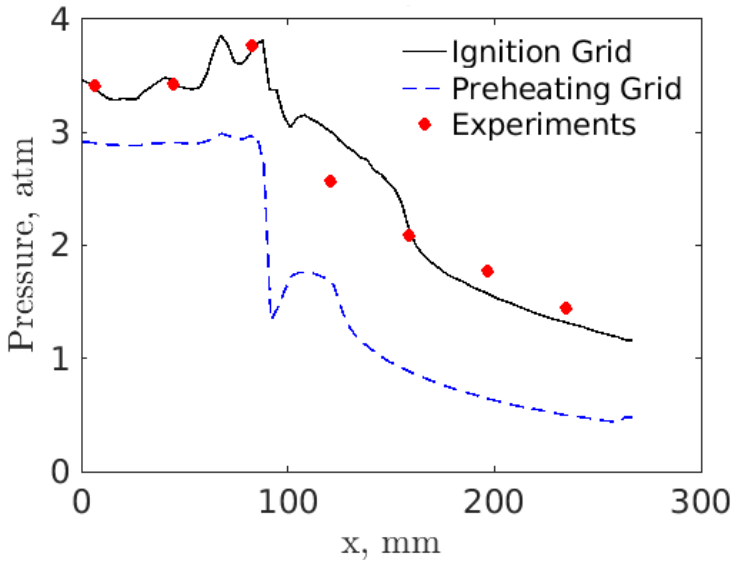


Figure 7.36: Comparisons of pressure along the fuel surface at ignition

The pressure along the centerline of the top fuel surface after 2.67 seconds of combustion can be seen in Figure 7.37 where experimental and numerical values are compared. Computational simulations agree well with the experimental results at all locations. One can see the high speed core flow once again impinges on the rear wall of the cavity creating a pressure spike as the flow stagnates. The core flow which is now moving more quickly than in ignition geometry produces an even larger spike than that seen in Figure 7.36. After 2.67 seconds of combustion, the constant area section has opened up enough to make the expansion section much more gradual. The decrease in static pressure in this

section is now very linear as opposed to the parabolic decrease seen in the preheating geometry. The supersonic transition point is also much harder to identify at this time due to the slower transition it undergoes; however, it can still be seen around x=200mm.

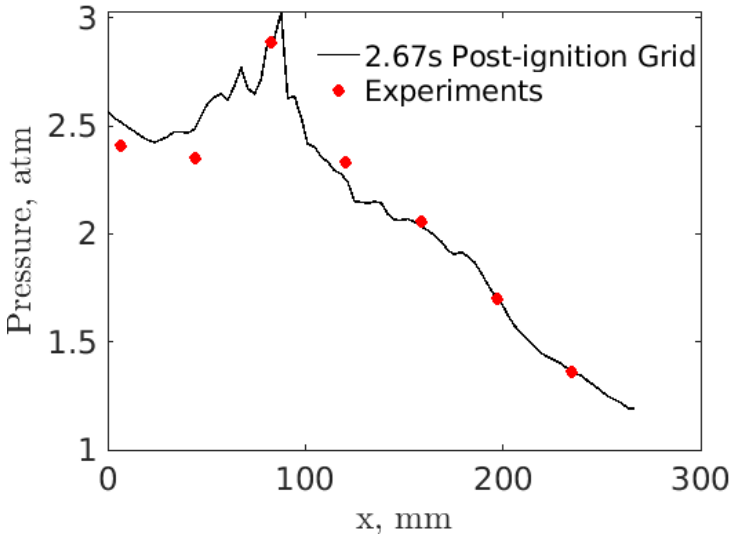


Figure 7.37: Comparisons of pressure along the fuel surface after 2.67 seconds of combustion

Figure 7.38 shows comparisons of the regression rates for the ignition and preheating geometries to the experimental values where the green line shows the undeformed fuel geometry for reference. Experimental regression rates were recorded in 0.333 second increments, and the values presented here represent fuel regression from $0.333 - 0.667$ seconds after ignition. The regression rate is under-predicted in the cavity; however, the ignition geometry only slightly under-predicts regression and thus performs much better in this region. The regression on the ramp at the rear of the cavity is under-predicted using the preheating geometry, but the updated mesh captures the values very well. Both the preheating and ignition mesh geometries accurately reproduce the regression in the constricted area section. One might notice a strange trend in the regression rate for the expanding section of the ignition geometry. This peak is due to the choking of the flow, and provides a possible explanation for how pyrolyzation in the constricted area section is aided. It is well known that the choke point of a flow produces an increase in heat flux which in this case is correlated to the fuel regression rate. As the fuel regresses, the choke location will change. This is likely why the regression rate for the ignition

geometry is slightly under the mean at 120mm, but is over the mean experimental values at 160mm and 190mm. As the choke point moves between the constricted area section and the expansion region, the slope of the regression rate in this region will become averaged and smoothed out. This non-stationary choke point likely aids in regression and helps to maintain a level surface in the constricted area section and early expansion section. This mechanism of continuous leveling is then what produces the decreased slopes at later times of combustion as seen in the geometry 2.67 seconds after ignition. The computational fuel mass flux shown indicates the mass flux found using the ignition geometry, and one can see it closely agrees with experimental values.

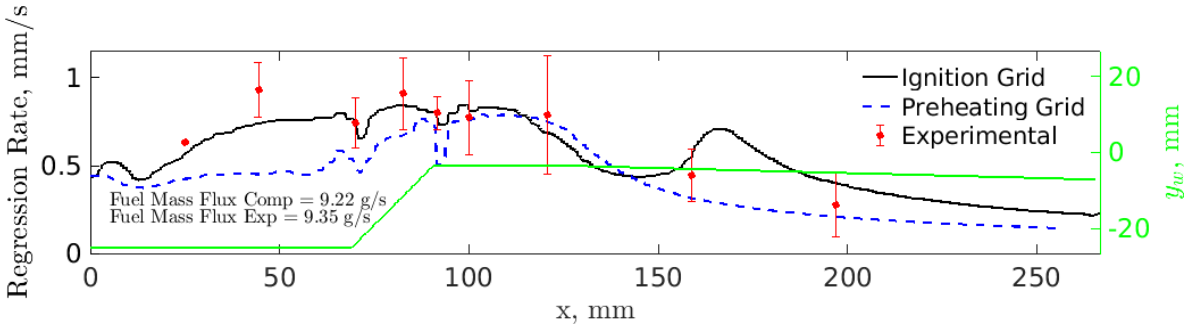


Figure 7.38: Comparison of fuel regression rate at time of ignition

Figure 7.39 shows a comparison between recorded experimental regression rates and the regression rates of the 2.67 second post-ignition geometry. The experimental values were found using a similar method as described previously, but instead looked at regression rates $2.333 - 2.667$ seconds after ignition. One can see all regression rates match well except those falling in the range of $90 < x < 120$ millimeters. This location corresponds to the ending corner of the ramp section and beginning of what was originally the expanding section. Because the current regression prediction model is only dependent upon heat flux, this discrepancy is likely due to mechanical shear. As seen previously in Figures 7.33c and 7.37, the core flow is moving more quickly at this point in combustion and has a stronger impingement on the rear ramp of the cavity which could be removing the melt layer via spallation as opposed to thermal decomposition. If this were the case, the fuel removed at the end of the ramp section might still be partially composed of condensed, liquid MMA which would absorb more heat from the surrounding fluid. This

absorption of heat could cause a temporary decrease in heat flux to the surface directly downstream. This is a likely explanation for the sudden increase followed by a sharp decline in experimental regression rates in the region of $90 < x < 120$ millimeters.

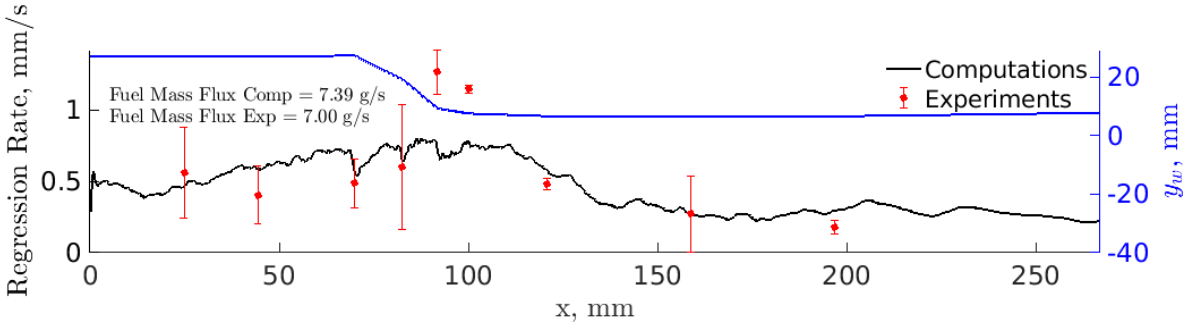


Figure 7.39: Comparison of fuel regression rate 2.67 seconds after ignition

7.4.3 Discussion

In conclusion, each of the geometries supports qualitatively similar streamlines; however, the regression of the surface - specifically near the constricted area section has several large impacts on the resulting combustion. Prior to the preheating stage, there is a large buildup of pressure inside the cavity that causes shocks inside the upstream nozzle and subsonic flow through the combustor. This upstream shock causes total pressure losses that decrease the stagnation pressure within the cavity. Due to the now subsonic flow, the reactants have time to combust in the core flow when traveling from the front to the back of the cavity region.

In the simulations modeling the combustor geometry at ignition, the core flow is initially supersonic, but thermal choking occurs shortly after its entrance into the cavity section of the combustor. The increased flow speed and decreased residence time of species did not allow the reactants sufficient time to fully react in the core flow of the cavity section. Fortunately, the supersonic flow at the entrance to the cavity section moved the reattachment point between the supersonic shear flow and the recirculation zones within the depths of the cavities. This movement increased the size of the mixing regions near the front of the cavity and provided a viable flameholding mechanism in this zone. While the temperature throughout the rest of the cavity is lower than in the preheating geometry, the heat flux to the fuel is greater due to an increase in flow

speed and thinner boundary layers within the cavity. A visualization of this decreased boundary layer thickness can be inferred from Figure A.8 in Appendix A which displays the wall shear stress for the three geometries during combustion. This allowed energy to be transported closer to the surface in the ignition geometry and caused an increase in fuel injection and regression rate that better matched experimental findings. The regression of the fuel near the constricted area section shifted the expanding section further downstream which in turn shifted the flow choke location. The choking of the flow in this downstream location caused an increase in the surface regression rate. If these geometries were not fixed in time, this choke location would change and provide a strong mechanism for fuel pyrolysis in this region. The effect of this moving choke location is a constricted area section that slowly levels itself with the expanding section such that the expanding section's slope is decreased.

The effect of this leveling has become evident after 2.67 seconds of combustion, and the constricted area section and expanding sections of the combustor merge nearly seamlessly. The supersonic transition in the expanding section is much more gradual than in previous geometries. As the constricted area section continues to open, the supersonic core flow penetrates further into the cavity section and pushes fluid through the constricted section much more easily. This causes the pressure within the cavity to decrease leading to slower reaction time of species and a decrease in heat flux to the fuel surface. Fortunately, despite the decreased reaction rates and fuel injection, flameholding is still possible due to the increased size of the recirculation regions in the front corners of the cavities.

The flamelet-progress variable approach and flamelet generated manifold it used were shown to provide strong agreement with experimental results. They are therefore recommended for future investigations into SFSJ combustion. Similarly, the surface regression model performed well in most regions; however, regions that experienced high speed flow impingement under-predicted experimental values, so additional models might be needed to account for mechanical stripping of the liquid fuel.

Chapter 8

Conclusions and Recommendations for Future Work

The research herein investigated the numerical modeling of solid fuel ramjet and scramjet (SFRJ and SFSJ) combustion using polymethyl methacrylate as a model fuel. The work presented encompasses many aspects including:

1. compilation and validation of a chemical mechanism describing the breakdown of MMA and air into their products
2. modeling of the solid fuel decomposition from solid to gaseous phases through the use of a multiphase melt layer
3. tabulating the melt layer products as a function of heat flux to the surface in order to later model fuel regression rates based on the heat flux to the fuel surface
4. the creation of multiple flamelet generated manifolds and their incorporation into a discontinuous Galerkin solver
5. comparison between the presented flamelet-progress variable approach and finite rate chemistry in multiple scenarios
6. a method to evaluate and improve future iterations of the FGM using finite rate chemistry

7. analysis of non-reacting flow through a scramjet combustor and the acoustic modes and instabilities present therein

8. numerical analysis of solid fuel ramjets and effects of mixing and combustion on surface regression

9. numerical analysis of solid fuel scramjet combustion using multiple geometries and two different FGM models

10. the development of a surface regression algorithm using B-Spline basis to move fuel wall surfaces while maintaining mesh quality in order to observe transition from ramjet to scramjet mode in a dual mode SFSJ

Initial validation of the chemical mechanism utilized experimental comparison in a counterflow stagnation flame set up. During this effort, a multiphase foam layer was experimentally observed and, when numerically investigated, was shown to increase regression rate by extending reactant residence time within the bubbles. A mutiphase model was created and incorporated into the counterflow validation tests. The computational results showed good agreement with experimental findings, and the products of the foam model were stored inside a library as a function of heat flux for later use.

Flamelet generated manifolds (FGMs) were created and implemented via the flamelet-progress variable (FPV) approach. Initial manifolds were created using two air temperatures to account for the varying recovery temperatures anticipated in the different ramjet and scramjet configurations. In the higher temperature case, the unsteady portion of the FGMs was modeled using both extinction and ignition phenomenon. These FGMs used a novel approach to incorporate compressibility effects into the flamelet progress rate using a polynomial curve fit to include libraries at multiple pressures while not increasing the dimensions of the FGM. They also used a novel approach to read FGM libraries that are not strictly monotonic for all values of the mixture fraction.

In order to provide more detailed insight into the performance of the FGMs, finite rate chemistry (FRC) simulations were run for comparison in simplified geometries. Progress variable production rates and temperatures were compared with the FPV approach. Both

the extinction and ignition based FGMs performed quite well in a deep cavity geometry that had reached a quasi-steady state, but the ignition library outperformed the extinction during the early autoignition phenomenon. In a separate geometry that simulated combustion in a highly strained boundary layer, the extinction library performed poorly in both the initial ignition and later blowoff phenomenon. The ignition model did well in modeling the production of the progress variable and heat release; however, both FGM models had issues with species transport when comparing to the FRC solutions. The data from these FRC simulations permitted identification of shortcomings in the FGM and provide a clear evaluation metric in order to improve future iterations of the PMMA FGM model.

Non-reacting scramjet combustor configurations were simulated and compared with experimental measurments. The numerical and experimental results showed good agreement, and the flow was analyzed in order to better understand the instabilities supported by supersonic flow in an enclosed geometry with deep cavity recessions. It was discovered that large scale turbulent eddies play a large role in breaking down the freestream. These structures are dampened by 3D acoustic modes inside the cavities, but their recirculation through the cavity and upstream to the combustor inlet are still enough to disrupt the supersonic shear layer. This disruption in conjunction with the increased pressure at the rear of the cavity causes flow biasing in certain geometries. This biasing can cause large non-symmetric recirculation zones in the cavities that could aid in flame holding via a increase in species residence time and mixing.

The FGMs were then implemented into a finite element discontinuous Galerkin solver using a FPV approach. This approach was used to investigate numerous geometries including studies on both both ramjet and scramjet combustors. In each case, the fuel injection rate from the fuel walls was a function of the heat flux to the surface and the previously mentioned foam layer output tabulation. In ramjets, regression rates were shown to spike at the end of the cavities with larger cavities providing greater mixing and fuel residence time and thus increasing the heat flux and regression rates. The scramjet geometries utilized much larger cavity regions to aid in flame holding; however,

the regression rate still tended to be the greatest near the end of the cavity due to flow impingement. For fuel grain 14 (with a H/L ratio of 0.7 inside the cavity prior to deformation), several geometries were investigated that corresponded to different points in time. These stationary, regressed geometries provided insight into the mechanisms that drive fuel regression. As the constricted area section downstream of the cavities opens up, choke points are created where the flow transitions from sub- to supersonic. These locations greatly increase the heat flux to the area and thus these regions regress more quickly than the surroundings. As the choke location changes, the constricted area section and expanding section slowly level to a very gradual and nearly constant slope that greatly decreases the expansion ratio at the combustor exit. Ramjet and scramjet results were compared with experimental data and showed strong agreement which validated the FGM approach to modeling SFRJ and SFSJ combustion.

In conclusion, a chemical mechanism was compiled, validated, and used to create a manifold of flamelet states. This manifold, in conjunction with a PMMA regression rate model, was used to model solid fuel ramjet and scramjet combustion. In order to continue to improve the FGMs, FRC simulations were run to provide more detailed benchmarks. Using these FRC results, the FGM was then improved upon to demonstrate the versatility of the model. Experimental comparison was used validate the approach, and the numerical simulations provided insight into the mechanisms supporting instabilities, regression rates, and flame holding in SFRJs and SFSJs.

Future work should focus on the continuing development of the FGM using the FRC benchmark framework provided herein. As the FGM improves, so will its ability to predict ignition and extinction phenomenon in lab scale SFSJ combustors and thus aid in the development of smaller and more efficient cavities. In the same regard, implementation of B-spline active surface regression into more geometries is likely to provide insights into extinction phenomenon in simulations with long run times. Being able to safely push these extinction limits will greatly aid in our understanding of the factors that affect the duration of combustion and thus applicability of SFSJ design.

Bibliography

[1] Ronald S. Fry. A century of ramjet propulsion technology evolution. *Journal of Propulsion and Power*, 20(1), 2004.

[2] Roni Zvuloni, Yeshayahou Levy, and Alon Gany. Investigation of a small solid fuel ramjet combustor. *Journal of propulsion and power*, 5(3):269–275, 1989.

[3] Abraham Cohen-Zur and Benveniste Natan. Experimental investigation of a supersonic combustion solid fuel ramjet. *Journal of Propulsion and Power*, 14(6):880–889, 1998.

[4] Naminosuke Kubota. *Propellants and explosives: thermochemical aspects of combustion*. John Wiley & Sons, 2015.

[5] Ilan Hadar and Alon Gany. Fuel regression mechanism in a solid fuel ramjet. *Propellants, explosives, pyrotechnics*, 17(2):70–76, 1992.

[6] Obula Reddy Kummitha. Numerical analysis of passive techniques for optimizing the performance of scramjet combustor. *International journal of hydrogen energy*, 42(15):10455–10465, 2017.

[7] Peter G Cross and Iain D Boyd. Two-dimensional modeling of ablation and pyrolysis with application to rocket nozzles. *Journal of Spacecraft and Rockets*, 54(1):212–224, 2017.

[8] Ruben Van de Vijver, Nick M Vandewiele, Pierre L Bhoorasingh, Belinda L Slakman, Fariba Seyedzadeh Khanshan, Hans-Heinrich Carstensen, Marie-Françoise Reyniers, Guy B Marin, Richard H West, and Kevin M Van Geem. Automatic

mechanism and kinetic model generation for gas-and solution-phase processes: a perspective on best practices, recent advances, and future challenges. *International Journal of Chemical Kinetics*, 47(4):199–231, 2015.

[9] Charles D. Pierce and Parviz Moin. Progress-variable approach for large-eddy simulation of non-premixed turbulent combustion. *Journal of Fluid Mechanics*, 504:73–97, 2004.

[10] Henry Pace, Aidan Jessup, Dominic Gallegos, Greg Young, and Luca Massa. Counterflow Combustion and Regression of PMMA Model Fuel. Chicago, Illinois & Virtual, June 2022. AIAA Paper 2022-3996.

[11] Henry Pace, Charles Arnold, Dominic Gallegos, Greg Young, and Luca Massa. Acoustics in flameholding solid-fuel-ramjet fuel grains. *AIAA Journal*, 61(10):4579–4597, 2023.

[12] Dominic Gallegos, Henry Pace, Charles Arnold, Luca Massa, and Gregory Young. Regression and flame structure in cavity flameholding solid-fuel ramjet fuel grains. *Journal of Propulsion and Power*, 39(6):800–810, 2023.

[13] Nigel Clark and Kathryn Yusoff. Combustion and society: A fire-centred history of energy use. *Theory, Culture, and Society*, 31(5):203–226, 2014.

[14] Luigi DeLuca. *Highlights of Solid Rocket Propulsion History*, pages 1015–1032. Springer, Cham, 01 2017.

[15] E. Gray, H. Marsh, and M McLaren. A short history of gunpowder and the role of charcoal in its manufacture. *Journal of Materials Science*, 17:3385–3400, 1982.

[16] C Carmicino. Special issue "advances in hybrid rocket technology and related analysis methodologies". *Aerospace*, 6(12):128, 2019.

[17] C. Carmicino and A Russo Sorge. Experimental investigation into the effect of solid-fuel additives on hybrid rocket performance. *Journal of Propulsion and Power*, 31(2):699–713, 2015.

[18] Kaushal Kishore, Vencatesh R. Pai Verneker, and Ganga Prasad. Storage stability of solid rocket fuel. 1. effect of temperature. *Fuel*, 56(3):292–294, 1977.

[19] Alon Gany and Yaakov M. Timnat. Advantages and drawbacks of boron-fueled propulsion. *Acta Astronautica*, 29(3):181–187, 1993.

[20] W. H. Campbell Jr., B. N. Ko, S. R. Lowe, and D. W. Netzer. Solid-fuel ramjet fuel regression rate/thrust modulation. *JOURNAL OF PROPULSION AND POWER*, 8(3):624–629, 1992.

[21] G Marxman and M Gilbert. Turbulent boundary layer combustion in the hybrid rocket. *Symposium (International) on Combustion*, 9:371–383, 1963.

[22] Alon Gany. Accomplishments and challenges in solid fuel ramjets and scramjets. *International Journal of Energetic Materials and Chemical Propulsion*, pages 421–446, January 2009.

[23] Paul A Czysz, Claudio Bruno, and Bernd Chudoba. Commercial near-earth launcher: Propulsion choices. In *Future Spacecraft Propulsion Systems and Integration*, pages 123–191. Springer, 2018.

[24] US Air Force Scientific Advisory Board. Why and whither hypersonics research in the us air force. Technical report, SAB-TR-00-03, 2000.

[25] David Van Wie. Hypersonics: Past, present, and potential future. *Johns Hopkins APL Technical Digest*, 35(4):335–341, 2021.

[26] Laurie Marshall, Griffin Corpening, and Robert Sherrill. *A Chief Engineer's View of the NASA X-43A Scramjet Flight Test.* Aerospace Research Central, 2012.

[27] Joseph Hank, James Murphy, and Richard Mutzman. *The X-51A Scramjet Engine Flight Demonstration Program.* Aerospace Research Central, 2012.

[28] Jihad A. Badra, Fethi Khaled, Meng Tang, Yuanjiang Pei, Janardhan Kodavasal, Pinaki Pal, Opeoluwa Owoyele, Carsten Fuetterer, Brenner Mattia, and Farooq

Aamir. Engine Combustion System Optimization Using Computational Fluid Dynamics and Machine Learning: A Methodological Approach. *Journal of Energy Resources Technology*, 143(2):022306, 08 2020.

[29] Rajkumar Vaidyanathan, P Kevin Tucker, Nilay Papila, and Wei Shyy. Computational-fluid-dynamics-based design optimization for single-element rocket injector. *Journal of propulsion and power*, 20(4):705–717, 2004.

[30] Amirreza Saghafian, Vincent E. Terrapon, and Heinz Pitsch. An efficient flamelet-based combustion model for compressible flows. *Combustion and Flame*, 162(3):652–667, 2015.

[31] Suo Yang, Xingjian Wang, Hongfa Huo, Wenting Sun, and Vigor Yang. An efficient finite-rate chemistry model for a preconditioned compressible flow solver and its comparison with the flamelet/progress-variable model. *Combustion and Flame*, 210:172–182, 2019.

[32] Raymond Friedman. *A History of Jet Propulsion, Including Rockets*. Xlibris Corporation, 2010.

[33] John D Anderson Jr. History of high-speed flight and its technical development. *AIAA Journal*, 39(5):761–771, 2001.

[34] Michel Van Pelt. *Rocketing into the future: the history and technology of rocket planes*. Springer Science & Business Media, 2012.

[35] J Anderson. Research in supersonic flight and the breaking of the sound barrier. *Retrieved September*, 30:2009, 2001.

[36] E Riester. *Comparison of turbojet, turborocket and ramjet as a propulsion system for long range airplanes at mach numbers between 2 and 4*. NTIS, US Department of Commerce., 1975.

[37] R. BAKOS, R. MORGAN, and J. TAMAGNO. *Effects of oxygen dissociation on hypervelocity combustion experiments*. Aerospace Research Central, 2012.

[38] Charles McClinton. *X-43 - Scramjet Power Breaks the Hypersonic Barrier: Dryden Lectureship in Research for 2006.* Aerospace Research Central, 2012.

[39] Randall C. Boehm, Zhibin Yang, David C. Bell, John Feldhausen, and Joshua S. Heyne. Lower heating value of jet fuel from hydrocarbon class concentration data and thermo-chemical reference data: An uncertainty quantification. *Fuel*, 311:122542, 2022.

[40] Antonella Ingenito. *Subsonic combustion ramjet design.* Springer, 2021.

[41] Seong-kyun Im and Hyungrok Do. Unstart phenomena induced by flow choking in scramjet inlet-isolators. *Progress in Aerospace Sciences*, 97:1–21, 2018.

[42] S Im, D Baccarella, B McGann, Q Liu, L Wermer, and H Do. Unstart phenomena induced by mass addition and heat release in a model scramjet. *Journal of Fluid Mechanics*, 797:604–629, 2016.

[43] Sean O'Byrne, Matthew Doolan, SR Olsen, and AFP Houwing. Analysis of transient thermal choking processes in a model scramjet engine. *Journal of Propulsion and Power*, 16(5):808–814, 2000.

[44] Johan Larsson, Stuart Laurence, Iván Bermejo-Moreno, Julien Bodart, Sebastian Karl, and Ronan Vicquelin. Incipient thermal choking and stable shock-train formation in the heat-release region of a scramjet combustor. part ii: Large eddy simulations. *Combustion and Flame*, 162(4):907–920, 2015.

[45] Chukwuka C. Mbagwu, James F. Driscoll, Derek J. Dalle, and Sean M. Torrez. Combustion efficiencies and flameout limits computed for a hypersonic vehicle during ascent. *Journal of Propulsion and Power*, 34(3):624–635, 2018.

[46] Aristides M Bonanos, Jeffrey M Bergthorson, and Paul E Dimotakis. Molecular mixing and flowfield measurements in a recirculating shear flow. part ii: supersonic flow. *Flow, turbulence and combustion*, 83:251–268, 2009.

[47] Peter Gerlinger, Peter Stoll, Markus Kindler, Fernando Schneider, and Manfred Aigner. Numerical investigation of mixing and combustion enhancement in supersonic combustors by strut induced streamwise vorticity. *Aerospace Science and Technology*, 12(2):159–168, 2008.

[48] Franklin Génin and Suresh Menon. Simulation of turbulent mixing behind a strut injector in supersonic flow. *AIAA Journal*, 48(3):526–539, 2010.

[49] Gautam Choubey and K.M. Pandey. Effect of different wall injection schemes on the flow-field of hydrogen fuelled strut-based scramjet combustor. *Acta Astronautica*, 145:93–104, 2018.

[50] J. R. Koseff and R. L. Street. The Lid-Driven Cavity Flow: A Synthesis of Qualitative and Quantitative Observations. *Journal of Fluids Engineering*, 106(4):390–398, 12 1984.

[51] M. R. Gruber, R. A. Baurle, T. Mathur, and K.-Y. Hsu. Fundamental studies of cavity-based flameholder concepts for supersonic combustors. *Journal of Propulsion and Power*, 17(1):146–153, 2001.

[52] M. R. Gruber, J. M. Donbar, C. D. Carter, and K.-Y. Hsu. Mixing and combustion studies using cavity-based flameholders in a supersonic flow. *Journal of Propulsion and Power*, 20(5):769–778, 2004.

[53] Roni Zvuloni, Alon Gany, and Yeshavahou Levy. Geometric effects on the combustion in solid fuel ramjets. *Journal of Propulsion and Power*, 5(1):32–37, 1989.

[54] Andreas Züttel. Hydrogen storage methods. *Naturwissenschaften*, 91:157–172, 2004.

[55] Edward T. Curran. Scramjet engines: The first forty years. *Journal of Propulsion and Power*, 17(6):1138–1148, 2001.

[56] Adela Ben-Yakar, Benveniste Natan, and Alon Gany. Investigation of a solid fuel scramjet combustor. *JOURNAL OF PROPULSION AND POWER*, 14(4):447–455, 1998.

[57] Michael A Witt. Investigation into the feasibility of using solid fuel ramjets for high supersonic/low hypersonic tactical missiles. *Marster's Thesis, Department of Astronautical Engineering, Nava Postgraduate School, Monterey, CA, USA*, 1989.

[58] William J Angus and David W Netzer. *An investigation into the performance characteristics of a solid fuel scramjet propulsion device*. PhD thesis, Naval Postgraduate School Monterey, CA, 1991.

[59] Victor Chernov. Experimental investigation of a solid fuel scramjet using an arc heater. *Journal of Propulsion and Power*, 35(4):879–882, 2019.

[60] Osvalda Senneca, Riccardo Chirone, and Piero Salatino. Oxidative pyrolysis of solid fuels. *Journal of Analytical and Applied Pyrolysis*, 71(2):959–970, 2004.

[61] Colomba Di Blasi. Modeling and simulation of combustion processes of charring and non-charring solid fuels. *Progress in Energy and Combustion Science*, 19(1):71–104, 1993.

[62] Y Yano, K Miyata, N Kubota, and S Sakamoto. Combustion wave structure of ap composite propellants. *Propellants, explosives, pyrotechnics*, 12(4):137–140, 1987.

[63] Merrill W. Beckstead, Karthik Puduppakkam, Piyush Thakre, and Vigor Yang. Modeling of combustion and ignition of solid-propellant ingredients. *Progress in Energy and Combustion Science*, 33:497–551, 2007.

[64] S No, J Gu, H Moon, C Lee, and Y Jo. *An introduction to combustion: concepts and applications*. McGraw-Hill Korea, 2011.

[65] Gregory Young, Scott Hromisin, Sam Loeffler, and Terrence L. Connell. Effect of oxidizer type on solid fuel combustion. *Journal of Propulsion and Power*, 36(2):248–255, 2020.

[66] C Lautenberger and AC Fernandez-Pello. Pyrolysis modeling, thermal decomposition, and transport processes in combustible solids. *Transport phenomena in fires*, 20:209, 2008.

[67] Paul Kutler. A perspective of theoretical and applied computational fluid dynamics. *AIAA journal*, 23(3):328–341, 1985.

[68] Mori Mani and Andrew J Dorgan. A perspective on the state of aerospace computational fluid dynamics technology. *Annual Review of Fluid Mechanics*, 55:431–457, 2023.

[69] W Lazik, Th Doerr, S vd Bake, R vd Bank, and L Rackwitz. Development of lean-burn low-nox combustion technology at rolls-royce deutschland. In *Turbo Expo: Power for Land, Sea, and Air*, volume 43130, pages 797–807, 2008.

[70] Joel H Ferziger and Milovan Perić. *Computational methods for fluid dynamics*. Springer, 2002.

[71] Liang Wang, Lianghua Xiao, and Song Fu. A modular rans approach for modeling hypersonic flow transition on a scramjet-forebody configuration. *Aerospace Science and Technology*, 56:112–124, 2016.

[72] JR Nanduri, DR Parsons, SL Yilmaz, IB Celik, and PA Strakey. Assessment of rans-based turbulent combustion models for prediction of emissions from lean premixed combustion of methane. *Combustion Science and Technology*, 182(7):794–821, 2010.

[73] Christer Fureby, Guillaume Sahut, Alessandro Ercole, and Thommie Nilsson. Large eddy simulation of combustion for high-speed airbreathing engines. *Aerospace*, 9(12):785, 2022.

[74] Xiaofeng Yang, Saurabh Gupta, Tang-Wei Kuo, and Venkatesh Gopalakrishnan. Rans and large eddy simulation of internal combustion engine flows—a comparative study. *Journal of Engineering for Gas Turbines and Power*, 136(5):051507, 2014.

[75] Magnus Berglund and C Fureby. Les of supersonic combustion in a scramjet engine model. *Proceedings of the Combustion Institute*, 31(2):2497–2504, 2007.

[76] R. A. Baurle. Hybrid reynolds-averaged/large-eddy simulation of a scramjet cavity flameholder. *AIAA Journal*, 55(2):544–560, 2017.

[77] Matthew A. Trudgian, Will O. Landsberg, and Ananthanarayanan Veeraragavan. Experimental investigation of inclining the upstream wall of a scramjet cavity. *Aerospace Science and Technology*, 99:105767, 2020.

[78] Antonella Ingenito and Claudio Bruno. Physics and regimes of supersonic combustion. *AIAA journal*, 48(3):515–525, 2010.

[79] Olek C Zienkiewicz, Robert L Taylor, and Jian Z Zhu. *The finite element method: its basis and fundamentals*. Elsevier, 2005.

[80] Fadl Moukalled, Luca Mangani, Marwan Darwish, F Moukalled, L Mangani, and M Darwish. *The finite volume method*. Springer, 2016.

[81] L Diaz Angulo, J Alvarez, M Fernández Pantoja, S Gonzales Garcia, and AR Bretones. Discontinuous galerkin time domain methods in computational electrodynamics: State of the art. In *Forum Electromagn. Res. Methods Appl. Technol*, volume 10, pages 1–24, 2015.

[82] Chi-Wang Shu. A brief survey on discontinuous galerkin methods in computational fluid dynamics. *Advances in mechanics*, 43(6):541–553, 2013.

[83] James Juno, Ammar Hakim, Jason TenBarge, Eric Shi, and William Dorland. Discontinuous galerkin algorithms for fully kinetic plasmas. *Journal of Computational Physics*, 353:110–147, 2018.

[84] Thomas JR Hughes, Gerald Engel, Luca Mazzei, and Mats G Larson. The continuous galerkin method is locally conservative. *Journal of Computational Physics*, 163(2):467–488, 2000.

[85] Bernardo Cockburn. Discontinuous galerkin methods. *ZAMM-Journal of Applied Mathematics and Mechanics/Zeitschrift für Angewandte Mathematik und Mechanik: Applied Mathematics and Mechanics*, 83(11):731–754, 2003.

[86] Pascal J Frey and Frédéric Alauzet. Anisotropic mesh adaptation for transient flows simulations. In *IMR*, pages 335–348, 2003.

[87] Pascal J Frey and Houman Borouchaki. Geometric surface mesh optimization. *Computing and visualization in science*, 1(3):113–121, 1998.

[88] D. Lynch and K. O'Neill. *Finite Elements in Water Resources*, chapter Elastic Grid Deformation for Moving Boundary Problems in Two Space Dimensions, pages 7.111–7.120. Agricultural Research (Souther Region) Science and Education Administration, US Department of Agriculture, 1980.

[89] Aleksander L Zibitsker, Joel McQuaid, Christoph Brehm, and Alexandre Martin. Development and verification of a mesh deformation scheme for a three dimensional ablative material solver. In *AIAA Scitech 2022 Forum*, page 1285, 2022.

[90] Joseph C Schulz, Eric Stern, Suman Muppidi, Grant Palmer, Olivia Schroeder, and Alexandre Martin. Development of a three-dimensional, unstructured material response design tool. In *55th AIAA Aerospace Sciences Meeting*, page 0667, 2017.

[91] Qiang Li, Guo-qiang He, Pei-jin Liu, and Jiang Li. Coupled simulation of fluid flow and propellant burning surface regression in a solid rocket motor. *Computers & Fluids*, 93:146–152, 2014.

[92] Michael L Brewer, Lori Freitag Diachin, Patrick M Knupp, Thomas Leurent, and Darryl J Melander. The mesquite mesh quality improvement toolkit. In *IMR*, 2003.

[93] Jonathan E Wiebenga. *High-Fidelity Material Response Modeling as Part of an Aerothermoelastic Framework for Hypersonic Flows.* PhD thesis, University of Michigan, 2014.

[94] RE Hogan, BF Blackwell, and RJ Cochran. Application of moving grid control volume finite element method to ablation problems. *Journal of thermophysics and heat transfer*, 10(2):312–319, 1996.

[95] Peter G. Cross and Iain D. Boyd. Conjugate analyses of ablation in rocket nozzles. *Journal of Spacecraft and Rockets*, 56(5):1593–1610, 2019.

[96] Alexandre Martin, Leonardo C Scalabrin, and Iain D Boyd. High performance modeling of atmospheric re-entry vehicles. In *Journal of Physics: Conference Series*, volume 341, page 012002. IOP Publishing, 2012.

[97] Obula Reddy Kummitha. Numerical analysis of passive techniques for optimizing the performance of scramjet combustor. *International Journal of Hydrogen Energy*, 42(15):10455–10465, 2017.

[98] Obula Reddy Kummitha, Krishna Murari Pandey, and Rajat Gupta. Cfd analysis of a scramjet combustor with cavity based flame holders. *Acta Astronautica*, 144:244–253, 2018.

[99] R Liinn Belford and Roger A Strehlow. Shock tube technique in chemical kinetics. *Annual review of physical chemistry*, 20(1):247–272, 1969.

[100] Wing Tsang and Assa Lifshitz. Shock tube techniques in chemical kinetics. *Annual review of physical chemistry*, 41(1):559–599, 1990.

[101] Ronald K Hanson and David F Davidson. Recent advances in laser absorption and shock tube methods for studies of combustion chemistry. *Progress in Energy and Combustion Science*, 44:103–114, 2014.

[102] Guy B Marin, Vladimir V Galvita, and Gregory S Yablonsky. Kinetics of chemical processes: From molecular to industrial scale. *Journal of Catalysis*, 404:745–759, 2021.

[103] Yong Sun and Rolf D Reitz. Modeling diesel engine nox and soot reduction with optimized two-stage combustion. Technical report, SAE Technical Paper, 2006.

[104] Olivier Herbinet, Joffrey Biet, Mohammed Hichem Hakka, Valérie Warth, Pierre-Alexandre Glaude, André Nicolle, and Frédérique Battin-Leclerc. Modeling study of the low-temperature oxidation of large methyl esters from c11 to c19. *Proceedings of the Combustion Institute*, 33(1):391–398, 2011.

[105] Juan Li, Zhenwei Zhao, Andrei Kazakov, and Frederick L Dryer. An updated comprehensive kinetic model of hydrogen combustion. *International journal of chemical kinetics*, 36(10):566–575, 2004.

[106] Christopher B Whitehead, Saim Ozkar, and Richard G Finke. Lamer's 1950 model for particle formation of instantaneous nucleation and diffusion-controlled growth: A historical look at the model's origins, assumptions, equations, and underlying sulfur sol formation kinetics data. *Chemistry of Materials*, 31(18):7116–7132, 2019.

[107] Dennis Yoder, Nicholas Georgiadis, and Michael O'Gara. Frozen chemistry effects on nozzle performance simulations. In *38th Fluid Dynamics Conference and Exhibit*, page 3969, 2009.

[108] Ekaterina Fedina, Christer Fureby, Ghenadie Bulat, and Wolfgang Meier. Assessment of finite rate chemistry large eddy simulation combustion models. *Flow, Turbulence and Combustion*, 99:385–409, 2017.

[109] Bonnie J McBride, Michael J Zehe, and Sanford Gordon. Nasa glenn coefficients for calculating thermodynamic properties of individual species. Technical Report 2002-211556, NASA, 2002.

[110] Markus Meuwly. Machine learning for chemical reactions. *Chemical Reviews*, 121(16):10218–10239, 2021.

[111] Ziaul Huque. Mathematically reduced chemical reaction mechanism using neural networks. Technical report, Prairie View A&M University, 2007.

[112] Michael Oevermann. Numerical investigation of turbulent hydrogen combustion in a scramjet using flamelet modeling. *Aerospace Science and Technology*, 4(7):463–480, 2000.

[113] Charles David Pierce. *Progress-variable approach for large-eddy simulation of turbulent combustion.* stanford university, 2001.

[114] Shanmugasundaram Dakshnamurthy, Denis A Knyazkov, Artem M Dmitriev, Oleg P Korobeinichev, Elna JK Nilsson, Alexander A Konnov, and Krithika Narayanaswamy. Experimental study and a short kinetic model for high-temperature oxidation of methyl methacrylate. *Combustion Science and Technology*, 191(10):1789–1814, 2019.

[115] David G. Goodwin, Harry K. Moffat, and Raymond L. Speth. Cantera: An object-oriented software toolkit for chemical kinetics, thermodynamics, and transport processes. `http://www.cantera.org`, 2017. Version 2.3.0.

[116] H. Arisawa and T.B. Brill. Kinetics and Mechanisms of Flash Pyrolysis of Poly(methyl methacrylate) (PMMA). *Combustion and Flame*, 109(3):415–426, May 1997.

[117] Jeffery D Peterson, Sergey Vyazovkin, and Charles A Wight. Kinetic study of stabilizing effect of oxygen on thermal degradation of poly (methyl methacrylate). *The Journal of Physical Chemistry B*, 103(38):8087–8092, 1999.

[118] S Dakka. Tg/dta/ms of poly (methyl methacrylate), the role of the oxidative environment. *Journal of thermal analysis and calorimetry*, 73(1):17–24, 2003.

[119] K Seshadri and FA Williams. Structure and extinction of counterflow diffusion flames above condensed fuels: comparison between poly (methyl methacrylate) and its liquid monomer, both burning in nitrogen–air mixtures. *Journal of Polymer Science: Polymer Chemistry Edition*, 16(7):1755–1778, 1978.

[120] Umar Ali, Khairil Juhanni Bt Abd Karim, and Nor Aziah Buang. A review of the properties and applications of poly (methyl methacrylate)(pmma). *Polymer Reviews*, 55(4):678–705, 2015.

[121] H Arisawa and TB Brill. Kinetics and mechanisms of flash pyrolysis of poly (methyl methacrylate)(pmma). *Combustion and Flame*, 109(3):415–426, 1997.

[122] Robert F McAlevy III, Suh Yong Lee, and Westcott H Smith. Linear pyrolysis of polymethylmethacrylate during combustion. *AIAA Journal*, 6(6):1137–1142, 1968.

[123] OP Korobeinichev, AA Paletsky, MB Gonchikzhapov, RK Glaznev, IE Gerasimov, YK Naganovsky, IK Shundrina, A Yu Snegirev, and R Vinu. Kinetics of thermal decomposition of PMMA at different heating rates and in a wide temperature range. *Thermochimica Acta*, 671:17–25, 2019.

[124] Thomas Steinhaus. *Evaluation of the thermophysical properties of poly (methylmethacrylate): a reference material for the development of a flammability test for micro-gravity environments*. PhD thesis, The University of Maryland, 1999.

[125] Von A Brockhaus and E Jenckel. Über die kinetik des thermischen abbaues von polymethacrylsäuremethylester. *Die Makromolekulare Chemie: Macromolecular Chemistry and Physics*, 18(1):262–293, 1956.

[126] Deniz Rende, Linda S. Schadler, and Rahmi Ozisik. Controlling foam morphology of poly(methyl methacrylate) via surface chemistry and concentration of silica nanoparticles and supercritical carbon dioxide process parameters. *Journal of Chemistry*, 2013, 2013. Article ID 864926.

[127] Martín de León J, Bernardo V, and Rodríguez-Pérez MA. Nanocellular polymers: The challenge of creating cells in the nanoscale. *Materials (Basel)*, 12(5):797, 2019.

[128] Guilong Wanga, Jinchuan Zhaob, Guizhen Wang, Lun Howe Mark, Chul B. Park, and Guoqun Zhao. Low-density and structure-tunable microcellular pmma foams with improved thermal-insulation and compressive mechanical properties. *European Polymer Journal*, 95:382–393, 2017.

[129] M.S. Economon, F. Palacios, S. R. Copeland, T.W. Lukaczyk, and J. J. Alonso. Su2: An open-source suite for multiphysics simulation and design. *AIAA Journal*, 54(3):828–846, 2016.

[130] Ryan F Johnson and Andrew D Kercher. A conservative discontinuous galerkin discretization for the chemically reacting navier-stokes equations. *Journal of Computational Physics*, 423:109826, 2020.

[131] Thierry Poinsot and Denis Veynante. *Theoretical and numerical combustion*. RT Edwards, Inc., 2005.

[132] RWt Bilger. A note on favre averaging in variable density flows. *Combustion Science and Technology*, 11(5-6):215–217, 1975.

[133] RW Bilger, SH Stårner, and RJ Kee. On reduced mechanisms for methane-air combustion in nonpremixed flames. *Combustion and Flame*, 80(2):135–149, 1990.

[134] Charles D Pierce and Parviz Moin. A dynamic model for subgrid-scale variance and dissipation rate of a conserved scalar. *Physics of Fluids*, 10(12):3041–3044, 1998.

[135] Robert J Kee, Michael E Coltrin, and Peter Glarborg. *Chemically reacting flow: theory and practice*. John Wiley & Sons, 2005.

[136] M Chen, J Buckmaster, T.L. Jackson, and L Massa. Homogenization issues and the combustion of heterogeneous solid propellants. *Proceedings of the Combustion Institute*, 29(2):2923–2929, 2002.

[137] Stefan Domino, Chris Moen, Shawn Burns, and Greg Evans. Sierra/fuego: A multimechanics fire environment simulation tool. In *41st Aerospace Sciences Meeting and Exhibit*, page 149, 2003.

[138] Joshua A Hubbard, Michael A Hansen, Jared R Kirsch, John C Hewson, and Stefan P Domino. Medium-scale methanol pool fire model validation. *Journal of Heat Transfer*, 144(6):061303, 2022.

[139] Heinz Pitsch and Matthias Ihme. An unsteady/flamelet progress variable method for les of nonpremixed turbulent combustion. In *43rd AIAA Aerospace Sciences Meeting and Exhibit*, Reno, NV, Jan 2005.

[140] Tuan M Nguyen and William A Sirignano. Spontaneous and triggered longitudinal combustion instability in a single-injector liquid-rocket combustor. *AIAA Journal*, 57(12):5351–5364, 2019.

[141] Brian T Bojko and Paul E DesJardin. Formulation and assessment of flamelet-generated manifolds for reacting interfaces. *Combustion and Flame*, 173:296–306, 2016.

[142] Ethan J. Schlussel, Dominic F. Gallegos, and Gregory Young. Supersonic combustion of solid fuels. *Journal of Propulsion and Power*, 40(3):460–468, 2024.

[143] Ethan Schlussel, Dominic Gallegos, Henry Pace, Luca Massa, and Gregory Young. Flow characteristics in an optically accessible solid fuel scramjet. *Journal of Propulsion and Power (in press)*, 2024.

[144] None None and USDOE Office of Science. Pelec, 8 2017.

[145] Marc T Henry de Frahan, Jon S Rood, Marc S Day, Hariswaran Sitaraman, Shashank Yellapantula, Bruce A Perry, Ray W Grout, Ann Almgren, Weiqun Zhang, John B Bell, et al. Pelec: An adaptive mesh refinement solver for compressible reacting flows. *The International Journal of High Performance Computing Applications*, 37(2):115–131, 2023.

[146] Joseph A Schetz and Rodney DW Bowersox. *Boundary layer analysis*. American Institute of Aeronautics and Astronautics, 2011.

[147] Dominic Gallegos and Greg Young. Utilizing unique fuel geometries to increase performance in solid fuel ramjets. In *AIAA Scitech 2022 Forum*, 2022.

[148] Henry Pace. Analysis of acoustic modes in solid fuel ramjet cavities. *Bulletin of the American Physical Society*, 2022.

[149] Oliver T Schmidt and Tim Colonius. Guide to spectral proper orthogonal decomposition. *AIAA Journal*, 58(3):1023–1033, 2020.

[150] C de Boor. Subroutine package for calculating with b-splines, 1971.

[151] Christophe Geuzaine and Jean-François Remacle. Gmsh: A 3-d finite element mesh generator with built-in pre-and post-processing facilities. *International journal for numerical methods in engineering*, 79(11):1309–1331, 2009.

Appendices

Appendix A

Additional Figures

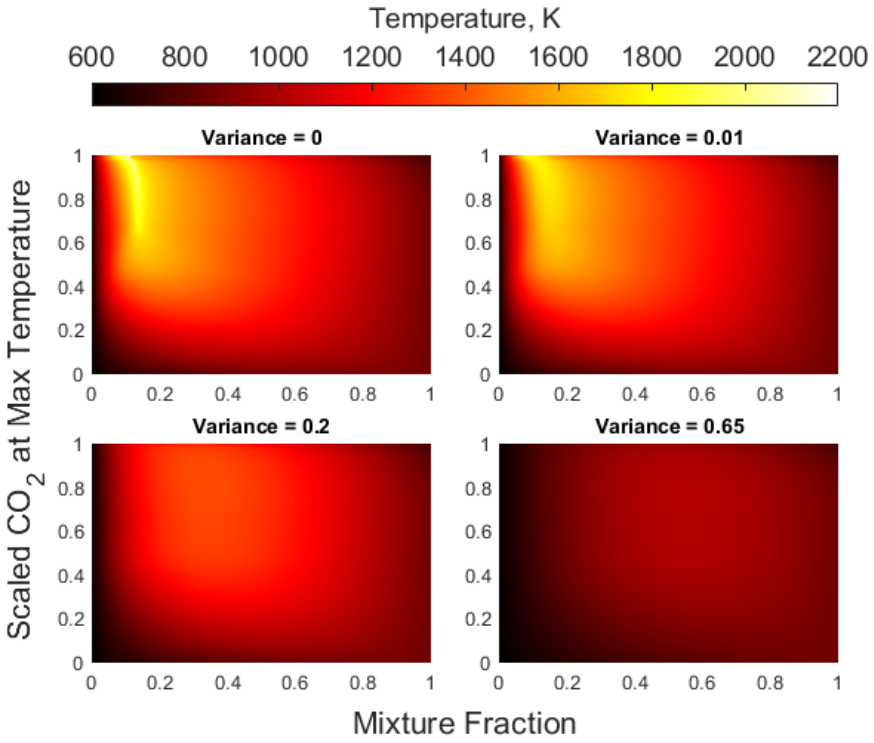
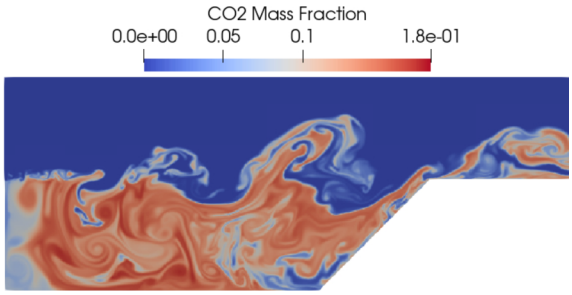
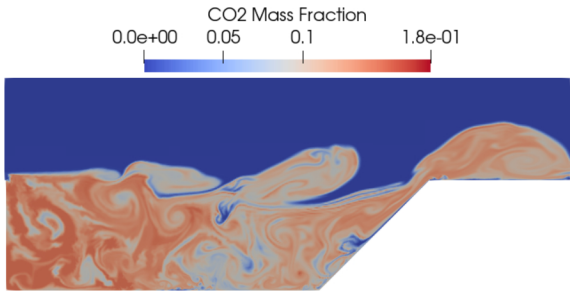


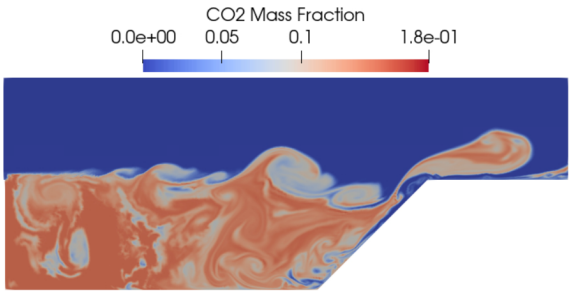
Figure A.1: Temperature distribution inside flamelet generated manifold for MMA at low (600K) oxidizer temperature



(a) Finite rate chemistry solution

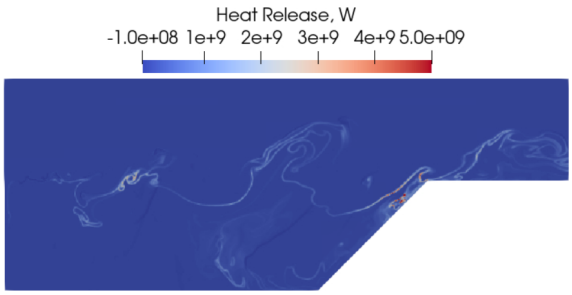


(b) Extinction FGM solution

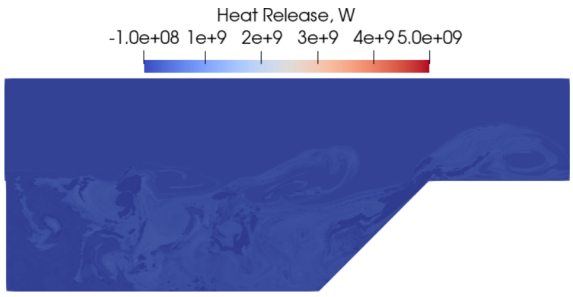


(c) Ignition FGM solution

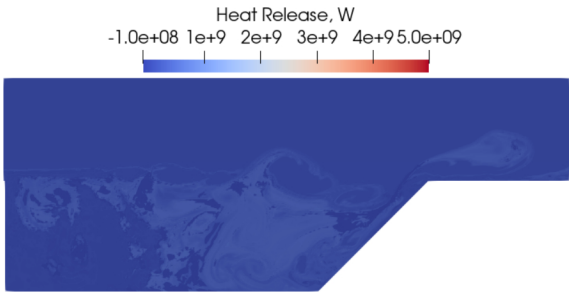
Figure A.2: Comparison of instantaneous CO_2 mass fraction between two FGMs and finite rate chemistry in deep cavity after 2.5e-4 seconds of independent running



(a) Finite rate chemistry solution

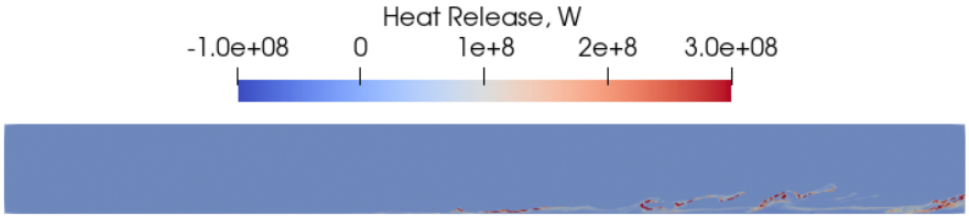


(b) Extinction FGM solution

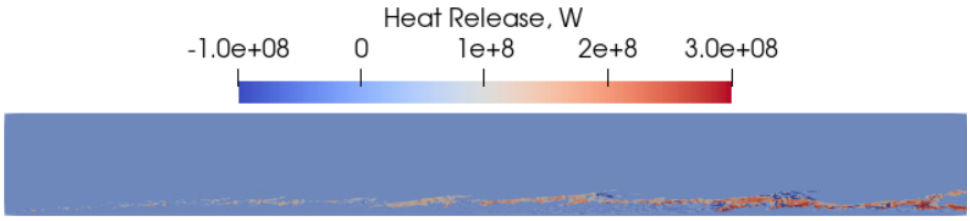


(c) Ignition FGM solution

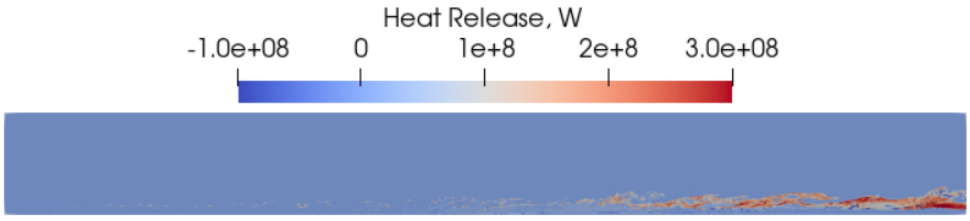
Figure A.3: Comparison of instantaneous heat release between two FGMs and finite rate chemistry in deep cavity after 2.5e-4 seconds of independent running



(a) Finite rate chemistry solution

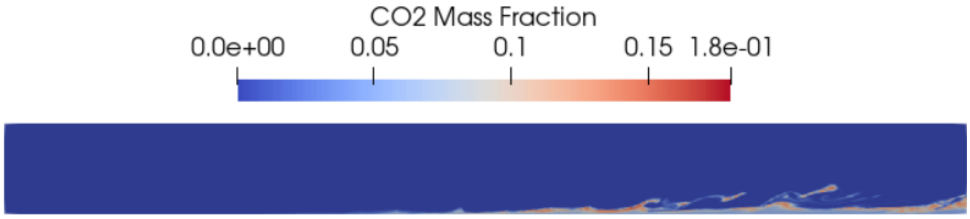


(b) Extinction FGM solution

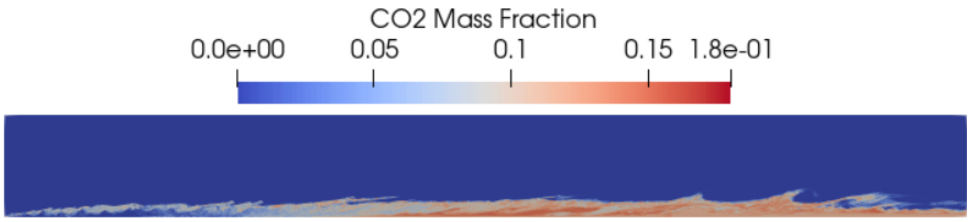


(c) Ignition FGM solution

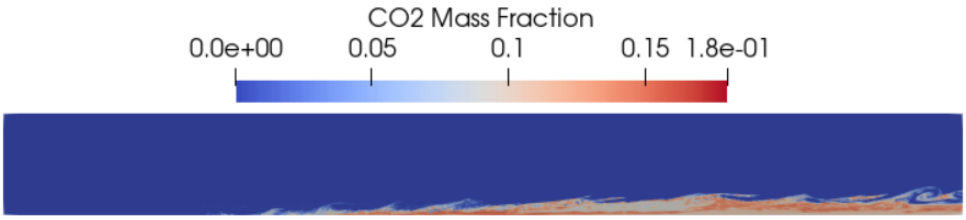
Figure A.4: Comparison of instantaneous heat release between two FGMs and finite rate chemistry in boundary layer blowoff after 2.5e-4 seconds of independent running



(a) Finite rate chemistry solution

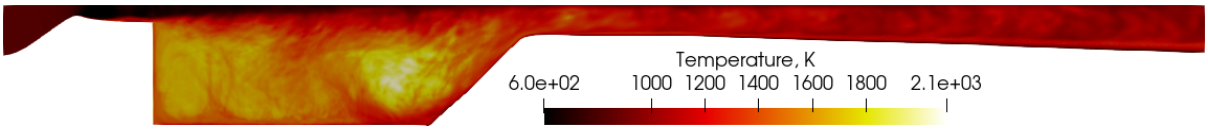


(b) Extinction FGM solution

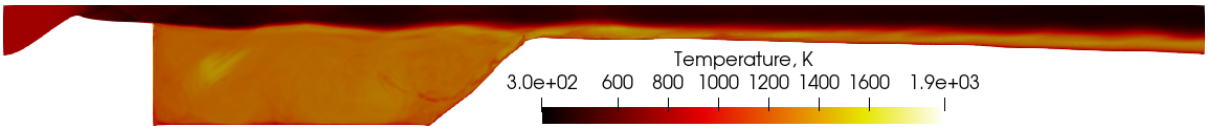


(c) Ignition FGM solution

Figure A.5: Comparison of instantaneous CO_2 mass fraction between two FGMs and finite rate chemistry in boundary layer blowoff after 2.5e-4 seconds of independent running

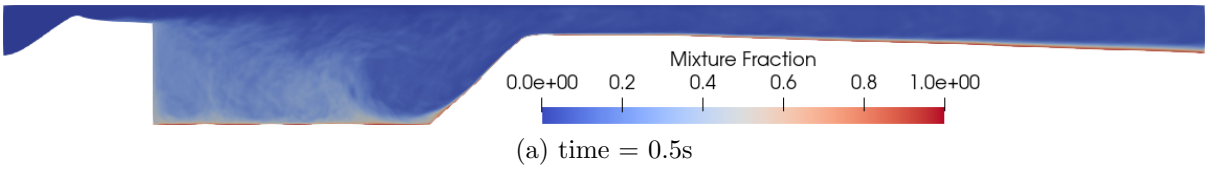


(a) time = 0.5s

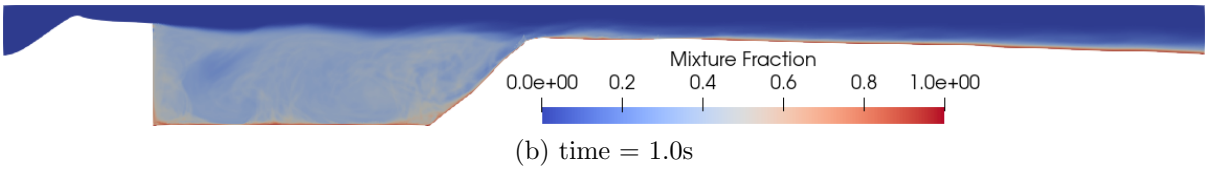


(b) time = 1.0s

Figure A.6: Temperature visualization at different times during combustion for 2D FG11 geometry



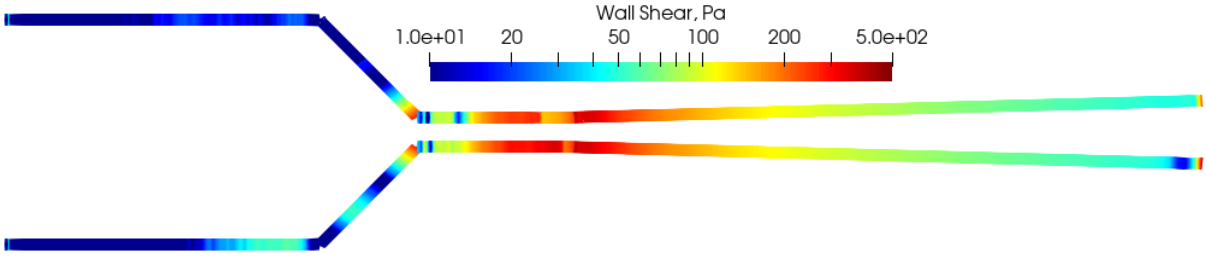
(a) time = 0.5s



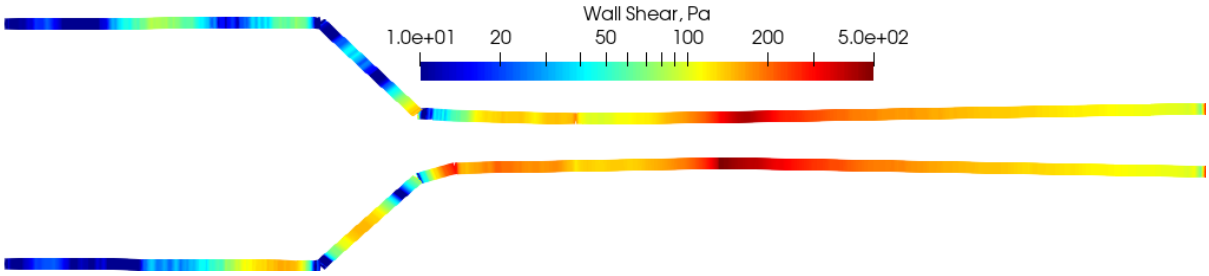
(b) time = 1.0s

Figure A.7: Mixture fraction visualization at different times during combustion for 2D FG11 geometry

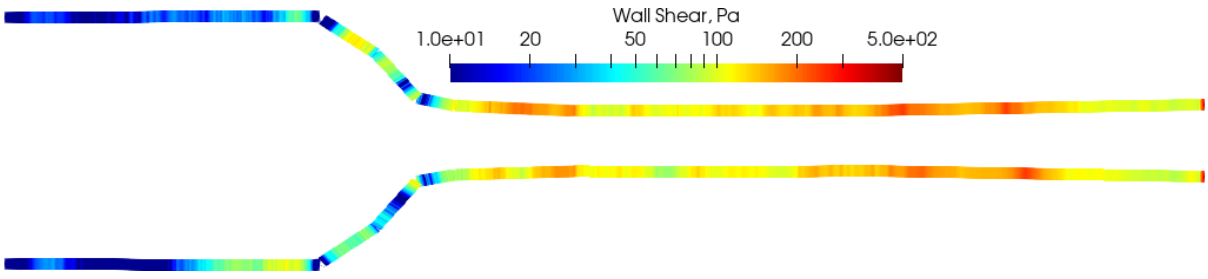
Wall shear was found using $\mu(\frac{\partial u}{\partial y} + \frac{\partial v}{\partial x})$.



(a) Preheating Geometry



(b) Ignition Geometry



(c) 2.67 Post-ignition Geometry

Figure A.8: Wall shear force during FG14 combustion at three stages of solid fuel deformation